Nano-Micro Letters

ISSN 2311-6706
e-ISSN 2150-5551
CN 31-2103/TB

REVIEW

https://doi.org/10.1007/s40820-021-00724-1

Cite as
Nano-Micro Lett.
(2021) 13:207

Received: 13 May 2021
Accepted: 22 August 2021
Published online: 11 October 2021

Advanced Strategies to Improve Performances of Molybdenum-Based Gas Sensors

Angga Hermawan[1,4], Ni Luh Wulan Septiani[2,3], Ardiansyah Taufik[4], Brian Yuliarto[2,3] ✉, Suyatman[2,3] ✉, Shu Yin[4] ✉

HIGHLIGHTS

- Various advanced strategies for improving gas sensing performances of molybdenum-based nanostructures are reviewed.
- The plausible mechanism of enhanced gas sensing properties from each strategy is discussed.
- The conclusive outlook, challenge, and suggestions for future development toward marked commercialization of molybdenum-based gas sensing devices are provided.

ABSTRACT Molybdenum-based materials have been intensively investigated for high-performance gas sensor applications. Particularly, molybdenum oxides and dichalcogenides nanostructures have been widely examined due to their tunable structural and physicochemical properties that meet sensor requirements. These materials have good durability, are naturally abundant, low cost, and have facile preparation, allowing scalable fabrication to fulfill the growing demand of susceptible sensor devices. Significant advances have been made in recent decades to design and fabricate various molybdenum oxides- and dichalcogenides-based sensing materials, though it is still challenging to achieve high performances. Therefore, many experimental and theoretical investigations have been devoted to exploring suitable approaches which can significantly enhance their gas sensing properties. This review comprehensively examines recent advanced strategies to improve the nanostructured molybdenum-based material performance for detecting harmful pollutants, dangerous gases, or even exhaled breath monitoring. The summary and future challenges to advance their gas sensing performances will also be presented.

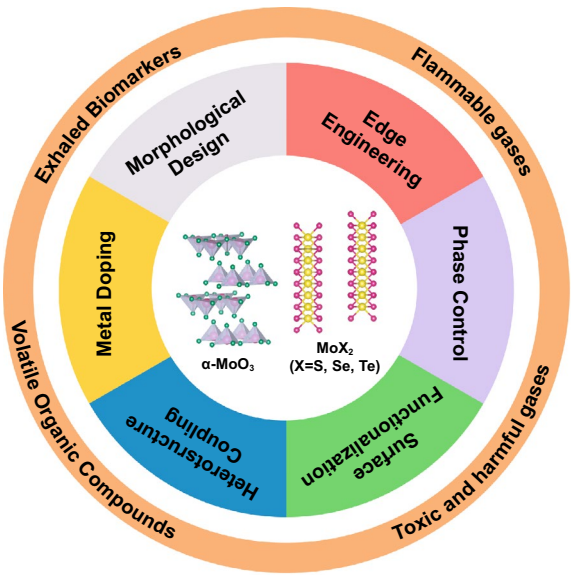

KEYWORDS Molybdenum based; MoO_3; MoS_2; Gas sensing; Advanced strategy

Angga Hermawan, Ni Luh Wulan Septiani, and Ardiansyah Taufik have contributed equally to this work.
✉ Brian Yuliarto, brian@tf.itb.ac.id; Suyatman, yatman@tf.itb.ac.id; Shu Yin, yin.shu.b5@tohoku.ac.jp
[1] Faculty of Textile Science and Engineering, Shinshu University, 3-15-1 Tokida, Ueda, Nagano 386-8567, Japan
[2] Advanced Functional Materials Research Group, Institut Teknologi Bandung, Bandung 40132, Indonesia
[3] Research Center for Nanosciences and Nanotechnology (RCNN), Institut Teknologi Bandung, Bandung 40132, Indonesia
[4] Institute of Multidisciplinary Research for Advanced Material (IMRAM), Tohoku University, 2-1-1 Katahira, Aoba-ku, Sendai, Miyagi 980-8577, Japan

1 Introduction

With advancements in technology, science, and economic mobilities, pollution has become a global concern, especially emissions from vehicles, various industrial processes and transports, agriculture, and residential activities [1–6]. For instance, air pollutions contain many particulate matters and harmful gases directly impacting the environment and human beings [1, 2]. The emissions mostly contain NO_x, CO, SO_2, NH_3, and volatile organic compounds (VOCs) [5], which cause global warming and climate change. Human health is also at risk because these toxic gases enter undetectably (because some gases have colorless and odorless properties) to the body through oral intake, inhalation, and skin contact, causing serious problems that might eventually lead to death [1, 2, 7–9]. According to the World Health Organization (WHO), air pollution is responsible for nearly 800,000 premature deaths per year [10]. Some gases, such as H_2, propane, and methane, are highly explosive without proper handling and safety measures. Therefore, there is a need to develop advanced gas sensor devices to detect these deleterious, dangerous and poisonous pollutants and reduce their damaging effect [4, 11]. Moreover, existing gas sensing technology is forecasted to take a dominant role in health monitoring and disease prediction *by* analyzing exhaled breath biomarkers [12–14].

Gas sensor devices, based on their working mechanism, are mainly classified into chemoresistive, electrochemical, optical, surface acoustic, surface plasmon resonance, and micro-cantilever sensors [15–21]. Among them, the chemoresistive-type gas sensor is the most popular due to its low cost, high sensitivity, fabrication simplicity, ease of miniaturization, and portability, apart from having a well-accepted empirically gas sensing mechanism [22, 23]. The term chemoresistive originates from its working principle in which sensing measurement is based on the change in electrical resistivity upon target gas or chemical exposure. Therefore, the active sensing materials should possess distinguished electrical properties in the different surrounding atmospheres. Metal semiconductors are generally utilized as active materials to sense gases. Initially, the gas sensing materials in sensor device are exposed to the air atmosphere at certain temperatures based on their optimum working conditions. The oxygen molecules (O_2) are then adsorbed onto the surface of materials by catching electrons near the conduction band, creating electron depletion layers (EDLs) in n-type semiconductor and hole accumulation layers (HALs) in p-type semiconductor materials. The adsorbed oxygen transforms into different ion species O^{2-}, O^- and O^{2-} [24, 25]. Due to the charge carrier concentration difference in the material before and after exposure in ambient, the internal resistance is altered.

At this point, the measured resistance represents sensor resistance in the air (R_a) [26, 27]. When the target gas flows and comes into the sensor system, the sensor resistance changes due to the active reaction between ionized oxygen, releasing trapped electrons from the depleted region [27, 28]. The measured resistance in the sensor represents sensor resistance in the air (R_g). Depending on the nature of semiconducting materials, the sensor sensitivity (S) can be calculated by R_a/R_g for n-type and R_g/R_a for p-type. Sometimes when the resistance difference is too small, sensitivity is defined as the relative change in resistance or $S = (R_a\text{-}R_g/R_g) \times 100\%$ for n-type and $S = (R_g\text{-}R_a/R_a) \times 100\%$ for p-type [29]. According to this mechanism, the high sensitivity value is an important parameter for gas sensing materials. Furthermore, operating temperatures, selectivity, response–recovery times, long-term stability, and durability against extreme conditions are crucial for evaluating gas sensor device performances [30].

For decades, studies have been conducted on the potentiality of various types of semiconducting materials for an active component in chemoresistive gas sensors, including metal oxides, sulfides/oxysulfides, nitrides/oxynitrides, and fluoride/oxyfluorides, as well as optimizing their gas sensing properties through advanced strategies [30–34]. Considerable efforts have also been directed toward the investigation of a different class of materials, including molybdenum-based gas sensing materials, which are an attractive group of materials for a wide range of applications, including catalyst, photocatalyst, gas sensor, biomedical therapy, energy storage and conversion, and optoelectronic devices owing to unique tunability of physical and chemical characteristic [32, 35–41]. The most important materials in this group are alpha-molybdenum oxide (α-MoO_3) and molybdenum sulfide (MoS_2). These two are promising candidates for high-performance gas sensor applications because their unique layered 2D structures allow gaseous compounds to access more adsorption sites. This is where the adsorption/desorption process extensively occurs, leading to high

 https://doi.org/10.1007/s40820-021-00724-1

sensitivity [32, 42]. With a high aspect ratio, 2D-structured α-MoO_3 and MoS_2 naturally exhibit high specific surface area that is undoubtedly beneficial for gas adsorption [43]. The synergistic effect of physical, electronic, chemical, and mechanical properties was previously examined for α-MoO_3- and MoS_2-based sensing materials. Furthermore, enormous research strategies have been employed through morphology and crystal phase control, facet engineering, surface functionalization with noble metals, elemental doping, and heterostructures coupling to escalate their gas sensing performance and meet the expected criteria for mass productions. Some previous reviews have been published elsewhere, but they focused on general synthesis and applications of molybdenum-based materials [37, 44]. No recent report has focused on advanced strategies for optimization of their gas sensing performance.

This review provides a comprehensive perspective of α-MoO_3 and MoS_2 as gas sensing materials. The basic crystal structures of these materials and their common properties include physical, electrical, electronics, optical, chemical, and mechanical that strongly correlate to their gas sensing behavior are presented. Afterward, the focus is on the most recent and advanced strategies to optimize gas sensing performances of α-MoO_3 and MoS_2 in detecting various harmful gases. It is noteworthy that the recent progress on the gas sensing performance of other molybdenum-based materials, such as $MoSe_2$, $MoTe_2$, Mo_2C, and MoC, is briefly discussed to encourage further extensive development. This review also summarizes molybdenum-based gas sensing materials and an overview, including challenges and future works.

2 Molybdenum Oxide (MoO_3) Gas Sensing Materials

Molybdenum oxide (MoO_3) is one of the n-type metal oxide semiconductors with a band gap ranging from 2.39 to 2.9 eV [45–47]. This oxide has unique optical and electronic properties, layered structure, and good catalytic properties suitable for photodevice, energy storage, and catalyst [43]. Furthermore, its intrinsic semiconductor property with high sensitivity to the presence of gas explains its wide use as a gas sensor material [43, 48]. Regarding crystal structure, MoO_3 exist in three different types of structures depending on growth temperature, pressure, and impurities [43]. The structures are orthorhombic (α-MoO_3), monoclinic (β-MoO_3), hexagonal (h-MoO_3), and ε-MoO_3, as shown in Fig. 1. However, α-MoO_3 is the most popular and widely used since it is stable thermodynamically and often formed at high temperatures. In this type of structure, the distorted MoO_6 octahedral are arranged in layers toward the b axis with corner and edge-sharing [49]. This layered structure is supported by Mo–O's asymmetry coordination, where the distance between them is varied from 1.67 to 2.33 Å [50]. In the gas sensor application, this phase is popular due to its high stability. The other phases, β-MoO_3 and h-MoO_3, are metastable and need a complex preparation procedure to prepare [51]. In general, β-MoO_3 is prepared by the cation exchange approach, while h-MoO_3 preparation involves alkaline earth metal [52]. Despite the superior nature of the catalyst, β-MoO_3 is a rarely found in gas sensor application. Regarding h-MoO_3, several studies have utilized this phase to detect ethanol, formaldehyde, acetone, NH_3, and H_2. In terms of electronic properties, the n-type semiconductor properties of MoO_3 are supported by the presence of oxygen vacancies, which induce localization of electrons on the surface [53]. These electrons fill the 4d state of Mo in the Mo–Mo bond, and the state is located in the MoO_3 band gap. However, the number of oxygen vacancies strongly determines the electronic properties of MoOx and according to previous studies, MoO_2 has metallic properties [53, 54]. In this section, the use of MoO_3 semiconductors as gas sensors is reviewed. The development of MoO_3 modifications to improve its performance as a gas sensor, such as morphology modification, metal decorated, elemental doping, and heterostructures, are also discussed in detail.

From the literature research obtained from the Web of Science database as shown in Fig. 2, we discovered the total number of publications related to MoO_3 based gas sensor is 265, with the first report of MoO_3 was published in 1992. After a decade, the number of work is still few which the most of the work focused on thin-film preparation. The number of detected gas is limited to non-VOCs gas. Early investigations demonstrated MoO_3 thin-film deposition method in electronic substrate via physical sputtering. Also, the intercalation of polymeric materials guest on interlayer MoO_3 host became a major approach for increasing MoO_3 gas sensing properties. Because of the development of sol–gel chemistry as a novel wet preparation of inorganic solid, various morphological nanostructured MoO_3 such as nanoparticles, nanobelts, and nanoplatelets have been successfully synthesized within the time frame of 2010–2014. This approach

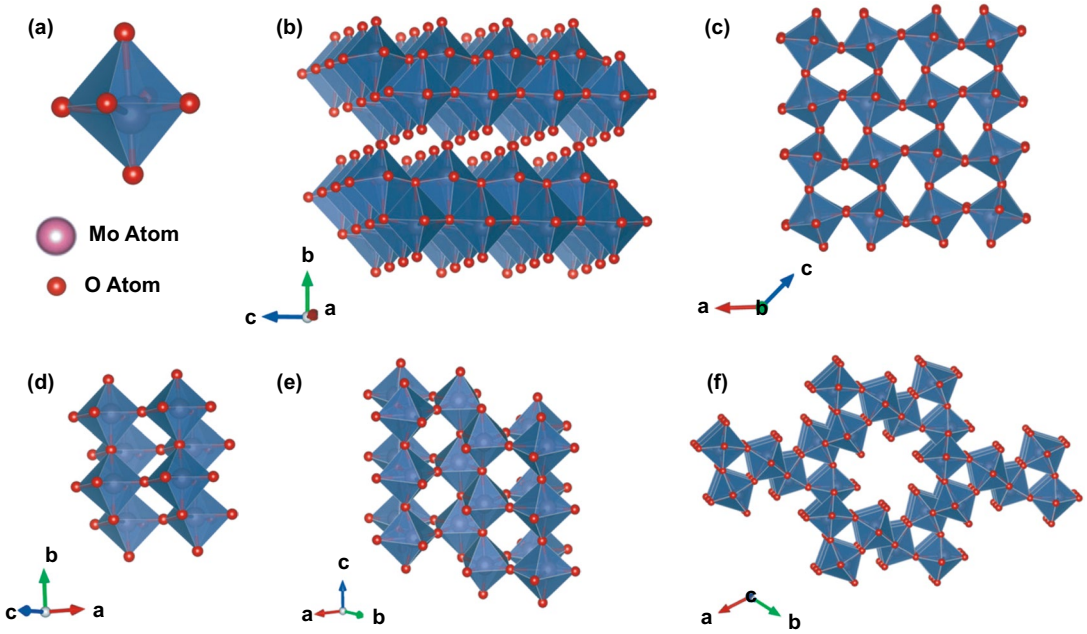

Fig. 1 **a** MoO_6 octahedra in the thermodynamically stable α-MoO_3 phases. **b** Orthorhombic α-MoO_3 with a layered structure. **c** Metastable monoclinic β-MoO_3. **d** ε-MoO_3, also known as MoO_3-II. **e** Metastable h-MoO_3. **f** Tunnel structure along the c-axis of h-MoO_3 unit cell. Reproduced with permission from Ref. [43]. Copyright 2017 Wiley-VCH

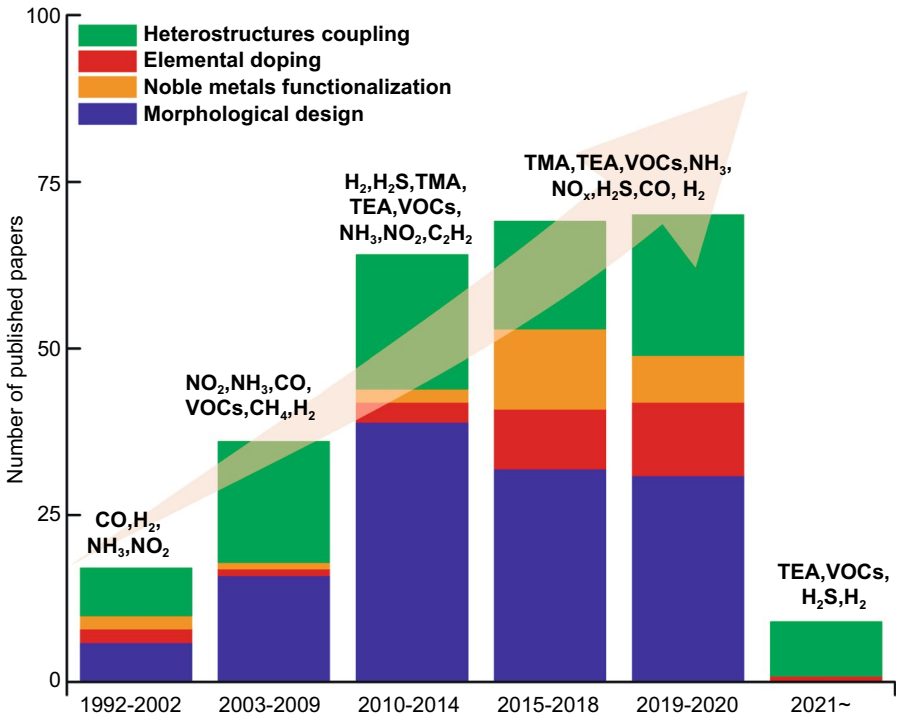

Fig. 2 Number of publications examining various strategies to improve gas sensing properties of MoO_3 toward wide range of gases. Data are collected from Web of Science (WoS) as of April 2, 2021, with the keyword "MoO_3 gas sensing." Both experimental and computational works are included. Review and perspective articles are excluded from the collected data. TMA and TEA stand for trimethylamine and triethylamine, respectively

 https://doi.org/10.1007/s40820-021-00724-1

attracted many researchers in the gas sensing field, as demonstrated by the number of publications that exceeded other approaches. We have recognized that the acidity of MoO_3 is effective in detecting gases with basic nature, such as the gas with an amine group (TMA and TEA). The noble metals functionalization and elemental doping strategies have also been getting more popularity in recent years and are predicted to compete with the other 2 approaches. We will be discussing the development of each strategy in the following section.

2.1 Morphological Design

The morphology design is essential in improving gas sensor performance because it strongly determines the active sites for surface reaction. Several efforts to design MoO_3 from zero dimensional to hierarchical three dimensional have been recently reported. Each dimension has its role in enhancing sensor performances. Zero-dimensional nanomaterials commonly referred as quantum dots (QDs), typically semiconductor materials with a size less than 10 nm. This nanoscale size of MoO_3 allows their electrons to be depleted entirely by oxygens, thus significantly improve the sensitivity [55]. The quantum confinement that occurs in quantum dots also makes their bandgap tunable depending on their size. Based on its property, its sensing performance can be altered by altering its size [55–57]. Moreover, the reactivity of the QDs is considerably high due to the many defects or oxygen vacancies present on their surface, increasing active sites for oxygen adsorption. In general preparation of MoO_3 or MoO_x QDs, exfoliation process of MoS_2 or MoO_3 precursor is involved in the presence of an oxidant such as H_2O_2 that act as an exfoliating agent [58–60]. When MoS_2 precursor is dispersed in the aqueous solution containing H_2O_2, the oxidant provides the excess of oxygen that induces exfoliation and oxidation of Mo^{4+} to its higher oxidation state. It was also reported that short oxidation of an aggressive oxidant of $KMnO_4$, followed by oxidation by H_2O_2 in hydrothermal conditions, will also produce high quality of MoO_x QDs [61]. Moreover, post-treatment, such as thermal exfoliation and surfactants addition, were reported to control the size and stabilize the QDs [59]. Those techniques produced the QDs with the size in the range of 2–6 nm. Aside from MoS_2, MoO_3 powder was also reported as a precursor for the formation of MoO_x QDs. The exfoliation of MoO_3 can be realized by dispersing the oxide in organic solvents such as dimethyl sulfoxide (DMSO) and N-methyl-2-pyrrolidinone (NMP) with the help of ultraviolet (UV) light [60, 62]. Although many reports in MoO_x QDs are available, their exploitation as gas sensor materials cannot be found. Therefore, the research on this topic is still widely opened. The QDs can be present as supporting material for other oxides or carbon nanomaterials.

Unlike zero-dimensional MoO_3, other dimensions of this oxide, such as one dimensional (1D), two dimensional (2D), and three dimensional (3D), were widely examined as sensitive materials for gas sensors. 1D MoO_3 is a popular gas sensor due to its high surface-to-volume ratio, high exposed facet, and high chemical stability [63–65]. Controlling their diameter close to the Debye length (λ_L) can give various conduction states improving the sensing performances significantly. Moreover, the back-to-back *Schottky* barrier can be generated by contacting two or more random oriented MoO_3 [66, 67]. The synergistic effect between the wide depletion layer on the 1D surface and the back-to-back *Schottky* barrier is believed as a reason for their excellent performances. In the case of MoO_3-based gas sensors, several 1D nanostructures have been reported, including nanowires, nanorods, and nanobelts. Self-assembly α-MoO_3 nanowires on a flexible hydrophobic substrate for H_2 sensing was reported by Luo et al. [48]. Since MoO_3 tends to form 2D in its growing process, modifications of the synthesis method need to be carried out. The nanowire was firstly prepared by hydrothermal method at 260 °C for 96 h. The formation of orthorhombic phase α-MoO_3 nanorod occurred with a diameter of ~ 300 nm and a length of ~ 1 mm. The authors define its sensing performance by sensitivity factor, β, $(R_{air}\text{-}R_{gas})/R_{air}$. At room temperature, the resulted α-MoO_3 displayed a good response toward 1.5% of H_2 with a sensitivity factor of 0.85. Moreover, the materials can detect the gas in 3 s and need only 2.7 s to recover with remarkable selectivity. The excellent performances of the α-MoO_3 nanowire are caused by the Mo^{5+} species contained in the oxide. Since this species has a stronger bonding with adsorbed oxygen, it provides more active sites for gas sensor reactions. Other 1D nanorods of α-MoO_3 were prepared by Cao et al. [68] using a similar method with the assistance of hydrochloric acid (HCl) and cetyltrimethylammonium bromide (CTAB) at 180–190 °C for 24 h. The process led to nanorod formation

with a diameter and length in the range of 100–200 nm and 1–3 μm, respectively. The resulting nanorod shows a response of 35 toward 400 ppm ethanol at a relatively high optimal temperature of 350 °C.

VOCs sensor based on α-MoO_3 nanobelts was prepared by Jiang et al. [69] and Mo et al. [70] using a similar method, hydrothermal. Both groups used ammonium heptamolybdate tetrahydrate as a Mo source with different acids. Nanobelts of α-MoO_3 with a width of 200 nm and length of ~ 6 μm were produced by a hydrothermally heated Mo precursor solution containing HNO_3 at 180 °C for 36 h. The nanobelts show a response of ~ 3 to 100 ppm of xylene at 206 °C with the response and recovery times of 7 and 87 s, respectively. The addition of HCl as a pH modulator and hydrothermal condition at 160 °C for 15 h resulted in nanobelts structure with a width of 180 nm. Mo et al. reported that the prepared oxide displayed good performance as an ethanol sensor at 300 °C with a 50–800 ppm detection range. At its optimal temperature, the oxide has a response and recovery times in the range of 10–40 and ~ 4–70 s, respectively. Interestingly, the sensing mechanism of α-MoO_3 is mainly contributed by surface lattice oxygen. The ethanol target is oxidized by the oxygen lattice, causing electron transfer to the metallic core and producing oxygen vacancies. This phenomenon changes the oxide resistance that is used as a sensor signal.

Naturally, MoO_3 with orthorhombic crystal structure or α-MoO_3 has a double-layer structure [43]. This feature of α-MoO_3 offers the easiness to produce 2D morphologies, including a thin layer via the exfoliation process. The 2D material itself is considered a promising class of materials due to its unique properties, the high surface area that provide a huge number of active sites, and the possibility for surface modification as needed [71, 72]. As sensitive materials for gas sensors, increasing its affinity to target gas combine with the high surface area leads to superior gas sensor performance. Moreover, in the α-MoO_3 case, the distance between its layer provides an additional diffusion path for gases to reach accessible sites. Several works report on the exfoliation of bulk α-MoO_3 to 2D structures, such as nanoflakes [72, 73] and nanosheets [74]. Generally, the exfoliation process is successfully executed with ultrasonication assistance in the mixture of ethanol/water medium. Ji et al. [74] reported that nanosheets of α-MoO_3 could be produced via exfoliation in the water/ethanol mixture with the ratio of 50%. Another liquid, such as DMSO, DMF, and IPA, produces a many layers of nanoflake. The nanosheets have superior alcohol sensing performance compared to the nanoflakes, with a response value of 31 at 300 °C to 100 ppm of alcohol vapor. The nanosheets with a higher surface area than the nanoflakes provide more active sites for surface reaction. Rahman et al. [75] also performed exfoliation using a different route. The CVD method was used to deposit α-MoO_3 on the substrate. This technique produces nonstoichiometry of nanoflakes of α-MoO_{3-x} with many Mo^{5+} and oxygen vacancies on its surfaces. Since oxygen vacancies are the main key in the sensing mechanism of layered α-MoO_3, the more vacancy, the higher the performance will be. The nanoflakes show good performance to NO_2 and H_2S at 250 °C with excellent selectivity.

Surface modification by enriching oxygen vacancy on MoO_3 surface for TMA sensing was carried out by Shen et al. [76] The ultrasonication of bulk MoO_3 in the solution containing methanol and H_2O_2, followed by solvothermal at 180 °C for 12 h were performed to exfoliate the bulk oxide. The nanosheets with a thickness of 28 nm and rich in oxygen vacancies were obtained after calcining the solvothermal product at 400 °C. The abundance of oxygen vacancies provides many delocalized electrons that support charge transfer between the surface and TMA. These nanosheets detect 50 ppm of TMA at the optimal temperature of 133 °C with a response of 198. The different surface modifications with different results in types of gas sensor behavior were observed by Bisht et al. [77]. In their work, α-MoO_3 was deposited using the pulsed laser deposition (PLD) technique on Si/SiO_2 substrates. By varying the number of pulses, 2D, ultrathin-film (UTF) and thin-film (TF) α-MoO_3 were produced with the thickness of 6, 18, and 80 nm, respectively. Interestingly only TF exhibits n-type behavior while 2D and UTF exhibit p-type behavior during NO_2 exposure at 100 °C. Two reasons are believed to cause this unusual behavior of 2D and UTF; first, the high number of oxygen species on the surface of 2D and UTF induce the inversion layer resulting in the domination of holes in their conduction process. Second, the *Schottky* barriers at metal-α-MoO_3 contact of 2D and UTF are higher than that of TF preventing the electrons transfer from metal to α-MoO_3 and allowing holes to pass the conduction channel. At 100 °C, the 2D α-MoO_3 shows the highest response to 10 ppm of NO_2 with a response value of 25% and response time of 200 s.

Several studies show that low dimensional of MoO_3, such as nanorods [78–80], nanowires [48, 81], nanobelts [82, 83], nanoflakes [26, 84], and nanosheets [45, 49, 85] have good

 https://doi.org/10.1007/s40820-021-00724-1

performance as sensitive materials for toxic gas detection. However, some works reported that hierarchical 3D structures assembled by their low dimensional form offer higher performance due to their low density, high surface area, and porosity that allow more adsorption sites [86, 87]. Huo's group compared the TEA sensor performance of α-MoO_3 nanoparticles, nanobelts, and nanobelt-assembled hierarchical flower-like [87] at 170 °C. α-MoO_3 flower-like show superior response of 931.2 to 10 ppm TEA, 8.1 and 33.7, higher than the value generated by nanobelts and nanoparticles, respectively. The high performance is attributed to the combination of high surface area and high (010) facet. Some studies also report the active facet of (010), especially to TEA [88, 89]. The flower-like α-MoO_3 produced by Huo's group also shows higher performance than ultralong α-MoO_3 nanobelts and nanorod, which show the highest performance to detect TEA at 240 and 300 °C [78, 83], respectively, as shown in Fig. 3. The microboxes of α-MoO_3 composed of nanosheets are obtained using $MnCO_3$ microboxes as a template [90]. In this case, the template was removed by an acid treatment. As a gas sensor, the boxes show good performance in detecting 100 ppm ethanol at 260 °C with response value and response time of 78 and 15 s, respectively. Its performance is higher than other works that developed sponge-like nanorods, nanofibers, and nanobelts α-MoO_3 [89, 91].

In the case of 3D α-MoO_3, the gas sensor performances also depend on its assembly units. For instance, Ji et al. prepared a hierarchical 3D structure assembled from nanosheets with three different thicknesses, 65–80, 30–40, and 5–8 nm [85]. The gas sensor measurements to 300 ppm of ethanol at 300 °C show the thinnest sheets show the highest performances due to its relatively larger surface area. Furthermore, the two assembly units, nanofibers and nanosheets, assemble a 3D sphere of α-MoO_3 were prepared by Ji et al. as

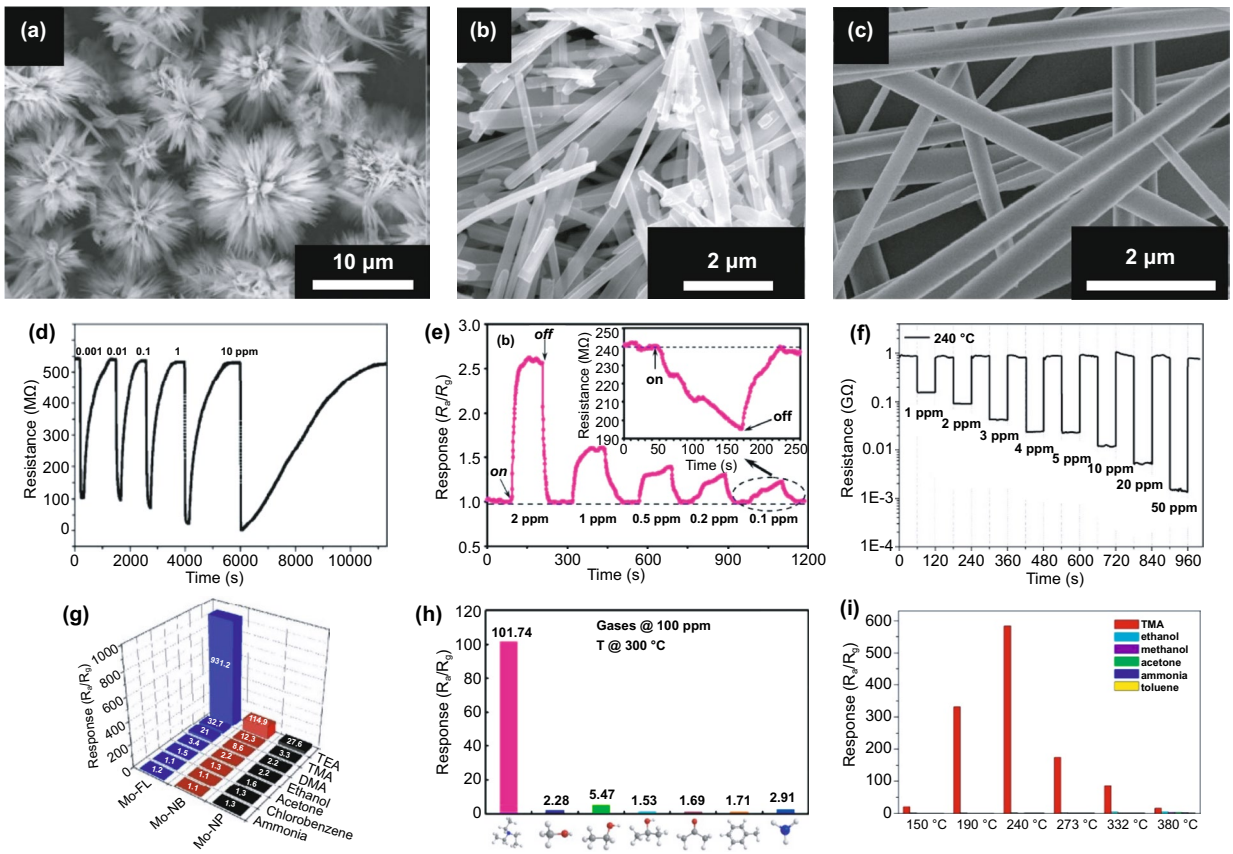

Fig. 3 α-MoO_3 flower-like showing superior TEA sensor performance at 170 °C (**a, d, g**) compared to α-MoO_3 nanorod that has optimal temperature of 300 °C (**b, e, h**) and α-MoO_3 nanobelts that have optimal temperature of 240 °C (**c, f, i**). (**a, d, g**) are reproduced with permission from Ref. [87]. Copyright 2015, The Royal Society of Chemistry. (**b**, **e**, **h**) are reproduced with permission from Ref. [78]. Copyright 2019, Elsevier. (**c**, **f**, **i**) are reproduced with permission from Ref. [26]. Copyright 2016, Elsevier

ethanol sensors [92]. The nanosheets show a higher response to 400 ppm of ethanol at 300 °C than the nanofiber one due to their higher surface area and there are many intersections between individual sheets that force gas to adsorb on the surface effectively. However, the higher diffusion rate and lower potential energy of the nanofiber-assembled sphere lead to a faster response.

The morphology design apparently can reduce the optimal temperature which has an impact on increasing sensor stability. Efforts to reduce the working temperature of a pure MoO_3-based gas sensor can be done by making the 2D structure as thin as possible. The thin 2D structure has abundant defects and oxygen vacancies providing a large amount of electron delocalization so that the reactivity increases at lower temperatures. However, another challenge in the utilization of this oxide is the negative effect of humidity. High humidity generally reduces sensor performance because moisture on the surface can hinder oxide and target gas interaction. Therefore, other efforts such as modification with noble metals, elemental doping, and creating heterostructures can minimize the influence of humidity.

2.2 Surface Functionalization with Noble Metals

Improvement in the gas sensor performance can be achieved by introducing a noble metal on the metal oxide surface. Apart from their action as active sites, noble metals with high catalytic activity also reduce the activation energy of a gas, leading to an increase in adsorption rate and lowering operating temperature [93–95]. Improvement of sensor performance due to the functionalization of noble metal is attributed to its ability to induce electronic and chemical sensitization. Fermi level differences between noble metal and metal oxide generate a Schottky barrier at the interface that is sensitive to the presence of gas (electronic sensitization). For instance, some noble metals, such as Au [26, 45, 96–98], Ag [99], Pt [100], and Pd [101], were reported to enhance gas sensors based on MoO_3. These metals have a higher work functions of 5.1 [97, 102], 4.72 [103], 5.6 [104], and 5.2 eV [105], respectively, compared to work function of MoO_3 that is 2.9 eV [106]. These differences induce the occurrence of electronic sensitization. Moreover, the dispersion of noble metals on the surface of metal oxides induces spill-over effects that help to increase the rate of surface reactions, leading to reduce response and recovery times. This chemical sensitization also helps to convert unreactive gas into a reactive form and improve selectivity [107–110]. Figure 4 shows an illustration of chemical and electronic sensitization in noble metal decorated MoO_3. Under an air atmosphere, the noble nanoparticles on MoO_3 surface act as an active site for O_2 dissociation. During gas exposure, for example R_2, the noble metal dissociates them to R, which is more reactive than R_2, as seen in Fig. 4a. This spill-over effect increases the reaction rate that resulting in reduced response time and lowered operating temperature. As mentioned earlier, electronic sensitization occurs due to the difference in work function between noble metal and MoO_3. Almost all noble metals have a work function higher than that of MoO_3. Right after MoO_3 makes contact with noble metals, electrons will flow from MoO_3 to noble metal along with Fermi level alignment leading to upward bending of MoO_3 (Fig. 4b). The band bending is associated with barrier potential qV at the noble metal/MoO_3 interface that can be changed during the surface reaction as shown in Fig. 4c. The combination of chemical and electronic sensitizations results in high sensitivity, low temperature, and fast response.

Decoration of Au on MoO_3 successfully improved toluene [96], xylene [96], ethanol [45], H_2S [26, 111], and 1-butylamine [106] sensing performances. As toluene and xylene sensors, the α-MoO_3 hollow spheres with 450 nm in diameter have been prepared by the solvothermal method,

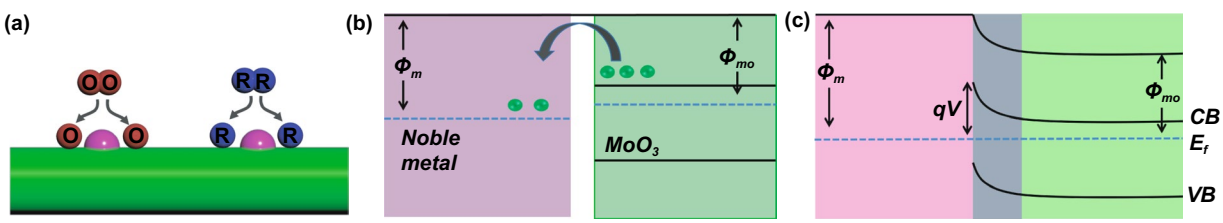

Fig. 4 **a** Spill-over effect or chemical sensitization induced by noble metal on the surface of MoO_3. **b, c** Electron transfer from MoO_3 to noble metal right after making contact along with Fermi alignment that generates Schottky barrier at the interface of noble metal/MoO_3

 https://doi.org/10.1007/s40820-021-00724-1

followed by chemical reduction of Au at 120 °C. The Au nanoparticles have a diameter in the range of 10–25 nm. The higher numbers of chemisorbed oxygens on Au decorated α-MoO_3 hollow sphere than in its pure one increase response 4.6 and 3.9 times at 250 °C to 100 ppm of toluene and xylene, respectively, higher than the pure one at 290 °C [96]. Aside from operating temperature, the presence of a certain amount of Au nanoparticles also reduces response times from 19 and 6 s to 1.6 and 2 s for toluene and xylene, respectively. Moreover, Au preference to coordinate with the aromatic ring group may improve Au–MoO_3 selectivity to toluene and xylene. The Amount and distribution of Au or noble metal also affect the sensing performance. A high amount and good dispersion of noble metal nanoparticles on the surface of metal oxide raise the catalytic effect yet cover the active sites of oxide leading to decreased performance [112]. A low amount of the metal is distributed sparsely, causing a lower catalytic activity and synergetic effect. Therefore, the proper ratio of metal/metal oxide is vital for achieving the best sensing performance. In the previous case, optimal amount of Au to deliver the highest performance was 2.04% of α-MoO_3. A different shape leads to a different sensor preference. 4 wt% of Au decorated MoO_3 nanosheet was reported to sense 200 ppm of ethanol better at its optimum temperature of 280 °C with the response and recovery times of 14 and 5 s, respectively [45]. The nanosheet with the size of 600 nm was prepared using a solvothermal method, while 10–15 nm of Au decoration was performed using the chemical reduction technique. However, the pure MoO_3 has a lower operating temperature, though the response value is much lower than the decorated one. The same amount of Au was used to decorate 200 nm in a width of MoO_3 nanobelt and was reported selectively in response to the presence of 1-butylamine [106]. The material preparations were similar to the previous work [45]. Compared to the pure MoO_3 nanobelt with an optimal operating temperature of 340 °C, the Au decorated nanobelt shows the best performance at 240 °C with a response value of ~ 300. The high selectivity to 1-butylamine is caused by a nitrogen atom in 1-butylamine that has electrons lone pair and bind with acid-Lewis site of Mo ions (Fig. 5a). Moreover, the hydrogen atoms in the gas also support the secondary dehydrogenation producing more electrons. However, strong interaction between the Au decorated MoO_3 and the gas result in a long recovery. Hence the response time was much shorter than recovery time in both pure and decorated cases, as seen in Fig. 5b [97, 113, 114].

A lower operating temperature is achieved after an additional of Ag to α-MoO_3 nanorods. The nanorods possess the length and diameter of 10 μm and 200–300 nm, respectively. The Ag nanoparticles on the nanorod surface has a size of ~ 20 nm. The structure was obtained by the solvothermal method to produce nanorods, then Ag reducing by wet chemical reduction at 50 °C. Also, 100 ppm of TEA was detected with the response value of 400.8 at 200 °C with high selectivity [99]. This value is three times greater than its pure counterpart and detects the gas within 3 s. Similar to the previous case, the strong interaction between amine-contained gas and Mo ions leads to an incomplete recovery. To solve the problem, He et al. [101] proposed short-time pulse heating at high temperatures and established that pulse heating at 300 °C for 1 min completes the recovery in 107 s. At the same temperature, Pd-loaded MoO_3 flower-like nanobelts detect NO_2 gas with good selectivity [101]. The nanobelt was prepared using chemical spray pyrolysis (CSP) on a glass substrate with $MoCl_5$ as a Mo source. The Pd loading was done by dipping the MoO_3 film in PdCl solution several times and heat at 200 °C to remove the chlorine compound. The pure nanobelts achieves a response of 68% to 100 ppm of NO_2 at 200 °C. After Pd's addition, the response value increased to 95.3%, with response and recovery time of 74 and 297 s, respectively. The higher affinity of NO_2 causes the high selectivity to NO_2 compared to pre-adsorbed oxygen and other gases; hence the NO_2 chemisorption is preferentially on the Pd-loaded MoO_3 surface. In another case, the addition of Pt nanoparticles on the α-MoO_3 nanobelts effectively detected formaldehyde at room temperature [100]. The nanobelts with 200–400 nm in width were prepared using a hydrothermal method, while Pt decoration was performed using the chemical reduction technique. A proper amount of Pt on the nanobelts had a response of 39.3% to 200 ppm of formaldehyde with a response and recovery times of 21.4 and 16.6 s, at room temperature. The presence of Pt nanoparticles raises the response by almost six times of the bare α-MoO_3.

Functionalization of MoO_3 with noble metal has been proven to increase response and decrease response time. Although the optimal temperature of MoO_3 is lower with noble metal functionalization, the reported optimal temperature is still relatively high, which is in the range of

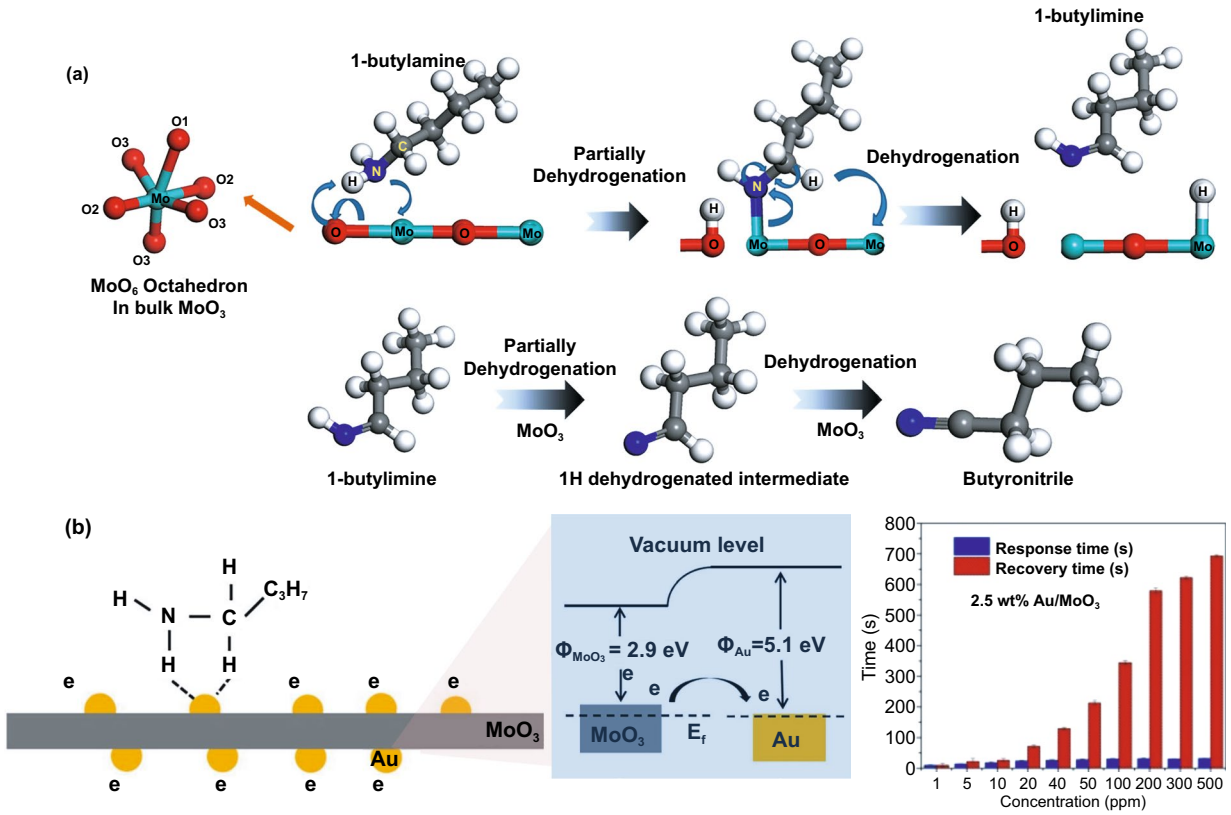

Fig. 5 **a** Schematic diagram of the sensing mechanism toward 1-butylamine on the MoO_3 surface. The dehydrogenation pathway and the electron transfer to the Mo site are displayed. The liberated proton over Mo and the adsorption OH are assumed to adsorb as water. **b** Proposed mechanism of the adsorbed dehydrogenation process on Au/MoO_3 nanocomposites and its consequence to response and recovery time. Adapted with permission from Ref. [106] Copyright 2021 Elsevier B.V

200–250 °C. The combination of ultrathin 2D MoO_3 and noble metal has the potential to be a superior gas sensor at low temperatures. In addition, this strategy has not been able to overcome the negative effect of humidity. In general, the best performance of gas sensors based on noble metal functionalized MoO_3 is obtained with a humidity of less than 40% and significantly decreases with increasing humidity [26, 99, 100, 106, 115]. Therefore, further exploration to overcome these challenges needs to be carried out in the future.

2.3 Elemental Doping

Aside from noble metals, other metals are also useful in improving MoO_3 sensing performance. For instance, small quantities of iron (Fe), nickel (Ni), zinc (Zn), and chrome (Cr) raised the sensor response significantly. The possible reasons for the sensing improvement are believed to be as follows. First, metals increase the porosity of the metal oxides. Second, the high oxidation state of Mo allowed many lower-state metals to replace the Mo site and create an acceptor level. This substitution increases the resistance hence modulating sensing performances. Third, charge balancing compensation generates the oxygen vacancies that increase oxygen chemisorbed species on the oxide surface [116–118]. The metal-doped MoO_3 preparation and its sensing performance are discussed efficiently in this section.

Fe-doped MoO_3 with nanobelts and nanoarrays morphologies were prepared by Ruan and Cao groups, respectively [119, 120]. The works were motivated partly by the similarity of the ionic radius of Fe^{3+}, 0.064 nm, and Mo^{6+}, 0.069 nm, which allow substitution with a minimal defect in the oxide crystal structure. The MoO_3 nanobelts were prepared using a hydrothermal method with ammonium molybdate tetrahydrate as a Mo source in the water medium [119]. Fe doping was completed by mixing the Mo source

 https://doi.org/10.1007/s40820-021-00724-1

with iron nitrate nonahydrate during solution preparation. The pure nanobelts have a width and length of 350 nm and 8 μm, respectively. Interestingly, higher Fe contents increase the tendency of MoO_3 to form nanosheets structure. However, with the variation of Fe content in the range of 1–15 wt%, 5 wt.% became the optimal amount in detecting xylene. The optimal temperature for xylene detection is 206 °C, with a response value of 6.1. The response and recovery times were recorded as 20 and 75 s, respectively. Moreover, the pure nanobelts show a response value of 2.9 at the same temperature to 100 ppm xylene. In another case, Cao's group prepared MoO_3 nanoarrays using the solid-state chemical reaction method with a similar Mo source as Ruan's experiment [120]. The Mo and Fe sources were mixed mechanically with an agate mortar in the presence of PEG-400 and oxalic acid. The mixture was heated at 60 °C for 24 h and calcined at 450 °C for 1 h, resulting in nanoplate arrays of MoO_3. The Fe^{3+} doping made the plate thinner due to the lattice distortion that hinders crystal growth. In this case, the Fe amounts are ranged between 0.1 and 0.7 wt%, and 0.3 wt% was the optimal amount for the best structure and sensing performance. The optimal temperature for MoO_3 nanoplates array was 370 °C, 30 °C higher than Fe-doped MoO_3. Although it works at high temperatures than those in nanobelts case, it shows a response to 100 ppm of xylene of 28.1 with the response and recovery times of 2 and 21–33 s, respectively. The excellent performances of Fe-doped MoO_3 are caused by the more oxygen vacancies available to facilitate more chemisorption as shown in Fig. 6a. The fact is strengthened by the density functional theory (DFT) calculation conducted by Lei et al. [121] The result shows that monolayer MoO_3 is insensitive toward oxygen molecule and Fe doping increase its molecule adsorption capability. The isosurface analysis (Fig. 6b) found that the oxygen was chemisorbed by capturing 0.2 e from one Fe-doped MoO_3. Upon exposure to xylene, oxygen molecules interact with it and consequently released the captured electrons to Fe-MoO_3. Moreover, the sensing material exhibited a stable response value up to 30 testing days (see Fig. 6c, d).

Ni-doped MoO_3 detects 100 ppm of xylene at the optimal temperature of 250 °C [116]. In Jiang et al. [116] synthesis procedure, the 800 nm in diameter of nanosheet-assembled MoO_3 spheres were obtained by the solvothermal method. With a similar procedure, adding a small amount of

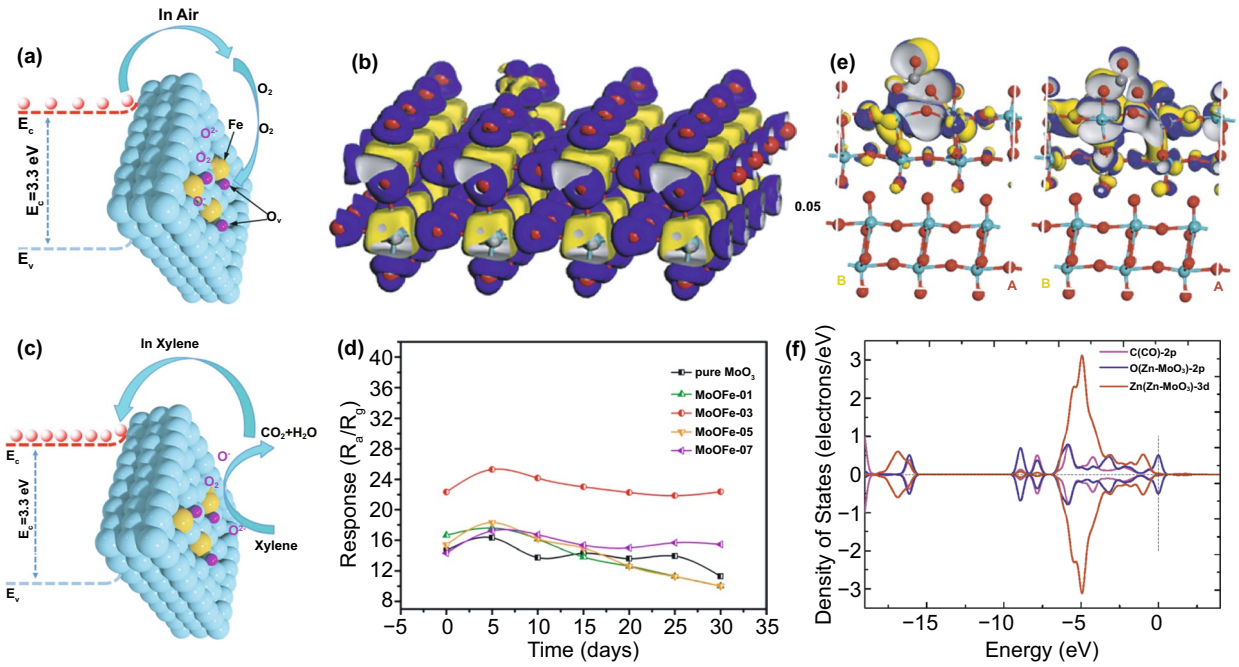

Fig. 6 Schematic diagram of **a** Fe-doped MoO_3 sensor and **b** its electronic density difference isosurfaces when exposed to oxygen molecules. **c** Schematic diagram and **d** long-term stability of Fe-doped MoO_3 sensor when exposed to xylene. (**a, c, d**) are reprinted with permission from Ref. [120]. Copyright 2020, Elsevier B.V. **b** is reprinted from Ref. [121]. Copyright 2020, Elsevier B.V. **e** HOMO (right) and LUMO (left) and **f** PDOS of CO-adsorbed Zn–MoO_3 (010) adsorption system. Reproduced from Ref. [122] with permission. Copyright 2020, Elsevier B.V

Ni results in the smaller pompon-shaped sphere. The smaller size indicated the role of Ni as a crystal growth inhibitor. Ni^{2+} diameter (0.072 nm), which is higher than Mo^{6+}, causes distortion that inhibits the crystal growth. The smaller Ni-doped MoO_3 size improves the response value to 62.61, 18 times higher than the MoO_3 nanosphere with good selectivity. The pompons structure detects xylene in only 1 s. The high response is attributed to the more Schottky contact by the small pompons, increasing the resistance. According to Ruan's group, adding 5 wt% Zr to the MoO_3 matrix changed nanobelts to nanosphere structure [123]. In the absence of Zr, α-MoO_3, which was synthesized using the solvothermal method at 180 °C for 36 h, has a nanobelt morphology with a length and width of 6 μm and 200 nm, respectively. A similar method was used with the addition of 5 wt% Zr to the Mo solution during synthesis. The presence of α-MoO_3 spheres assembled by nanobelts with a size of 600 nm was observed, indicating the role of Zr as a morphology modifier. As a xylene sensor, the presence of Zr increases the response of α-MoO_3 to 100 ppm xylene by three times at 206 °C. Furthermore, α-MoO_3 shows excellent selectivity to xylene compared to benzene and toluene due to two methyl groups in xylene. This makes it more reactive to Zr, which has good catalytic activity.

Several studies have reported the improvement of sensor performance of α-MoO_3 to amine compounds, such as triethylamine (TEA) and trimethylamine (TMA) by involving chrome (Cr) [124], cerium (Ce) [125], and tungsten (W) [118] as metal doping. Li et al. [124] reported the fabrication of the nanorods structure of Cr-doped MoO_3 by mixing MoO_3 powder produced through solvothermal followed by annealing processes. Doping Cr inhibits the growth of α-MoO_3 grains, resulting in shorter nanorod than that of pure MoO_3. A response value of 150.25 was achieved at 200 °C to 100 ppm TEA with a response and recovery of 7 and 80 s, respectively. The relatively short recovery is supported by pulse heating at 300 °C. In TMA detection, Li et al. synthesized α-MoO_3 nanobelts doped with Ce and W [118, 125]. Ce-doped α-MoO_3 and W-doped α-MoO_3 were obtained through a solvothermal process in the presence of cerium nitrate and Na_2WO_4 as sources of Ce and W, respectively. Ce and W doping result in different optimal temperatures of 240 and 280 °C, respectively. α-MoO_3 nanobelts show a response of 4.7 to 50 ppm TMA at the optimal temperature of 280 °C, while Ce-doped α-MoO_3 and W-doped α-MoO_3 show a response of 17.4 and 13.8 at their optimal temperature, respectively. Ce and W substitution at the Mo lattice site increases oxygen vacancies, improving the TMA sensor performance. Furthermore, the relatively short recovery times of 20 and 11 s for Ce and W doping, respectively, show superior amine compound detection performance.

The reducing gases, such as CO and H_2S, are also reported could be detected by modifying MoO_3 with metal doping. Bai et al. [126] examined Cd-doped α-MoO_3 as an H_2S sensing material. Cd-doped α-MoO_3 nanobelts with a 200–800 nm width and a length of several micrometers were synthesized using a simple solvothermal method at 120 °C for 24 h. Analysis using photoluminescence (PL), XRD, and Raman spectroscopy showed Mo^{6+} substitution with Cd^{2+} generates defects and oxygen vacancies. Furthermore, Cd also narrowed the bandgap of α-MoO_3, which was strengthened by the DFT study. These phenomena are the reason for the three times increase in the response of Cd-doped α-MoO_3 to 100 ppm H_2S at 140 °C (378.5), where pure α-MoO_3 performs optimally at 170 °C (123.4). In the case of CO detection, α-MoO_3 is modified by metal Zn. Zn-doped α-MoO_3 was prepared using a solvothermal method with a pH adjustment of 2. Wang et al. [122] reported the formation of a hierarchical micro flower α-MoO_3 with a size of about 2 μm that is composed of nanosheets. The presence of Zn in the α-MoO_3 lattice inhibits grain growth, leading to thinner individual nanosheets. Based on DFT calculations as displayed in Fig. 6e, f, the interaction between CO and α-MoO_3 is classified as a weak interaction. In Zn presence, chemisorption of CO on the oxide surface occurs with a charge transfer of 0.451e. Additionally, the narrowing bandgap from 1.447 to 1.167 eV after Zn addition leads to an increase in the conductance of α-MoO_3. This narrowing is believed to increase the α-MoO_3 response four times at a temperature of 240 °C, where pure α-MoO_3 has an optimal temperature of 260 °C. In another report, Zn metal was also used to dope α-MoO_3 and work as an ethanol sensor at 240 °C [127]. The response of 321–1000 ppm of ethanol was observed during the measurement. However, this value is 15 times higher than that of pure α-MoO_3.

Based on the above discussion, metal doping generally has a function as a modifier of the morphology of MoO_3. The improved performance of the sensors appears to be due to an increase in the number of oxygen vacancies available on the oxide surface. Although the resulting response is relatively high, the challenge of lowering the working temperature of MoO_3 does not seem to be solved by this

 https://doi.org/10.1007/s40820-021-00724-1

strategy because the MoO_3 only participates in the sensing mechanism. However, Cd-doped MoO_3 synthesized by Bai et al. showed superior performance in detecting H_2S at a relatively low temperature of 140 °C [126]. This proves that there is an excellent opportunity for further exploration of this strategy. In addition, elemental doping can also be realized with nonmetal doping such as nitrogen, sulfur, selenium, and carbon [128–132]. Nonmetal doping has been reported to alter the electronic structure, reduce the bandgap, increase the amount of oxygen vacancy, increase the gas adsorption capacity, and induce bipolar electrical transport [128, 133]. Although nonmetal doping on MoO_3 has been relatively widely reported, its exploitation as a gas sensor is still rarely found. This is another challenge in the field of gas sensors, and exploration in the development of nonmetal doping MoO_3 is still very wide open.

2.4 Heterostructures Coupling

Another strategy to modulate the performance of MoO_3-based gas sensors is interface modification or heterostructure formation. The modification involves adding other materials, such as other metal oxides, carbon nanomaterials, and polymers. This composite strategy leverages the synergy of two different material properties to achieve superior performance [134, 135]. Response, selectivity, and sensitivity improvement are achieved using this strategy [136–138]. There is a need to consider the ratio of the two materials and the distribution of interface in this strategy because it relates to the conduction path in the surface reaction. Adding p-type semiconductor to n-type MoO_3 may increase the MoO_3 resistance due to the depletion region that reduces the MoO_3 charge conduction channel. The depletion region is created when the p-type semiconductor with a higher work function making contact with MoO_3. As illustrated in Fig. 7a, the electrons in the MoO_3 conduction band flow to the p-type conduction band and recombine with holes that flow in the opposite direction. This electron–hole recombination occurs until the Fermi level alignment meets the equilibrium state as shown in Fig. 7b. The depletion region is the region at the interface of the two materials where the major charge carriers of both materials are depleted. This region is believed to be sensitive to the presence of gases. However, the gas sensor performance only can be maximized when the surface reaction is dominated by the depletion region and the MoO_3 itself. When the number of p-type material is higher or covers the surface of MoO_3 like in the core–shell case, the conduction path may be fully taken by the p-type materials, and the MoO_3 does not contribute to the sensing mechanism leading to a lower response. This is why the composition ratio of p-type: n-type is an important key for achieving the best sensing performances. Li et al. found that dispersing 50 mg of MoO_3 nanobelts in ethanol containing 50 mM of $Co(NO_3)_2.6H_2O$ under ultrasonication resulted in $CoMoO_4$ decorated MoO_3 after calcining the product at 500 °C [138]. In this case, $CoMoO_4$ acts as a p-type metal oxide that has a narrower bandgap compare to MoO_3. Moreover, from gas sensor measurement, one can easily find that the five-fold increase in TMA sensing response of $CoMoO_4/MoO_3$ composite at 220 °C is contributed by the p–n junction at $CoMoO_4/MoO_3$. The MoO_3 itself shows its highest response to 10 ppm of TMA at 280 °C.

In another report, Xu et al. [80] examined the p-type of $NiCo_2O_4$ nanosheet coated α-MoO_3 nanorods. The nanorods themselves were produced using the hydrothermal method with Mo powder as a precursor, while the composite of

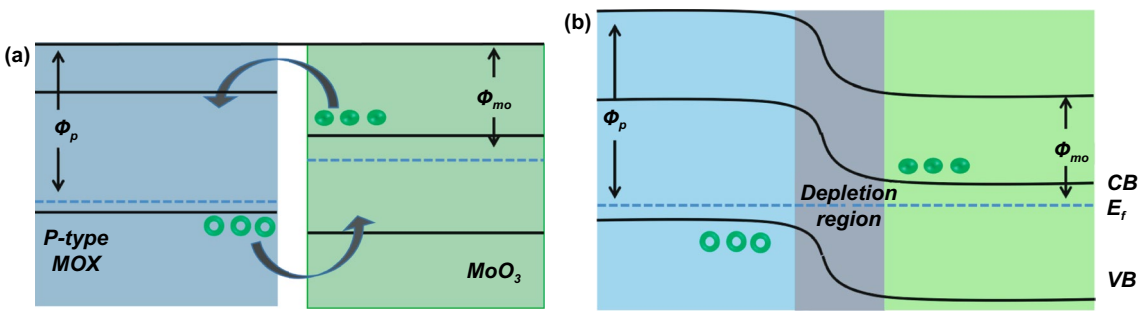

Fig. 7 Illustration of band diagram of p-type metal oxide and n-type MoO_3 **a** before and **b** after making contact. The depletion region is created at the interface as a result of electron–hole recombination during Fermi level alignment

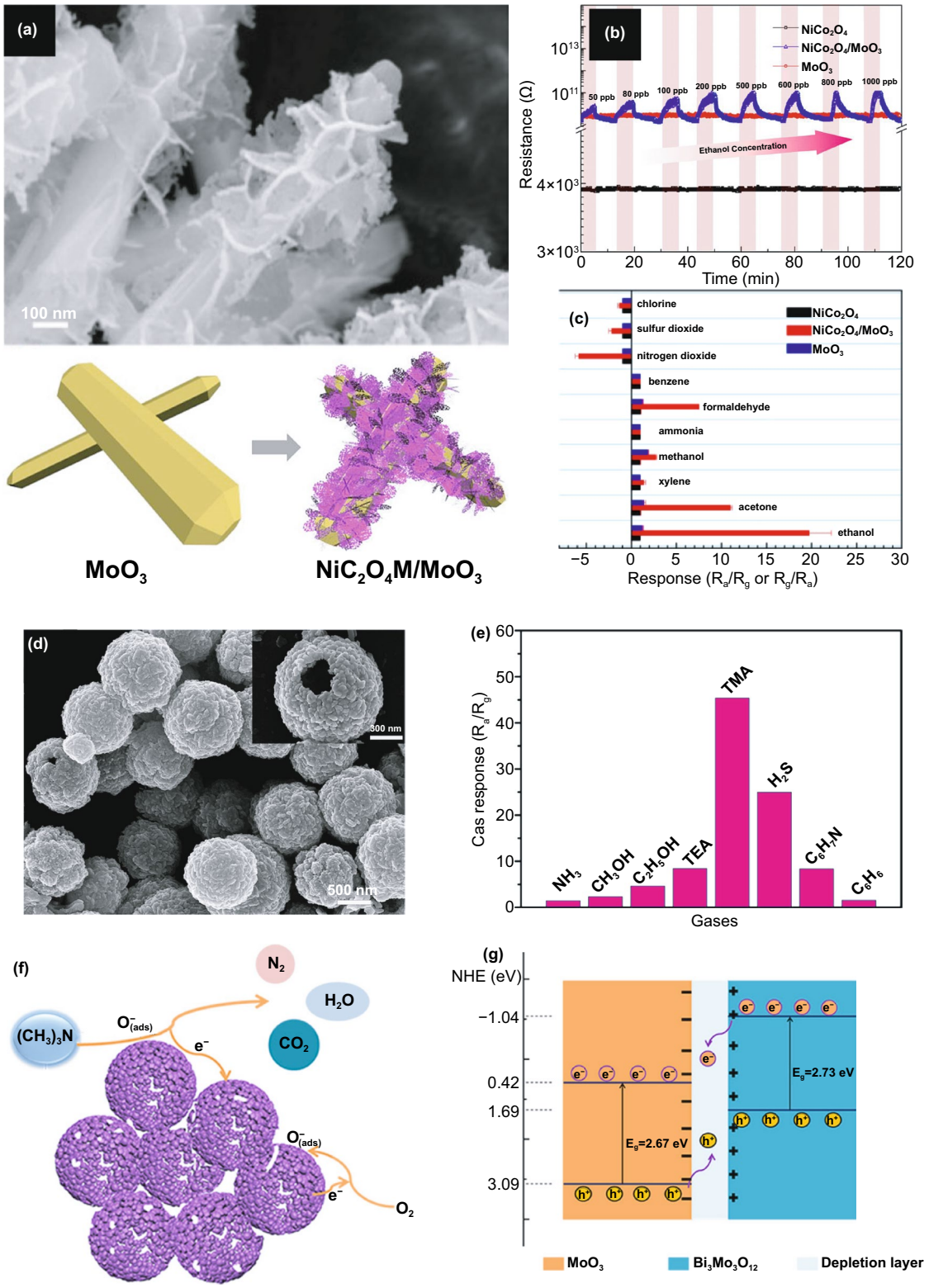

Fig. 8 **a** p–n heterostructure was constructed by $NiCo_2O_4$/α-MoO_3 nanorods with (**b, c**) sensing response and selectivity to 1 ppm of ethanol at 350 °C. Reprinted with permission from Ref. [80]. Copyright 2019 Elsevier 2020. **d** Hollow heterostructures consisted of MoO_3/$Bi_2Mo_3O_{12}$ exhibited selective sensing toward TMA **e**. The proposed sensing mechanism (**f, g**) showed electron–hole transfer processes between MoO_3 and $Bi_2Mo_3O_{12}$ upon the contact. Reproduced from Ref. [140] with permission. Copyright 2019 American Chemical Society

https://doi.org/10.1007/s40820-021-00724-1

$NiCo_2O_4$/α-MoO_3 was prepared using a chemical deposition approach. In their typical process, nickel and cobalt nitrates were dispersed in the aqueous solution containing α-MoO_3 nanobelts powder. The mixture was then heated at 95 °C for 2 h. The composite was obtained after calcining the product at 350 °C for 2 h. These procedures produce nanorods structure with width and length of 200 nm and 20 µm, respectively. Furthermore, the rods were also covered by the $NiCo_2O_4$ nanosheets. In its application as an ethanol sensor, the p–n junction was created at the interface of $NiCo_2O_4$/α-MoO_3. In general, Fermi alignment occurred along with the electron transfer from the n-type α-MoO_3 to p-type $NiCo_2O_4$. Since the work function of $NiCo_2O_4$ is lower than that of α-MoO_3, electron transfer occurred from $NiCo_2O_4$ to α-MoO_3, leading to a thicker hole accumulation layer on the $NiCo_2O_4$ side. The increase in resistance in the presence of ethanol indicates that the composite follows the $NiCo_2O_4$ characteristic. Under a reducing gas atmosphere, the released electrons from oxygen ion and ethanol reaction resulting in the thinner accumulation layer, leading to increase the composite resistance. This phenomenon is responsible for the high response of composites of 20–1 ppm of ethanol at 350 °C. Furthermore, the acid–base combination in the composites was claimed to have a high selectivity to ethanol.

Aside from p–n junction, n–n junction also can be created by contacting MoO_3 with another n-type metal oxide. For example, the formation of the n–n junction was realized by decorating MoO_3 nanobelts with Fe_2O_3 nanoparticles [139]. The decoration was completed using hydrothermal in the presence of $FeCl_3{\cdot}6H_2O$ and MoO_3 nanobelts. The 40 nm of Fe_2O_3 nanoparticles on the nanobelts create the n–n junction at its interface. As reported, different work functions between the two materials cause a depletion layer associated with barrier potential. The potential does not only produce the excellent response of 22.48 at 233.5 °C to 100 ppm of xylene but also improves the selectivity to xylene compared to the other VOC gases. Zhang et al. [140] prepared the MoO_3/$Bi_2Mo_3O_{12}$ hollow sphere composite via hydrothermal method. Based on the XPS spectra, the conduction band of MoO_3 is located lower than $Bi_2Mo_3O_{12}$; hence the electrons are transferred from $Bi_2Mo_3O_{12}$ to MoO_3. The electron transfer generates the depletion layer at the interface of MoO_3/$Bi_2Mo_3O_{12}$ and its thickness is sensitive to the change of atmosphere. The creation of depletion layer created and the number of oxygen ions trapped at the interface modulate the composite response to 50 ppm of TMA at 170 °C, 2.5 and 5.5 times higher than those of MoO_3 and $Bi_2Mo_3O_{12}$, respectively.

Heterostructure coupling can also be formed by combining MoO_3 with carbon nanomaterials, such as reduced graphene oxide (rGO). The rGO is categorized as 2D materials with remarkable properties and high surface area. Incorporating rGO to α-MoO_3 provides a conduction channel that increases surface reaction rate and reduces the operating temperature. Bai et al. [141] successfully incorporated MoO_3 nanorod onto the rGO surface with a very good distribution for optimal contact with rGO to be achieved. Sensing examination to 40 ppm H_2S shows that without rGO, α-MoO_3 works well at 170 °C with a response of 23.4. With 5 wt% of rGO, the composite works best 110 °C with a response of 59.7. Moreover, the observed response time and recovery time were 9 and 17 s, respectively. With optimal contact between the oxide and rGO, the rGO facilitates gas diffusion channels, mass transport, improve charge separation, and conduction channels between H_2S and α-MoO_3. By increasing α-MoO_3 resistance after rGO incorporation, rGO increases the characteristics of the n-type MoO_3 [141, 142]. The incorporation of α-MoO_3 nanoparticles on the surface of rGO for the H_2S sensor has also been reported [143]. The increasing specific surface area from 770 to 894 $m^2\ g^{-1}$ was achieved after 3 wt% of incorporating the nanoparticles. The enhancement of surface area causes the high response of 4120–100 ppm of H_2S at 160 °C. Although the operating temperature of α-MoO_3 nanoparticles-rGO is higher than the nanorod one, they show a better response. Figure 8 represents the work on heterostructures sensor based on α-MoO_3.

As stated earlier, the heterostructure coupling can be realized by combining MoO_3 with other metal oxide or carbon nanomaterials. Up to now, one can conclude that with proper ratio, high response and relatively low operating temperature can be achieved by p–n or n–n heterojunction. This strategy can also improve the selectivity of the composite. The higher resistance of the composite due to depletion layer formation is more suitable for detecting reducing gas such as TMA and H_2S. The higher resistance provides a wider detection range and a lower the limit of detection. Furthermore, the high conductivity of carbon nanomaterials at low temperatures is also a benefit for MoO_3. The highly p-doped carbon nanomaterials also contribute to sensing materials by generating Schottky contact with MoO_3, therefore, the high response at 100 °C can be achieved. Furthermore, it is expected that

hydrophobic of carbon nanomaterials can effectively help MoO_3 prevent the negative effect of humidity. As reported, carbon nanomaterials such as carbon nanotubes (CNT) and graphene show negligible humidity interfering effect up to 80% at low temperature [144]. However, the study of the effect of carbon nanomaterials on humidity interference in MoO_3-based gas sensors cannot be found anywhere. Therefore, the further investigation on this problem needs to be carried out in the future.

In summary, morphology design is most effective in increasing response. This strategy is strongly related to the number of active sites that depend on the morphology and specific surface area. The metal catalyst, such as noble metal and elemental doping, reduces the optimal temperature with the increased response. Moreover, the heterostructure strategy is also essential in achieving gas sensors with a high sensitivity, low operating temperature, and low response and recovery times. The parameters, such as the ratio of the second phase and MoO_3 need to be considered carefully to obtain the best performance. Table 1 summarizes the comparison of all strategies in gas detection.

3 Molybdenum Disulfide (MoS_2) Gas Sensing Materials

Molybdenum sulfide (MoS_2) is naturally available as a bulk molybdenite crystal with a 2H phase as a thermodynamically stable form. It exhibits an indirect band gap property of approximately 1.2 eV [145]. According to Fig. 9, the bulk possesses an interlayer space of 0.65 nm allows further delamination. It can be transformed into MoS_2 single-layer structures with a large intrinsic bandgap of 1.8 eV by mechanical exfoliation [146]. MoS_2, in the bulk form, has different crystal phases depending on the coordination bonding and stacking orders of [MoS_6] polyhedral. In general, MoS_2 crystallizes in three phases, including hexagonal (2H), octahedral (1 T), and rhombohedral (3R) with identical vertically stacking layers [147, 148]. There are strong in-plane covalent bonds of two sulfur atoms-sandwiched molybdenum atoms bounded by weak van der Waals forces [149]. Although they have similarities in their structures, only hexagonal 2H-MoS_2 with trigonal prismatic coordination behaves like a metal. 1 T-octahedral coordination (1T-MoS_2) and rhombohedral structure 3R-MoS_2 with trigonal prismatic coordination exhibit metals or semimetals characteristics [150]. There are five polymorphs in the single crystal or monolayer structure of MoS_2, including 1H, 1 T, 1 T′, 1 T″ and 1 T‴ [151]. Trigonal prismatic and octahedral coordination of bulk crystals are inherited by 1H-MoS_2 and 1 T-MoS_2, respectively. However, in monolayer phases, some point group symmetry changes lead to different inversion symmetries, such as D_{6h} to D_{3h} in the 1H-MoS_2 case. 1 T′, 1 T″, and 1 T‴ phases form due to the distorted structures of [MoS_6] octahedra [152, 153].

The significant variation of crystal structures (bulk and monolayer) and phases (stable and metastable) that MoS_2 possess bequeaths the unique features in their properties, such as tunable optical band gap (1.2–1.8 eV) and electronic structures [155]. Mechanical properties of MoS_2 are previously investigated. Bertolazzi et al. [156] have measured some mechanical characteristics of ultrathin MoS_2, which consists of a few layers. The MoS_2 monolayer exhibited in-plane stiffness of 180 ± 60 N m^{-1}, corresponding to an effective Young's modulus of 270 ± 100 GPa higher than its bulk MoS_2 counterpart (240 GPa) and benchmark carbon steel (210 GPa). Furthermore, the 2D monolayers have high stretchability and flexibility upon applying mechanical force without losing their inherited properties [157]. The monolayer MoS_2 has a breaking strength of 22 ± 4 GPa, which is about 11% of its Young's modulus [156]. According to the literature, Bulk MoS_2 shows electron mobility of 0.5–3 cm^2 V^{-1} s^{-1} [158]. The mobility can be increased to 12.1 cm^2 V^{-1} s^{-1} by making the monolayer MoS_2 into polycrystalline nature [159]. The highest electron mobility (200 cm^2 V^{-1} s^{-1}) was achieved in a single-layer MoS_2 transistor [154]. The electrical conductance of monolayer MoS_2 was 1.3×10^{-5} Ω cm^{-1} at room temperatures [160], which can be further increased through substitutional atomic doping, such as Nb and Re [161]. Additionally, 1 T-MoS_2 has seven times higher conductivity than 2H phase and smaller contact resistance for FETs (200–300 Ω μm at zero gate bias for 1 T-MoS_2 and 0.7–10 kΩ μm for 2H-MoS_2) [162, 163]. Both bulk and monolayer MoS_2 also exhibit excellent thermal conductivity. The experimental works showed that the out-of-plane thermal conductivity of bulk MoS_2 at 300 K falls within 1–52 W m^{-1} K^{-1} range and depends on the layer thickness of MoS_2 [164–167].

The last parameter that affects the gas sensing properties of MoS_2 is chemical. In this review, the chemical property is limited to surface chemistry properties since the gas sensing reaction and charge transfer process occurs mainly at

 https://doi.org/10.1007/s40820-021-00724-1

Table 1 Comparison of modification of MoO_3 technique in various gas detection

Improvement strategies	Sensing materials	Target gas	Conc. (ppm)	T (°C)	Response (R_a/R_g) or (R_{air}-R_{gas})/R_{air})	Response/recovery times (s)	Refs.
Morphology design	α-MoO_3 nanowires	H_2	15,000	RT	0.85%	3/2.7	[48]
	α-MoO_3 nanorods	Ethanol	400	350	35	N/A	[68]
	α-MoO_3 nanobelts	Xylene	100	206	3	7/87	[69]
	α-MoO_3 nanobelts	Ethanol	800	300	174	~40/~5	[70]
	α-MoO_3 nanosheets	Alcohol	100	300	33.1	21/10	[74]
	α-MoO_3 nanoflakes	Alcohol	100	300	28.1	23/13	[74]
	α-MoO_3 sheets	NO_2	10	250	56%	N/A	[75]
	α-MoO_3 sheets	H_2S	10	250	18%	N/A	[75]
	Flower-like α-MoO_3	TEA	10	170	931.2	25/–	[87]
	α-MoO_3 nanobelts	TEA	10	170	114.9	29/–	[87]
	α-MoO_3 nanoparticles	TEA	10	170	27.6	28/–	[87]
	α-MoO_3 nanobelts	Ethanol	200	300	21	69/174	[89]
	α-MoO_3 nanofibers	Ethanol	200	275	53	45/138	[89]
	α-MoO_3 nanorods	Ethanol	100	250	8.9	20/15	[91]
	Sponges-like α-MoO_3	Ethanol	100	250	19.8	15/15	[91]
	α-MoO_3 microboxes	Ethanol	100	260	78	15/5	[90]
	Sphere-like nanoflowers α-MoO_3	Ethanol	300	300	30.9	N/A	[85]
	Rose-like nanoflowers α-MoO_3	Ethanol	300	300	37.1	N/A	[85]
	Plate flowers α-MoO_3	Ethanol	300	300	27.3	N/A	[85]
	Nanosheet-assembled hierarchical MoO_3	Ethanol	400	300	32	13/9.6	[92]
	Nanofiber-assembled hierarchical MoO_3	Ethanol	400	300	24	3.2/2.4	[92]
Surface functionalization with noble metals	Au decorated α-MoO_3 hollow sphere	Toluene	100	250	17.5	1.6/-	[96]
	Au decorated α-MoO_3 hollow sphere	Xylene	100	250	22.1	2/-	[96]
	Au decorated MoO_3 nanosheet	Ethanol	200	280	169	14/5	[45]
	Au decorated MoO_3 nanobelts	1-butylamine	100	240	~300	23/388	[106]
	Ag decorated α-MoO_3 nanorods	TEA	100	200	400.8	3/107	[99]
	Pd-loaded MoO_3 flower-like nanobelts	NO_2	100	200	95.3	74/297	[101]
	Pt loaded α-MoO_3 nanobelts	Formaldehyde	200	RT	39.3	21.4/16.6	[100]
Elemental doping	Fe-doped MoO_3 nanobelts	Xylene	100	206	6.1	20/75	[119]
	Fe-doped MoO_3 nanoarrays	Xylene	100	340	28.1	2/21–33	[120]
	Ni-doped MoO_3 pompons	Xylene	100	250	62.6	1/50	[116]
	Zr-doped α-MoO_3 nanobelts	Xylene	100	206	7.99	32/264	[123]
	Cr-doped MoO_3 nanorods	TEA	100	200	150.25	7/80	[124]
	Ce-doped α-MoO_3 nanobelts	TMA	50	240	17.4	10/20	[125]
	W-doped α-MoO_3 nanobelts	TMA	50	280	13.8	6/11	[118]
	Cd-doped α-MoO_3 nanobelts	H_2S	100	140	378.5	23/45	[126]
	Zn-doped α-MoO_3 microflower	CO	50	240	31.23	10/14	[122]
	Zn-doped α-MoO_3 nanobelts	Ethanol	1000	240	321	N/A	[127]
Heterostructure	$NiCo_2O_4$ nanosheet coated α-MoO_3 nanorods	Ethanol	1	350	20	N/A	[80]
	Fe_2O_3–MoO_3 nanobelts	Xylene	100	233.5	22.48	4/102	[139]
	MoO_3/$Bi_2Mo_3O_{12}$ hollow sphere	TMA	50	170	25.8	7.1/–	[140]
	rGO–MoO_3 nanorod	H_2S	40	110	59.7	9/17	[141]
	rGO–α-MoO_3 nanoparticles	H_2S	100	160	4120	–/120	[143]

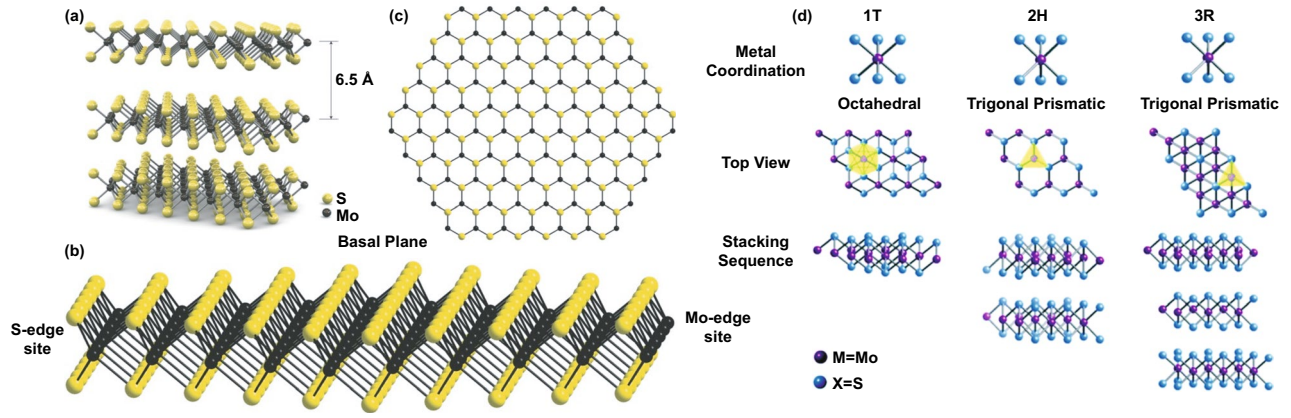

Fig. 9 **a** 3D form of bulk MoS_2 and **b, c** side and top views of 2D hexagonal layouts of single-layer MoS_2 (H-MoS_2). Reprinted with permission from Ref. [154]. Copyright 2011, Nature Publishing group. **d** Metal coordination and stacking sequences of TMD structural unit cells. Metal coordination can be either octahedral or trigonal prismatic. The octahedral coordination allows stacking sequences, which yield a tetragonal symmetry (1 T). Dissimilar stacking sequences of trigonal prismatic single layers give rise to different symmetries, including hexagonal symmetry (2H) and rhombohedral symmetry (3R). Reproduced with permission from Ref. [148]. Copyright 2017, The Royal Society of Chemistry

the material surface. Therefore, knowledge and understanding of the surface chemistry nature of MoS_2 are essential in advancing gas sensing properties. Surface-active sites differ in each MoS_2 phase. 2H-MoS_2 has highly surface-active for chemical adsorption edges at their layers [168, 169]. In 1 T-MoS_2, the surface-active is located in both edges and activated basal plane [170]. Therefore, 1 T-MoS_2 is more promising for chemical adsorption technology, such as catalysts and sensors [171, 172]. In a typical XRD pattern of MoS_2, three main peaks emerge. The inert basal plane has an orientation of (002) crystal plane, while (100) and (103) planes correspond to a step and edge plane, respectively.

We collected literature of MoS_2-based sensors available from the WoS database shown in Fig. 10. The first work on the MoS_2-based gas sensor was published in 1996. Similarly, MoS_2-based gas sensors were only available in thin-film structures. The sensing investigation of MoS_2 was limited to non-carbon-containing gases. A great interest in MoS_2-based sensors began not over a decade ago, where the significant improvement of their gas sensing performance was made by coupling with other materials. Moreover, this approach is still the most popular strategy for MoS_2 because of its interesting electronic structures that can support the performance of most oxide-based materials. Designing various morphological nanostructured MoS_2 is more feasible by wet chemical synthesis, although they possess layered structures. Advanced knowledge of phase diversity in MoS_2 structure expands the new strategy on how 1 T-2H phases engineering affects the gas sensing properties. Different from that of MoO_3, the MoS_2 is more sensitive to non-volatile organic compound (VOCs) gas due to the non-catalytic properties of MoS_2. However, using noble metals-functionalized surface strategy, it is also possible to detect VOCs highly. It should be noted that the majority of MoS_2-based sensors can be operated at room temperature.

3.1 Insight into Gas Sensing Mechanism of MoS_2

The gas detection mechanism by MoS_2 is still debatable. Some researchers believe that the gas sensor mechanism of MoS_2 is similar to oxide-based materials where the oxygen reduction and oxidation process during gas detection is involved. In contrast, others believe that the gas sensor mechanism of MoS_2 is a direct charge transfer from or to MoS_2, which directly affects its conductivity [173, 174]. However, the recent experimental and theoretical evidence have shown straightforward proof that the gas sensor mechanism of MoS_2 is a charge transfer process. Yue et al. [175] have reported the theoretical study of the molecular adsorption process of MoS_2. Various gases, including the H_2, O_2, NH_3, NO, NO_2, H_2O, and CO gases, have been investigated to be adsorbed on the MoS_2 surface. Figure 11a shows the charge density difference of all gases interacting with the MoS_2 calculated by Bader charge analysis. It could be seen that the charge transfer process occurred from or to the MoS_2

 https://doi.org/10.1007/s40820-021-00724-1

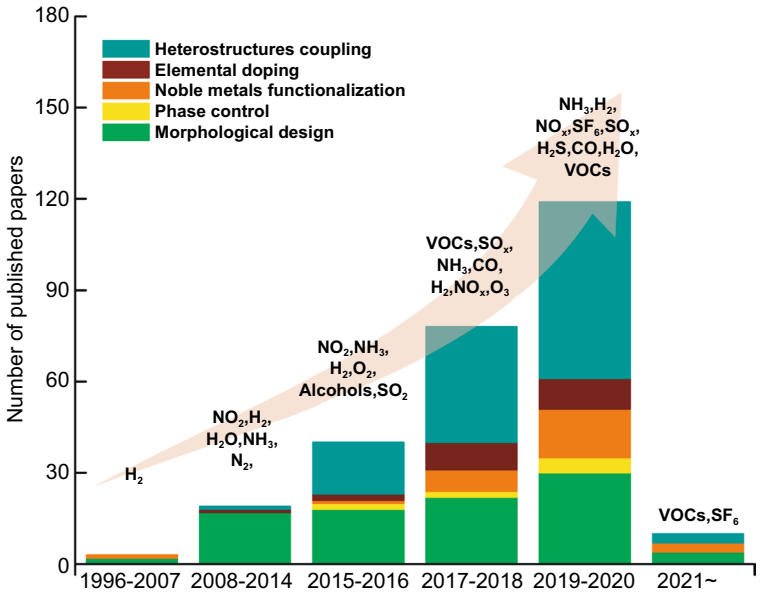

Fig. 10 Number of publications reporting advanced strategies to enhance gas sensing properties of MoS_2 toward various gas detection. Data are obtained from Web of Science (WoS) as of April 2, 2021, with the keyword "MoS_2 gas sensing." Both experimental and computational reported are included. Review and perspective articles are excluded

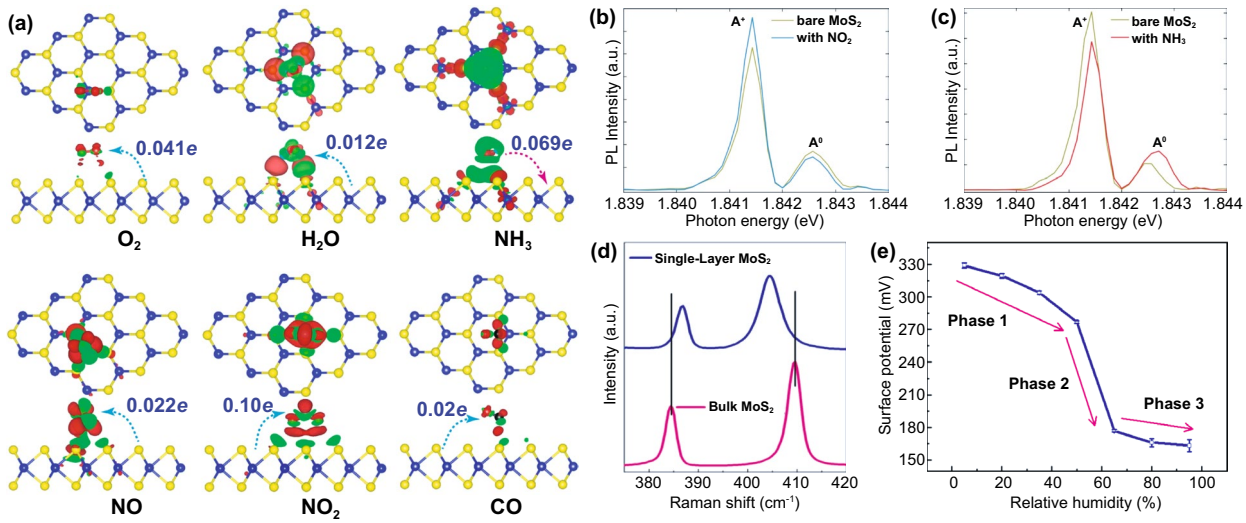

Fig. 11 **a** Charge density difference plots for O_2, H_2O, NH_3, NO, NO_2, and CO interacting with monolayer MoS_2. The red (green) distribution corresponds to charge accumulation (depletion). The isosurface is taken as 5×10^{-4} e Å^{-3}. The direction and value of charge transfer are also denoted. Reprinted from Ref. [175]. Copyright 2013, Springer Inc. In situ PL spectra recorded from the MoS_2 with **b** NO_2 and **c** NH_3 molecules. Reprinted from Ref. [174]. Copyright 2015, Springer Nature. **d** Raman spectrum of bilayer MoS_2 sheet before and after exposure to 1000 ppm NH_3. Reproduced from Ref. [176] with permission. Copyright 2013, American Chemical Society. **e** Statistical results of the Surface Potential of monolayer MoS_2 under different relative humidity. Reproduced from Ref. [177] with permission. Copyright 2017, IOP Publishing, Ltd

surface. Different gases result in different charge transfer behaviors due to the chemical structure of the gases molecules. The H_2, O_2, NO, NO_2, H_2O, and CO gases received the electron from the MoS_2 surface, which indicates the electron acceptor behavior of these gases. On the other hand, in NH_3 gas, the NH_3 donates the electrons into the MoS_2 surface. This phenomenon will affect the conductivity of MoS_2, which will be detected as the change of the electrical

signal during the gas detection. For example, in the case of NO_2, which acts as electron acceptor gas, the conductivity of n-type MoS_2 will decrease due to the reduction of its charge carrier (electron) number from the n-type MoS_2 surface. On the other hand, in NH_3, because it acts as an electron donor gas, the conductivity of n-type MoS_2 will increase due to the additional electron on the surface [176].

The experimental evidence about the charge transfer process during the gas sensor measurement has also been investigated through several methods. Cho et al. [174] have conducted the in situ photoluminescence (PL) analysis of MoS_2 in the presence of NO_2 and NH_3 to understand the interaction between MoS_2 and thus gases. Figure 11b, c shows the in situ photoluminescence measurement results of MoS_2 in the presence of NO_2 and NH_3 gases. The A exciton signal from MoS_2 can be expanded into two species: a trion of $A^{-/+}$ (two electrons to a hole, resulting in a negatively charged exciton, or an electron to two holes, resulting in a positively charged exciton) and a neutral exciton of A^0. The PL analysis after and before gases exposure is shown in Fig. 11b, c. The A^+ and A^0 trion appeared in the PL spectra. After NO_2 gas exposure, the A^+ and A^0 peak intensity change. The A^+ trion increase after NO_2 gas exposure while the A^0 peak intensity decrease. This phenomenon occurred because of the electron deficiency in the MoS_2 after NO_2 adsorption. Another report from Kelement et al. [180], who studied the Fermi energy of MoS_2 under N_2 and O_2 atmosphere, has also confirmed the charge transfer between MoS_2 and O_2 gases through PL measurement. A relative spectral weight shifts from A^- to A^0 during the oxygen exposure, and the PL intensity increases. This behavior occurred due to the depletion of electrons which in this case is of chemical origin. Because O_2 is more electronegative than N_2, the ion sorption of O_2 as O^{2-} results in the depletion of free electrons due to charge transfer to O_2 molecules. The Raman analysis has been confirmed able to detect the charge transfer process between MoS_2 and the gases. Figure 11d shows the Raman spectra of the as-prepared MoS_2 and as-prepared MoS_2 in the presence of NH_3 investigated by Late et al. [178]. The Raman A_{1g} and E_{2g} peaks' shifting was observed, which attributed to the charge transfer interaction with an electron donor molecule [181, 182]. Feng et al. [183] have conducted the potential surface analysis under different humid air environments by using Kelvin probe force microscopy. The result plotted in Fig. 11e has shown that the surface potential of the MoS_2 decreases with the increase in humidity value. The decrease in the surface potential is due to the injection of carriers from the adsorbed water led to the Fermi level shift of MoS_2. From all this analysis, it is confirmed that the gas detection of MoS_2 is a charge transfer process.

3.2 Morphological Design

With a lamellar structure, it is quite demanding to design various morphological structures of MoS_2. Most of the synthesized MoS_2 exhibited either monolayer, few layers, or multilayer structures. The sensing materials morphology is usually designed to optimize the gas adsorption/desorption processes, such as with more active sites, large surface area, porosity, or surface defect, leading to improved gas sensing properties. With an appropriate approach and synthesis method, the shape of MoS_2 could be altered into different dimensions. A good example is the use of surfactants in hydrothermally synthesized MoS_2. A controlled morphology, including spherical, bulk-like, and flower-like MoS_2, was produced by varying surfactants, such as PEG, SDS, PVP, AOT, or CTAB [178–180]. Other experiments involving surfactant-assisted hydrothermal process successfully fabricated some shape variants of MoS_2, such as 1D nanoribbons [181], 2D nanoplatelets [182], 3D hollow nanoparticles [183], and 3D hierarchical microspheres [184, 185]. The remaining surfactants may become an impurity in the synthesized products, amplifying the functional performance. However, this leads to alternative surfactant-free synthesis for morphology-controlled MoS_2, which might be of great interest to many researchers. Sen et al. [186] and Ye et al. [187] fabricated 2D nanowalls and bilayer nanosheets without involving any surfactant or directing agent. In many cases, with or without surfactants, morphological features and shape tunability of MoS_2 can be successfully performed.

This section discusses how different morphologies influence the gas sensing properties of MoS_2, including those layered structures and other morphologies. As a native structure, monolayer MoS_2 is among the primary gas sensing material due to its high surface-to-mass ratio. Other studies show that 2D monolayer structures sense chemical vapors, NO_2, H_2, and CO gases [32, 176, 188–192]. Figure 12a, b shows some selected works on gas sensing performances of 2D mono-/single-layer MoS_2 in NO_2, trimethylamine, and ammonia detection. Notably, edge sites of 2D MoS_2 monolayer are more reactive than the basal planes. For

 https://doi.org/10.1007/s40820-021-00724-1

this reason, constructing MoS_2 with a dominant edge site improves the sensitivity to several folds. The first principle study suggested that hydrogen molecules are favorably adsorbed on the top of Mo atoms at the edge site rather than Mo atoms at basal planes that strongly supports the experimental results [189]. The ability to respond to a wide range of low concentration gases, mono-/single-layer MoS_2 makes it an ideal sensing material. Moreover, such a structure offers greater flexibility with retained properties upon mechanical bending, compressing, and stretching [44]. Whether 2D MoS_2 monolayer is an optimized structure to obtain high-performance sensing is still under debate. Sensing devices comprising thin-layered MoS_2 with different thicknesses were fabricated by micromechanical exfoliation mounted on the chip [176]. The thickness of single-layer MoS_2 is about 0.9 nm, as confirmed by AFM (Fig. 12d, e). The results showed that the five-layer MoS_2 sample has better sensitivity to NH_3 and NO_2. However, the enhanced sensing mechanism is still unclear because MoS_2 may exhibit different electronic structures and redox mechanisms when the layered structures are altered. This issue limits further understanding of the solid–gas interaction at the interface of single- and multilayer 2D MoS_2 and overcoming this issue requires special attention. DFT calculation can be a good approach attempting for the revelation of electronic structure dependency in a single- and multilayer 2D MoS_2.

Although 2D mono-/few layers MoS_2 have outstanding performances in sensitivity, selectivity, low-power consumption and stability, their complex synthesis process, and device fabrication are not favorable for scaling-up production to mass application. However, 3D hierarchical nanostructures assembling from the lower dimension of 2D nanocrystal provide a simpler and scalable synthesis [195]. Particularly, their shorter diffusion pathway, relatively higher surface area, and distinguished electronic properties compared to conventional 2D structures increase the interaction with adsorbed molecules, leading to higher responsivity. For instance, the 3D hierarchical MoS_2 nanospheres exhibited excellent sensing properties to CO gas at 230 °C, which surpassed the performance of 2D nanosheets, as shown in Fig. 12g. The CO sensing properties were not observed previously in any other 2D MoS_2 [188]. In similar cases, 3D hierarchical porous MoS_2 synthesized by a simple hydrothermal method had different gas selective properties, including NO_2 and H_2 [185]. It gives novel knowledge on tunable gas selectivity by precise morphological design. However, comprehensive works are needed to understand tunable selective properties on different crystal morphologies.

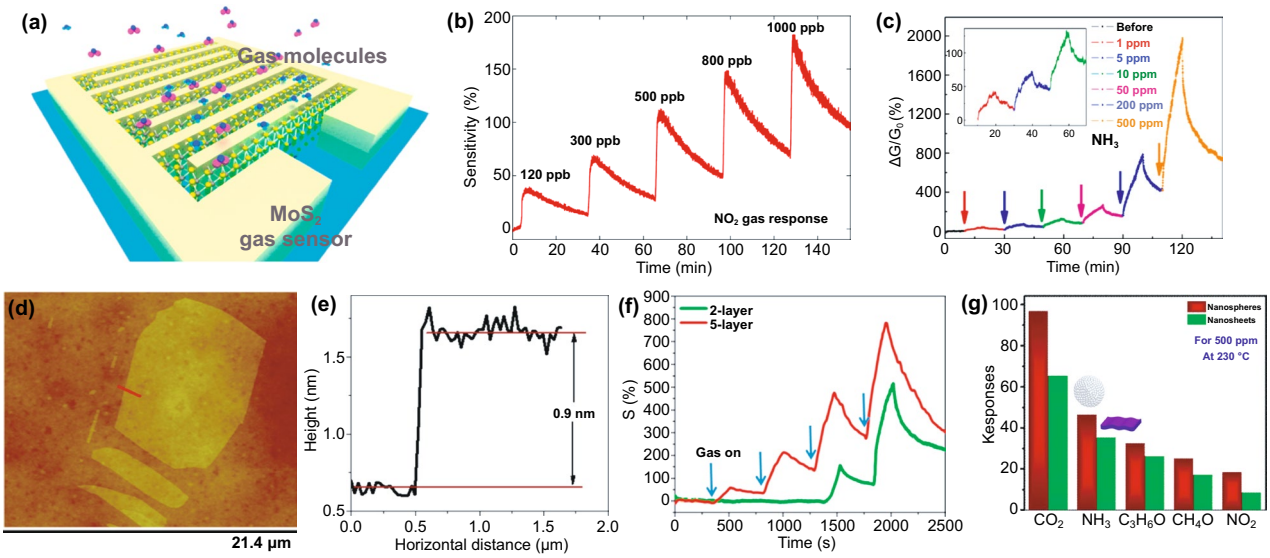

Fig. 12 **a** 3D schematic image of the MoS_2 gas sensor device under gas molecules. **b** The transient NO_2 gas response of the MoS_2 device from 120 to 1000 ppb at RT. Adapted from Ref. [193]. Copyright 2015, American Chemical Society. **c** Real-time conductance change in MoS_2 FETs with time after exposure to NH_3 under different concentrations, adapted with permission from Ref. [194]. Copyright 2014, American Chemical Society. **d** AFM image and **e** corresponding AFM height profile of single-layer MoS_2 sheet deposited on 300 nm SiO_2/Si substrate using the micromechanical cleavage method. **f** Comparative two- and five-layer MoS_2 cyclic sensing performances with NO_2 (for 100, 200, 500, 1000 ppm). Reprinted from Ref. [176]. Copyright 2013, American Chemical Society. **g** Selectivity of MoS_2 nanostructures for different gases, reproduced from Ref. [188]. Copyright 2018 Elsevier

The gas sensing performance of lower-dimensional MoS_2 (0D and 1D) is far less investigated, although 0D and 1D MoS_2 fabrications are feasible, and they are substantial components in several applications, including electrocatalysis and energy storage. 0D MoS_2 can be prepared by a top-down and bottom-up approach. In the top-down process, 2D MoS_2 undergoes thinning and bond-braking processes with the aid of ion intercalation, chemical/liquid exfoliation, or sonication. On the other hand, the hydrothermal reaction has been a convenient pathway in producing 0D MoS_2 by a bottom-up process. The synthesis involves Mo and S precursors in aqueous media. Generally, the size of produced 0D MoS_2 is in a range of 0.5–4.5 nm. Due to this quantum size confinement, 0D MoS_2 exhibits abundant active sites, large surface areas, and a large band gap (> 3.96 eV), raising unique gas sensing properties. Nevertheless, using 0D MoS_2 for gas sensing is challenging because it easily gets agglomerated, reducing its active surface areas. Thus, supporting materials are required to provide the anchor platform. The 1D MoS_2 (nanowires, nanotubes, nanoribbons, etc.) has also been successfully fabricated in a similar approach. MoS_2 nanotube, for example, was synthesized by chemical transport using MoS_2 powder as a precursor and iodine as a transport agent [196]. It had, however, size nonuniformity, defective structure, and low yield. The low-temperature hydrothermal method offers an alternative to synthesize 1D MoS_2 nanotube and nanorod with high size homogeneity and high yield. Benefiting from the enhanced surface-to-volume ratio and the faster charge transfer along the length direction, high-performance gas sensing can be enabled. It is, therefore, expected that both 0D and 1D MoS_2 would boost the detection of various gases due to the facts described above. Nevertheless, this hypothesis needs theoretical and experimental validation.

3.3 1T—2H Phase Control

The recent development of gas sensor devices still focuses on semiconductor-like 2H-MoS_2. However, the 2H-MoS_2 has limitations, primarily due to limited active sites and small adsorption energy. Several studies show that the active sites of 2H-MoS_2 are only located on the edge of the crystal structure, while the abundant basal plane is inert for chemical reactions [197–199]. In comparison, the 1 T/1 T' of MoS_2 is more active than 2H-MoS_2. Tang et al. [200] studied the adsorption performance of various molecules, including H, CH_3, CF_3, OCH_3, and NH_3. The results showed that the adsorption energy of 1 T and the molecular adsorption ability of 1 T MoS_2 were significantly higher than 2H-MoS_2. However, the 1 T-MoS_2 itself is electrically conductive to be applied as a sensor; hence electrical change during the molecular adsorption was hardly observed. The 1 T/1 T' phase is relatively unstable, and therefore, it only exists in the mixed phases of 1 T/2H-MoS_2. The HRTEM image (Fig. 13a) showed the observed grain boundary between orthorhombic and tetragonal structures, which indicates the successful formation of 1 T/2H-MoS_2 [201]. The electronic properties of 1 T/2H-MoS_2 are easily understood by Raman and XPS analysis, as shown in Fig. 13b, c [202]. The Raman spectra of 1 T/2H-MoS_2 consist of several vibration peaks. Three peaks located at 156, 228, and 330 cm^{-1} are attributed to the J_1, J_2, and J_3 vibration modes of the 1 T phase. The vibration peaks located at 283 and 403 cm^{-1} are attributed to the E_{1g} and A_{1g} modes. The formation of 1 T/2H-MoS_2 can be analyzed by XPS of Mo 3*d* core spectra, as shown in Fig. 13c. The Mo 3*d* core-level spectra of 1 T/2H-MoS_2 are deconvoluted into four different peaks. The lower binding energy peaks are attributed to the 1 T phase, while the higher binding energy peaks belong to 2H-MoS_2.

Several reports have demonstrated the formation of 1 T/2H-MoS_2 for various kinds of applications, such as hydrogen evolution reactions [201, 203, 204], hydrodesulfurization [205], and gas sensor applications [172]. Yang et al. [206] demonstrated the formation of the 1 T/2H-mix phase in the molybdenum tungsten sulfate (MWS_2) system for acetone gas detections. Hydrothermal reactions achieved the mixed 1 T/2H phases. With further annealing, the 1 T phase turned into a 2H phase. The enhanced acetone detection performance to several folds was achieved with only 10% of 1 T content in the MWS_2 system. Taufik et al. [172] have also successfully demonstrated the formation of 1 T/2H-MoS_2 structure via ethylene glycol (EG) intercalation for improved toluene gas detection performance. The EG intercalation process enhanced the ratio 1 T/2H phase from 1.7 to 4.0 and decreased the conductivity of 1 T/2H-MoS_2 due to EG low conductivity. The electron from toluene is transferred to the MoS_2 surface during the toluene adsorption, increasing the conductivity. Moreover, the gas sensor performances of EG-intercalated samples are much higher than the pristine ones. It was indicated that 1 T-MoS_2 is vital in improving the gas

 https://doi.org/10.1007/s40820-021-00724-1

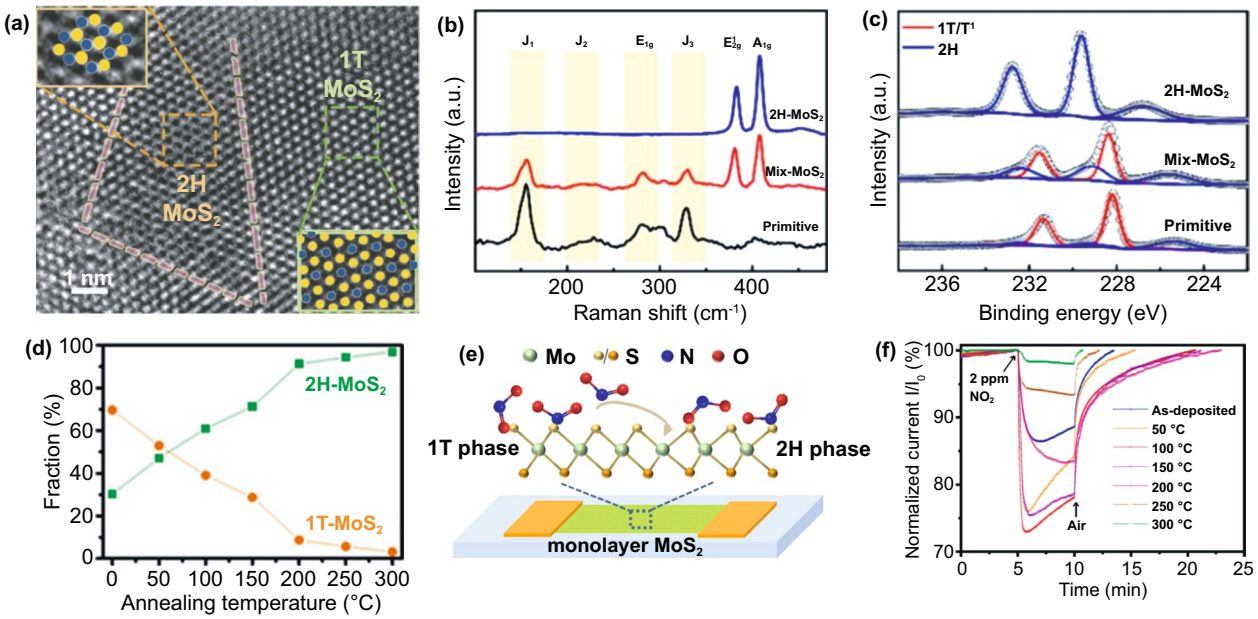

Fig. 13 **a** HRTEM images of 1 T/2H MoS_2. Reproduced with permission from Ref. [201]. Copyright 2018, Wiley-VCH. **b** Raman spectra and **c** XPS spectra for the primitive 1 T'-MoS_2 nanosheets. The mix-MoS_2 represents the exfoliated MoS_2 nanosheets obtained through butyl lithium intercalation. Reproduced from Ref. [202] with permission. Copyright 2017 The Royal Society of Chemistry. **d** Relative fractions of 1 T and 2H phases as a function of temperature. **e** Schematic illustration of NO_2 detection of 1 T/2H MoS_2. **f** Sensing responses of as-deposited and thermal-annealed ML-MoS_2 to 2 ppm NO_2 gas. Reproduced with permission from Ref. [207]. Copyright 2020 American Chemical Society

sensor performance of MoS_2. Zong et al. [207] carefully controlled the amount of 1 T and 2H concentration by the annealing process of hydrothermally prepared MoS_2. The higher the annealing temperatures, the smaller the amount of 1 T concentrations, as shown in Fig. 13d. The highest NO_2 detection performance (sensitivity up to 25% under 2 ppm NO_2, rapid detection time of 10 s and LoD of 25 ppb) was achieved by annealing MoS_2 at 100 °C, where the ratio of 1 T/2H is 2:3. The NO_2 gas sensor mechanism and performances of 1 T/2H-MoS_2 are shown in Fig. 13e, f. The preceding results show that the gas detection capability of 1 T/2H-MoS_2 could be boosted by controlling the heterophase, which brings new insights into transition-metal dichalcogenide gas sensors. A further investigation should be performed, especially with the utilization of in situ/*operando* spectroscopy, to essentially improve our current understanding of how each phase's stability and contribution to the overall gas sensing properties of MoS_2. Ideally, the papers report MoS_2 gas sensors should be accompanied by DFT simulation to reveal the principle gas sensing mechanism.

3.4 Surface Functionalization with Noble Metals

Numerous works on the noble metals-functionalized gas sensing materials have significantly enhanced responsivity, improved/tuning selectivity, and lowered working temperatures. As mentioned in the earlier discussion, pristine MoS_2 has shown a promising gas sensing performance. However, it is accompanied by several limitations, including poor selectivity due to high cross-sensitivity to many gases and limited sensitivity at room temperature. Surface functionalization by noble metals has been applied to metal oxides gas sensing and non-oxides, including the MoS_2. Noble metals, especially in nanoparticles (NPs) form, are utilized because they generally promote a more catalytic process via spill-over effect and electronic sensitization through charge carrier concentration and significantly alter internal electrical conductance or resistance of MoS_2 measured by the sensing system. The catalytic reactions always follow the preceding gas adsorption/desorption process, despite the nature of gas (reducing or oxidizing) and gas composition (organic or non-organic). The spill-over effect by noble metals loading on

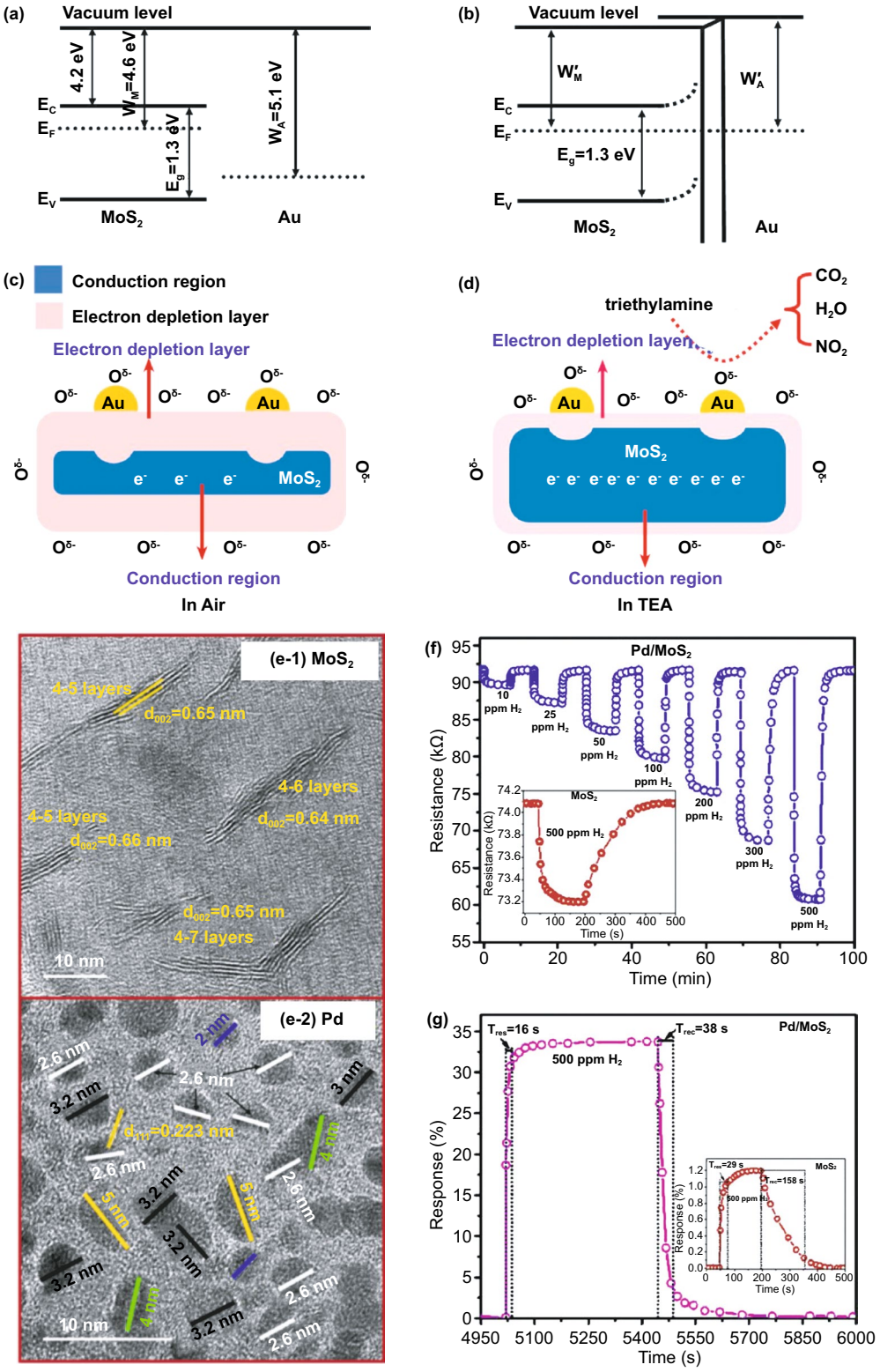

Fig. 14 **a** Concept map of the energy band configurations for MoS_2 and Au. **b** Energy band changing of Au@MoS_2 heterojunction. **c, d** Schematic of material before and after gas sensing response. Reprinted with permission from Ref. [208]. Copyright, 2020, Elsevier B.V. HRTEM images of (**e-1**) MoS_2 and (**e-2**) Pd nanoparticles. **f** A characteristic response curve (electrical resistance as a function of time) and **g** the sensor response curve of the Pd/MoS_2 hybrid and the pristine MoS_2 (inset) thin-film sensing devices toward H_2. The gas sensing measurement was conducted at room temperatures. Reprinted from Ref. [212] with permission. Copyright, 2020, Elsevier B.V

https://doi.org/10.1007/s40820-021-00724-1

the sensing material's surface helps lowering the potential energy dissociation of molecular oxygen (O_2) in the air, so that ionization process into monoatomic O is facilitated. It also facilitates the ionized O transport to the MoS_2 surface. The process cultivates the increase in the adsorbed oxygen ions on the materials for further reaction with tested analytes. The work function of noble metals is critical in regulating the mechanism, and herewith the modified gas sensing mechanism of MoS_2 under different noble metals loading is discussed. The work functions of MoS_2, Au, Pt, Pd, and Ag are 4.6, 5.1, 5.6, 5.4, and 4.8 eV, respectively. Due to the different work functions, in which the MoS_2 has a lower work function than many noble metals, upon the contact, the electron will flow from MoS_2 to noble metal through the depletion channel until the Fermi energy levels are equalized. Because of this process, the charge carrier concentration and mobility in depleted regions are improved and dissociated oxygen is more captured. More active interaction between ionized oxygens and the analytes is expected to improve gas sensing properties upon the analyte flow. The MoS_2 surface decoration by noble metals can be performed using several approaches, including heat treatment, DC sputtering, chemical reduction, or directly adding the chemical reagent containing noble metals as the precursors under a one-pot synthesis condition.

It is noticed that the different noble metals will determine the different gas selectivity of MoS_2 to some extent. For example, Au@MoS_2 nanostructures can directly be grown on ceramic tubes in one-pot hydrothermal treatment at 180 °C. Au nanoparticle decoration was deposited by DC sputtering with a predesignated sputter times [208]. The Au nanoparticles have a spherical shape with a diameter of 5 nm. Au@MoS_2 exhibited a remarkably higher response (5 times) and faster recovery speed to trimethylamine (TEA) gas at 280 °C than pristine MoS_2. As shown in Fig. 14a–d, the band depletion occurred during the contact between MoS_2 and Au due to the charge transfer process. The O_2 was adsorbed and then dissociated to O^- on the Au surface before redistributing it onto the MoS_2 surface. The thickening of the depletion layer and the increase in spilled O^- have increased the electrical resistance. During the TEA flow, the electrical decreased due to the active reaction of O^- with TEA and the removal of electrons in the depletion barrier. Au is believed to prefer adsorbing amine functional groups, as the Au–MoS_2 had a remarkable sensing response towards ammonia [209].

Pd-functionalized MoS_2 sensor acted differently from that of Au@MoS_2 because it had shown excellent hydrogen gas sensing properties, *e.g.,* in the case of Pd-MoS_2 nanosheets [210], Pd-MoS_2 nanostructures [211], and vertically aligned edge-oriented MoS_2 nanostructured thin film functionalized by Pd nanoparticles [212]. Figure 14e–g shows that the exfoliated MoS_2 has 4–7 layered structures while Pd nanoparticles are 2–5 nm in size. Furthermore, Pd-functionalized vertically aligned MoS_2 thin film has an average thickness of 19.5 nm. At RT, the sensor exhibited the highest response of 33.7% to 500 ppm of H_2 with a rapid sensing response and recovery times (16/38 s). The spontaneous dissociation of hydrogen molecules on the Pd metals is the firm reason behind the strong response of Pd@MoS_2, in which the formation of PdH_x affected the considerable resistance alteration. The distinguished selectivity behavior can also be found in the Ni-, Pt-, and Ag- loaded MoS_2 nanostructures gas sensing [213–216]. However, the underlying mechanism of how the gas dissociation process occurs on the surface of noble metals is still uncertain. The comprehensive computational studies, such as combining DFT calculation and molecular dynamic (MD) simulation, are essential in the future to provide a deeper insight into the gas sensing mechanism in noble metals-functionalized MoS_2.

3.5 Elemental Doping

Various atoms are suitable doping elements for improving the gas sensor performance of MoS_2. Sulfur or molybdenum substitution by foreign atoms is expected to improve the gas adsorption ability of MoS_2. As in many initial investigations, the introduction of doping into crystal structures of pristine MoS_2 [217] aims to increase charge carrier transfer via band structures alignment, form more effective gas adsorption sites, or create a trapping mechanism for suppressing the electron–hole recombination. Pristine MoS_2 is a natively n-type semiconductor originated from electron-donating sulfur vacancies, and the intrinsic n-type conductivity can be tuned to p-type conductivity with suitable substitutional atomic doping [218–220]. The resistivity behavior during the sensing mechanism will likely be similar to those of most metal oxides. Thus, discussion on the sensing mechanism has focused on the effect of dopings on gas sensing properties of MoS_2 proposed by recent investigations. For instance, Zn doping is the effective dopant to

induce p-type conductivity and tailoring effect on the MoS_2 ultrathin nanosheets gas sensing properties. In this case, the Zn atom replaced the Mo atom at the edge site, inducing the formation of Mo vacancies and acted as a new adsorption site for both O_2 and NO_2 gas due to the difference in electronegativity (Zn^{2+}: 1.70 and Mo^{4+}: 2.24). Therefore, it is easier for oxygen molecules to capture the electron from the Zn site, resulting in enhanced adsorption capacity and wider depleted regions. However, when the Zn^{2+} amount reached above 5% state, the adsorption capacity gets saturated, potentially decreasing the gas sensing performance (Fig. 15**).** From this understanding, the choice of atomic doping and its amount are critical to tailor the gas sensing properties.

Although there are limited reports of doped MoS_2, recent theoretical calculations studies show that the gas adsorption ability of MoS_2 can be enhanced by ion substitution with other atoms. For example, Linghu et al. [133] reported the theoretical investigation on the effect of S substitution of MoS_2 by various nonmetallic atoms (C, N, and O) on the CO, CO_2, NH_3, SO_2, NO, NO_2, and O_2 gases adsorption ability. The results show that the anions significantly improve the gases adsorption ability of both 2H-MoS_2 and 1 T'-MoS_2, as shown in Fig. 16a, b. The adsorption energy of anion-doped MoS_2 samples shows a massive improvement than pristine MoS_2. Compared to other doping elements, C-doping shows the best adsorption ability for all tested gases. For 1 T'-MoS_2, the N-doped MoS_2 and O-doped MoS_2 showed the best adsorption ability on CO_2 and O_2, respectively. Other reports also have confirmed that N-doping, O-doping, and C-doping MoS_2 improve the gas adsorption performance of MoS_2, directly affecting the gas sensor performance. Recent experimental evidence of the improvement of MoS_2 gas sensor by the presence of O atom was reported by Taufik et al. [222] O_2 plasma treatment was used to introduce O atom into the crystal structure of MoS_2 for enhancing the humidity sensor performance of MoS_2, as shown in Fig. 16c. The more extended O_2 plasma irradiation led to more oxygen amount in the crystal structure. O atom's presence significantly improved the humidity sensor performance of MoS_2 in the crystal structure. Although the direct evidence of the presence of N-doped MoS_2 and C-doped MoS_2 for gas sensor devices had not been reported, the N-doped MoS_2 and C-doped MoS_2 are widely used for hydrogen evolution

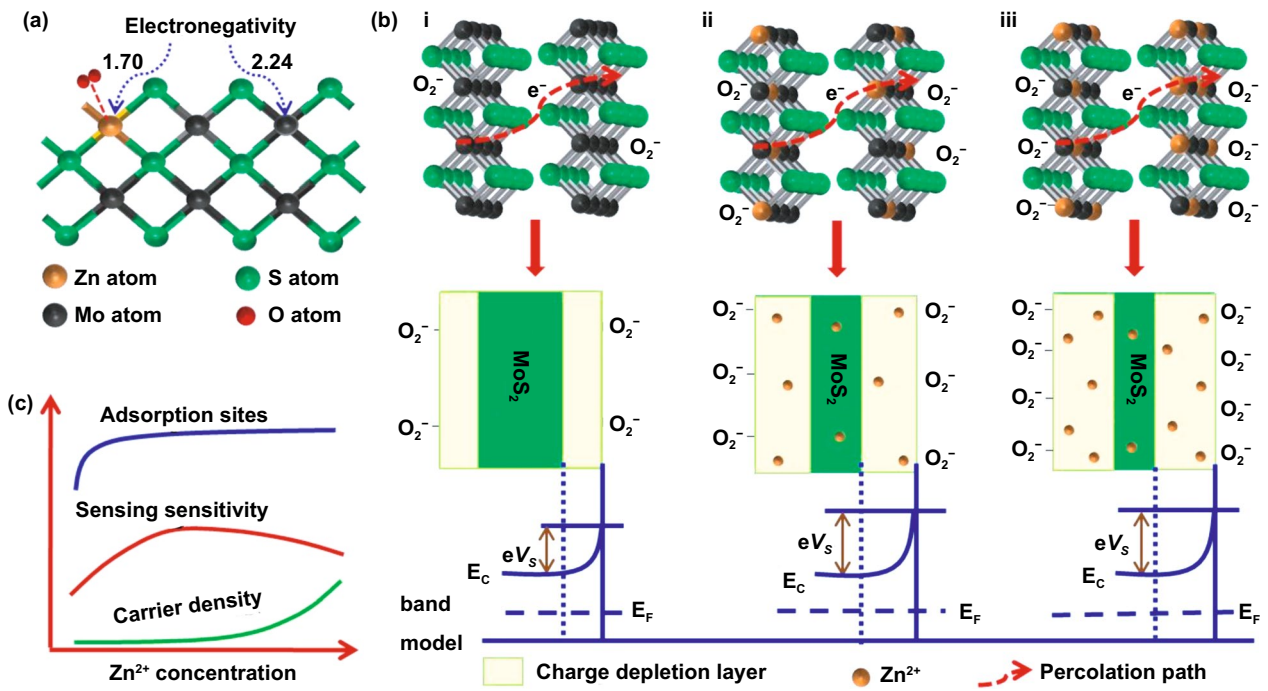

Fig. 15 **a** Surface adsorption illustration of Zn: MoS_2 UNs, **b** structural and band models showing the role of doping Zn^{2+}, i: pure MoS_2, ii: MoS_2 with intermediate Zn^{2+} concentration, iii: MoS_2 with high Zn^{2+} concentration, and **c** possible effects of Zn^{2+} concentration on absorption capacity, carrier density and sensing sensitivity. Reprinted from Ref. [221] with permission. Copyright 2018, Elsevier

https://doi.org/10.1007/s40820-021-00724-1

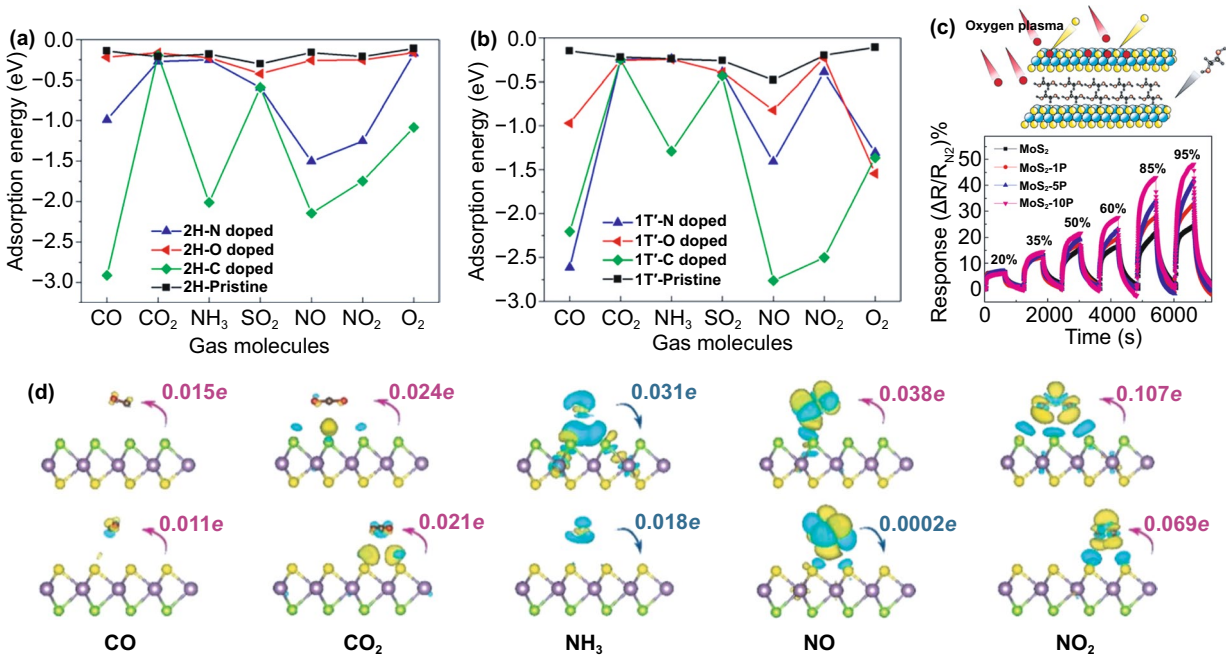

Fig. 16 Adsorption energy of gas molecules on the C-, N-, O-doped **a** 2H- and **b** 1 T-MoS_2 monolayers. Reprinted with permission from Ref. [133] Copyright 2020, American Chemical Society. **c** Sulfur substitution using O_2 plasma irradiation of MoS_2 and humidity sensing response values of MoS_2 irradiated by O_2 plasma. Reproduced with permission from Ref. [222]. Copyright 2020, American Chemical Society. **d** Charge density difference (CDD) for gas molecules adsorbed on the Se side (top panel) and S side (bottom panel). The yellow (cyan) region represents charge accumulation (depletion) and the isosurface. The orientation and the value of charge transfer of these molecules adsorbed on the Se and S surfaces are denoted. Adapted with permission from Ref. [229]. Copyright 2019 The Royal Society of Chemistry

reaction and photocatalyst [223–226]. According to Li et al. [225], the insertion of N atoms induced the defect on S sites. N atoms optimize the electron density beneficial for hydrogen evolution reactions. Guo et al. [227] reported that the edge of the MoS_2 structure can be engineered by the presence of N-doping and increase the hydrogen evolution reaction with a low overpotential of 114 mV to produce a current density of 10 mA cm^{-2} and high stability. The edge is also essential in the gas sensor performance because the active sites of MoS_2 are primarily located at the edge of its layer.

Apart from the anions mentioned above, other chalcogen anions, such as selenium and tellurium, are potential doping sources for modifying the structure of MoS_2. The advantage of using chalcogen anions as dopant is the structural similarity with MoS_2 [228]. Therefore, the MoS_2 structure is easily modified without additional impurities and secondary phase. According to Jin et al. [229], the MoSSe Janus structure might improve the gas adsorption properties of MoS_2. Figure 16d shows the adsorption parameters of MoS_2, MoSSe, and $MoSe_2$ on various gas adsorption, including CO, CO_2, NO, NO_2, and NH_3 [229]. The adsorption properties of S- and Se-modified MoSSe surfaces were investigated. The results showed that in the CO and CO_2 gas, the adsorption distance between MoSSe and analyte was greater than 3 Å. This shows that the adsorption process is weak (physisorption). In NH_3, NO, and NO_2 gas, the adsorption distance is less than 3 Å, which is considered strong adsorption (chemisorption). The adsorption distance between MoSSe and adsorbed molecules/gases is closer than MoS_2 and $MoSe_2$. The E_a values (magnitudes) of all the studied molecules adsorbed on the Se-layer were obviously larger than those on the S-layer, indicating the surface selectivity of Janus MoSSe for these molecules. Therefore, gas molecules need to be adsorbed on the Se surface with higher binding strengths. Furthermore, the E_a values of NH_3 and NO_2 adsorption on the Janus layer were relatively larger, leading to higher selectivity of the MoSSe structure. There are several interesting phenomena to be considered in this regard. For instance, CO, CO_2, and NO_2 on the MoSSe act as the charge acceptors while the NH_3 molecule behaves as the charge donor to the Se or S side of the monolayer. Particularly, NO acts as an acceptor on the Se side and as a donor

on the S side. Figure 16d shows the charge density difference between MoSSe samples and adsorbed gases. The obvious charge redistribution occurred in NH_3, NO, and NO_2 gases which were considered as sensitive molecules to be adsorbed by MoSSe structures. The results have demonstrated that the modification of MoSSe has relatively more potential to improve molecular adsorption ability.

Besides the anion doping, modification of MoS_2 structures-led enhanced sensing performances can be conducted by cations elements. Zhu et al. [230] established that Nb, V, and Ta doping into MoS_2 monolayer significantly improves the gas adsorption properties to CO, NO_2, H_2O, and NH_3 molecules. This effect occurs due to the substantial overlap between the metal and orbitals and gas molecule orbitals, leading to activation of the adsorbed gas molecules. Analysis of Bader charge shows that more charge transfer (−0.66 e^- to −0.72 e^-) occurs from metal (V, Nb, Ta)-doped monolayer MoS_2 to the oxidizing gas molecules (NO_2) acting as acceptors. Regarding CO molecules adsorption, relatively fewer electrons (about − 0.24 e^-−0.35 e^-) transfer occured from the substrate to the adsorbed gases. In experimental works, the MoS_2 gas sensing performances have been successfully modified via Zn, Co, Ni, and Fe atomic dopings. These atoms usually replace the Mo atom due to similar cationic behavior. Shao et al. [221] varied the Zn concentration in MoS_2 structures to understand the optimum gas sensing performances optimum condition. Regardless of the tested analytes, the 5%-Zn-doped MoS_2 attained the highest gas sensor. Zhang et al. [231] used Co, Ni, and Fe as dopants sources for MoS_2. The improved SO_2 gas sensor performance was observed in the Co-, Ni-, and Fe-doped MoS_2. Compared to other cations, Ni-doped MoS_2 exhibited the best SO_2 gas sensor performance. DFT calculation showed that the cations-doped MoS_2 increases the adsorption energy, decreases the adsorption distance, and increases the charge transfer process between MoS_2 and SO_2. Moreover, Ni-doped MoS_2 showed the highest adsorption energy, closer adsorption distance, and highest charge transferability. All these results support the anion and cation doping process of MoS_2 that modifies the crystal structure and increases the gas adsorption performance of MoS_2. However, the long-term and phase stability of the anion incorporation into MoS_2 crystal structures against environmental oxidation are lack of detailed studies.

3.6 Heterostructures Coupling

When two dissimilar materials are in contact, heterointerfaces, commonly known as heterojunction, are formed. It offers various advantages to the improvement of many gas sensing materials. The underlying enhanced mechanisms of heterostructures include (i) band structures alteration due to Fermi level adjustment, (ii) depletion layer enlargement, (iii) synergistic surface reaction via electronic sensitization, and (iv) catalytic promotions [28]. Therefore, heterostructures coupling arose as one of the advanced strategies for optimizing gas sensing performances of MoS_2. Many materials have been recently combined with MoS_2 to achieve good gas sensors materials, such as carbon-based materials, oxide materials, and other TMDs materials.

The combination between MoS_2 and carbon-based materials has been widely investigated due to the synergistic effects between the good sensitivity of MoS_2 with the good conductivity and high specific surface area of carbon-based materials. For instance, Sing et al. [232] reported the formation of MoS_2/CNTs heterostructures to detect NH_3 gas at RT. The addition of CNTs into MoS_2 increased the specific surface area. The fabricated sensor devices based on MoS_2 and MoS_2/CNTs illustrated in Fig. 17a exhibited the n-type semiconducting behavior and showed room-temperature NH_3 detection down to 12 ppm-level. Regarding MoS_2, the corresponding response time (t_{res} = 400 s) and recovery time (t_{recov} = 280 s) are very large with LoD down to 1.2 ppm. In comparison, the prepared MoS_2/CNTs exhibited faster response–recovery (65 and 70 s, respectively) features along with enhanced relative response for various ammonia concentrations, ranging from 12 to 325 ppm. The improvement of ammonia detection performance of MoS_2/CNTs is attributed to the higher adsorption energy of MoS_2/CNTs than MoS_2 for ammonia adsorption.

The 2D/2D heterojunction showed fascinating effects on the gas detection improvement governed by large and strong interface contact areas. This is due to the close face-to-face contacts between 2D layered materials. The combination of 2D MoS_2 with 2D graphene-based materials needs to facilitate stronger interfacial electrical coupling and charge transfer than 0D/2D, 1D/2D, and 3D/2D. Park et al. [233] reported the successful formation of MoS_2/RGO composites for water vapors sensing devices with fast response, excellent

 https://doi.org/10.1007/s40820-021-00724-1

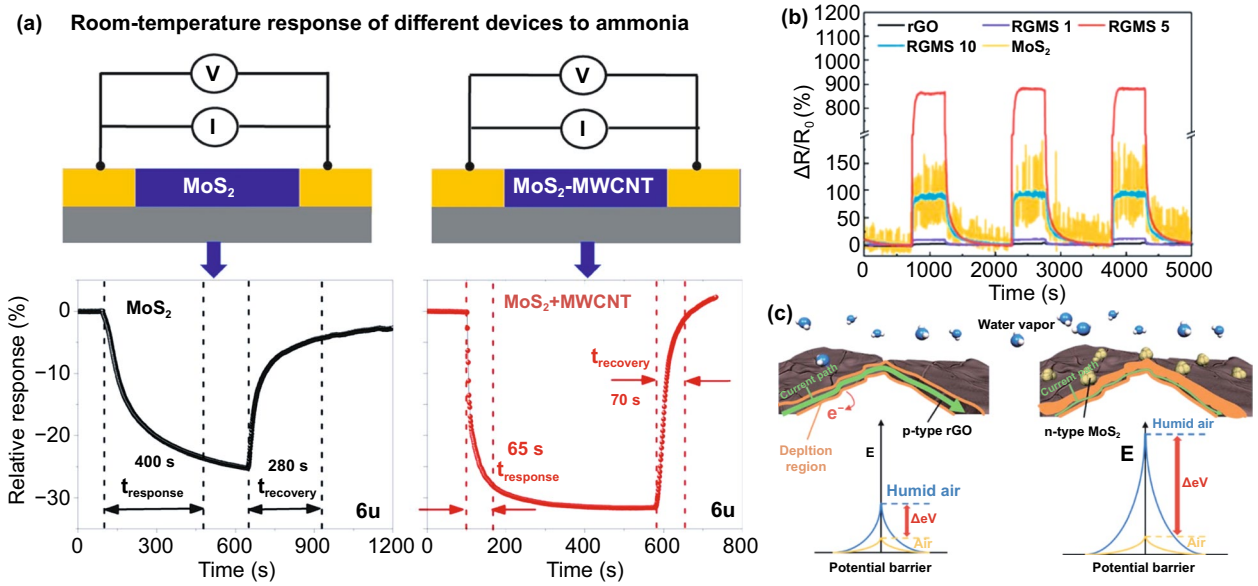

Fig. 17 **a** NH_3 sensor performance of MoS_2 and MoS_2/carbon nanotubes composites Reproduced from Ref. [232]. Copyright 2020, Elsevier. **b** Response curves of rGO, RGMS 1, RGMS 5, RGMS 10, and MoS_2 to 50% RH at room temperature. **c** Schematic of the mechanism with enhanced humidity sensing properties of the enhanced depletion region on bare rGO and RGMS. Reproduced from Ref. [233]. Copyright 2018, The Royal Society of Chemistry

selectivity, and ultrahigh sensitivity based on 2D rGO and 2D MoS_2 hybrid composites (RGMSs). The RGMSs were fabricated by simple ultrasonication without the addition of additives and additional heating. Compared to pristine rGO, the RGMS exhibited a 200 times higher response to water vapors at RT. The significant enhancement in the sensing performance of the composite was attributed to electronic sensitization due to p–n heterojunction formation and porous structures between rGO and MoS_2, as shown in Fig. 17b, c. The synergistic combination of rGO and MoS_2 could be applied to construct a flexible humidity sensor. Besides, a recent study suggested that carbon dots (CDs) can modify the humidity sensing properties of MoS_2 nanosheets because of the abundant surface functional groups of CDs that can possibly adsorb water molecules stronger than the bare MoS_2 [234]. Yue et al. [235] investigated the formation of graphene/MoS_2 quantum dots composites for NH_3 and NO_2 gas recognition. The NO_2 detection gives a negative response value, while the NH_3 detections have a positive response value attributed to the different charge transfer mechanisms between NO_2 and NH_3. In NO_2 gas detection, all sensor materials lose the electron and increase the resistance. In NH_3 detection, the sensor materials gain an electron from NH_3 due to the electron donor properties of NH_3. These results confirm that the combination of MoS_2 and carbon-based materials improve gas sensor performance.

Having many resemblances in term of crystal structures, combining MoS_2 with other TMDs families provide more synergistic process and component suitability, which often increases the gas sensor ability. An assemble heterostructure containing MoS_2 and SnS_2 composite has been successfully fabricated by Liu et al. [236] using a hydrothermal approach. The MoS_2/SnS_2 composite exhibited an outstanding improvement for NO_2 gas detection compared to MoS_2 and SnS_2. The higher NO_2 sensing ability of MoS_2/SnS_2 composites is attributed to the p–n junction formation. In the p–n heterojunction system, the electrons flow from n-type SnS_2 to p-type MoS_2. Consequently, electron depletion layers formed on the surface of SnS_2. Simultaneously, the holes from MoS_2 tend to diffuse to the surface of SnS_2, which leaves a negatively charged region. Electron–hole diffusion continues until the Fermi level of the composite reaches an equilibrium state. The barrier at the SnS_2/MoS_2 interface and the cumulative layer on the surface of the MoS_2 contribute to the low conductivity of the SnS_2/MoS_2 nano-heterostructures in air, confirmed by I–V results. However, in the fresh air, O_2 is adsorbed on the surface of the sensor and changes into O_2^-. When the

sensor is exposed to NO_2 gas, the molecules are adsorbed on the surface of the sensor and capture free electrons from the accepter level of the sensor to form NO_2^-. Also, the NO_2 molecules reacted with chemisorbed oxygen and consequently converted into NO_3, disturbing the electric field's equilibrium to decrease the barrier width and increase the sensor conductivity toward NO_2 gas [236]. The entire process is simplified in Fig. 18a. Ikram et al. [237] demonstrated the synthesis of a heterojunction of few-layer MoS_2 nanosheets (NSs) with multilayer WS_2 using a simple one-pot hydrothermal process. They successfully improved the gas sensing performance of TMD heterostructure nanomaterials (NMs) for NO_2 at room temperature. The response value of MoS_2 and MoS_2@WS_2 with Mo: W atomic ratio of 3.8:1 (MWS-1), 1.55:1 (MWS-2), and 0.36:1 (MWS-3). The NO_2 detection response of all composite samples was higher than MoS_2 samples. Similarly, the response and recovery processes during the NO_2 adsorption are faster than MoS_2. The commendable selectivity and appreciable stability to NO_2 gas are believed to be a synergistic effect between MoS_2 and WS_2 NSs originating from the enhanced surface area and remarkably increased exposed active sites for NO_2 adsorption.

MoS_2 has interesting features to support the performances of oxide-based sensing materials. One major problem of oxide-based is related to the high operating temperature of the oxide materials due to low conductivity. To make oxide-based materials applicable in the room-temperature regime, MoS_2 is needed because of its relatively good conductivity and being reactive at room temperature for diverse types of gases. Han et al. [238] demonstrated MoS_2/ZnO heterostructure's formation for improving NO_2 sensing performance. The purpose of this heterostructure formation is to fabricate the p–n heterostructures as an effective way to modulate the

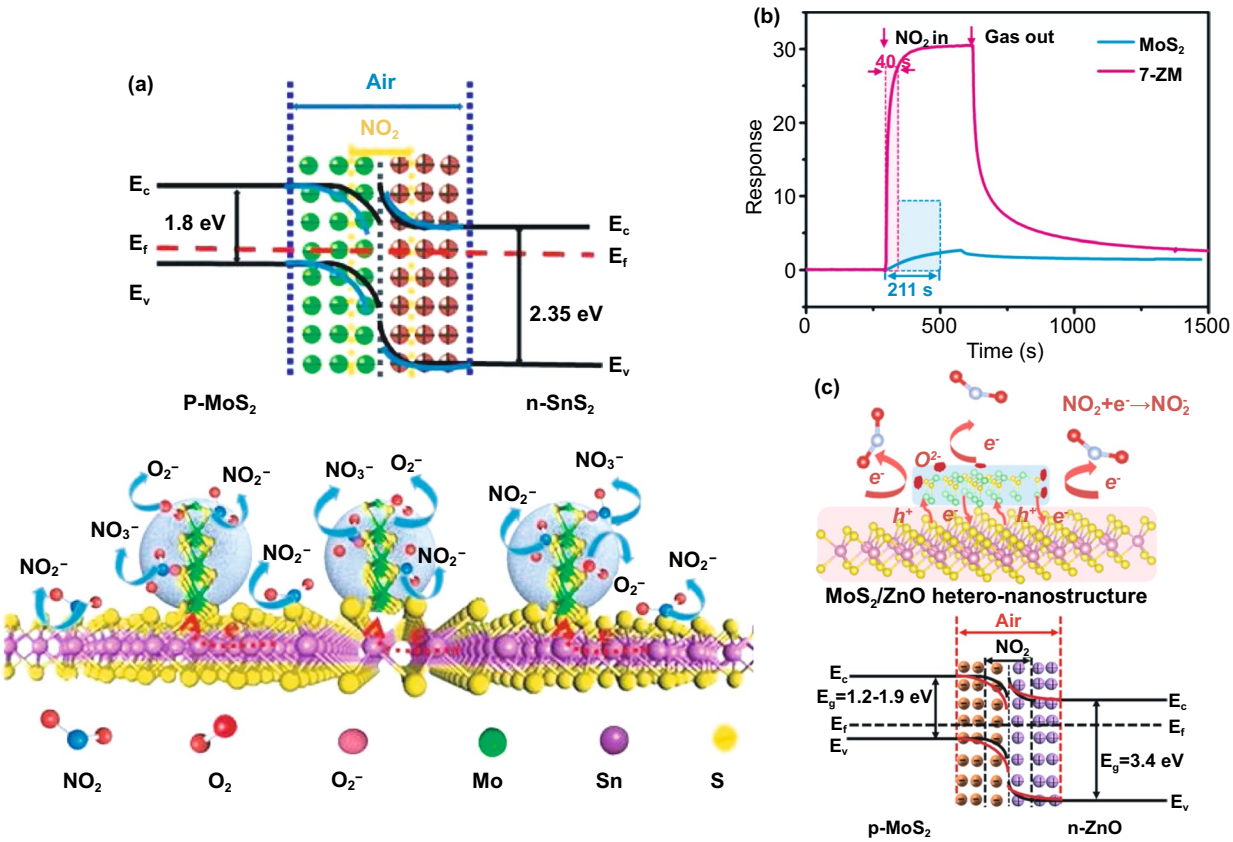

Fig. 18 **a** Schematic of sensing mechanisms of MoS_2/SnS_2 samples the sensors to NO_2. nanocomposite. Reprinted with permission from Ref. [236]. Copyright 2020 Elsevier. **b** Response and recovery curves of MoS_2 NSs and 7-ZM at 5 ppm NO_2. **c** Schematic of sensing mechanisms of MoS_2/ZnO hetero-nanostructures to NO_2 molecules and MoS_2/ZnO hetero-nanostructures energy band structure in Air and a NO_2 atmosphere. Reprinted with permission from Ref. [238]. Copyright 2018 American Chemical Society

https://doi.org/10.1007/s40820-021-00724-1

intrinsic electronic properties of MoS_2 nanosheets (NSs), achieving high sensitivity and excellent recovery properties. Figure 18b shows the comparative NO_2 response between pure MoS_2 and MoS_2/ZnO (7-ZM). The 7-ZM displays superior performance with an excellent response of 30 (R_a/R_g) to 5 ppm NO_2 with a fast response time of 40 s and outstanding recovery ability. Figure 18c shows a graphical illustration of the NO_2 sensing process. During the NO_2 adsorption, the electron from MoS_2 and ZnO tends to move toward NO_2 molecules. Holes accumulate at the surface of MoS_2 NSs, and the width of the heterojunction barriers is decreased. Therefore, the conductivity of MoS_2/ZnO heterostructures greatly increases, contributing to the enhanced response values. Constructing p–n hetero-nanostructures for 2D materials is a versatile solution for achieving excellent sensing performances. According to Wang et al. [239], the combination of MoS_2 and SnO_2 effectively improves gas sensor performance. In this study, the NH_3 sensing performance of MoS_2/SnO_2 at RT was examined. The NH_3 sensing performance of MoS_2/SnO_2 is much higher than MoS_2 and pure MoS_2. They also suggested the improvement of the NH_3 sensing performance of MoS_2/SnO_2 is due to the formation of n–n junction between MoS_2 and SnO_2. In a summary, heterojunction fabrication between MoS_2 and other materials, including carbon-based, TMDs, and oxide materials, has exceptional gas sensing benefits due to the advantages of the interfacial charge transfer mechanism. The computational dynamic simulation may give a deeper understanding of the hole–electron mobility and transfer at the interface, especially during the gas adsorption.

3.7 Other Recent Strategies

3.7.1 Enhancement by Light Irradiation

The recent experimental results have shown that light irradiation effectively increased the gas sensor performance of MoS_2. The light irradiation can have several impacts on the MoS_2 surface, which will benefit gas sensor enhancement. The electron–hole formation is unavoidably existed during the light irradiation due to its small band gap of MoS_2. The increase in the charge carrier formation during light irradiation could improve the sensor response due to increased reaction probability between the charge carrier and gases. Moreover, light irradiation can remove the oxygen ion from the surface, which will be beneficial to increase the reactivity of the tested gas with the MoS_2 surface. Pham et al. [240] have investigated the NO_2 sensor performance of MoS_2 by using red-light irradiation. As mentioned earlier, light irradiation can increase the charge carrier concentration. The increase in the charge carrier concentration directly relates to the increase in the conductivity, as shown in Fig. 19a. The I–V characteristics increase about 500% after light irradiation, which indicates this material is light sensitive. The MoS_2 was deposited on the SiO_2 substrate through spin-coating techniques, and gold was used as an electrical channel. Figure 19b shows the NO_2 response under dark and light irradiation (inset is MoS_2-based sensor device). The NO_2 detection performance of MoS_2 significantly improved after light irradiation and showed extremely high sensitivity to ppb level NO_2 gas exposure up to 3.3% ppb (3300% ppm) and sub-ppb limit of NO_2 gas detection at the 0.1 ppb level. Another report from Kumar et al. [241] has also shown the improvement of the NO_2 sensor of MoS_2 through UV-light irradiation. Figure 19c–e shows the gas sensor performance of MoS_2 under light irradiation, heating treatment, and room temperature. The sensor response of UV-activated is higher than at room temperature and with annealing treatment. Moreover, the response and recovery speed time are greatly improved under UV-light irradiation. The increase in the response and recovery speed under UV-light irradiation is due to the substantial enhancement in response to full reproducibility of multilayer MoS_2 gas sensor to NO_2 gas at room temperature under the UV illumination was attributed to the removal of contamination from the surface (clean surface, renders greatest possible reactive sites per unit volume) and the minor effect of photogenerated electrons in the conduction band of MoS_2.

3.7.2 Substrate Engineering

The electrode preparation is also crucial in designing suitable sensor devices because the different substrates and different electrical channels will give a different electrical signal response. Ali et al. [242] have investigated the detailed preparation of the electrode for gas sensor measurement of MoS_2. The different substrates and also different channel lengths have been carefully conducted. Two kinds of substrate (SiO_2 and h-BN) have been used as a substrate. In MoS_2/h-BN, a

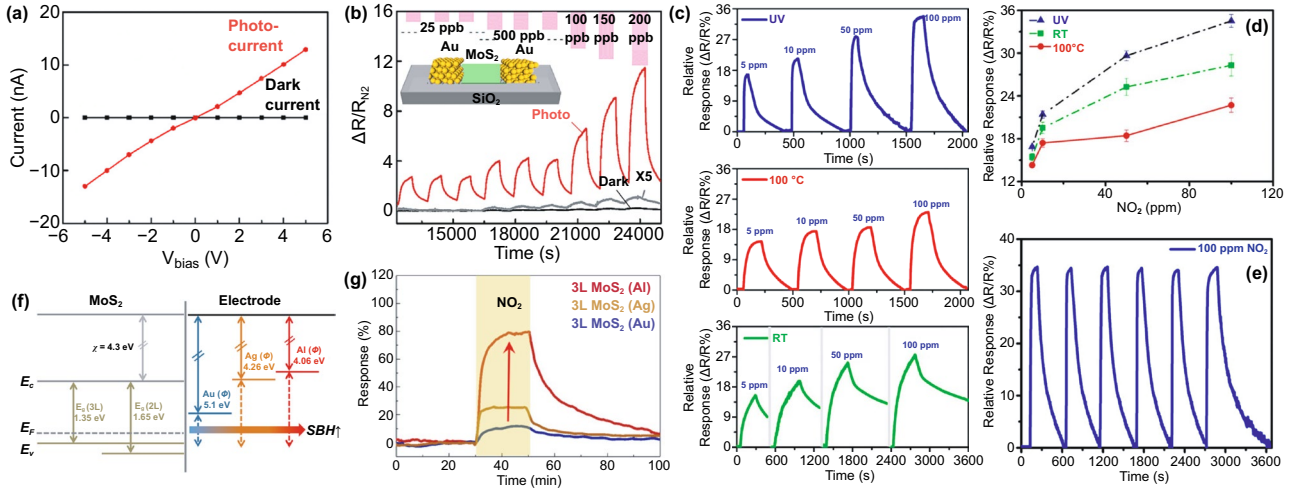

Fig. 19 **a** I–V dependence of the Au–MoS_2–Au device in the dark and under red LED illumination with incident power of 60.9 nW. **b** Effect of NO_2 gas exposure at concentrations from 25 to 200 ppb on normalized resistance of the Au–MoS_2–Au device in the dark (black line; gray line shows fivefold magnified data) and under red LED illumination (red curve). Reproduced from Ref. [240] with permission. Copyright 2019, American Chemical Society. **c** Transient relative response of sensor to 5, 10, 50, and 100 ppm concentration of NO_2 at room temperature (RT), at 100 °C, and at RT under UV illumination (1.2 mW cm^{-2}). **d** Relative response versus NO_2 concentration at RT, 100 °C, and at RT under light. **e** Cyclic test to 100 ppm of NO_2 at RT under UV light. Reproduced from Ref. [241] with permission. Copyright 2017, American Chemical Society. **f** Band diagram of MoS_2 with metal electrodes. **g** Sensing characteristics of NO_2 for 3L MoS_2 with Al, Ag, and Au electrodes. Reproduced from Ref. [243] with permission. Copyright 2019, American Chemical Society

sharp decrease in mobility is observed for low concentration gas exposures, which can be explained by the increase in scattering sites on adsorption of NO_x molecules due to the device being more homogeneous on a flatter substrate. In the case of the MoS_2/SiO_2 device, the change in mobility in NO_x presence is much lower for low concentrations, which shows that influence of surface roughness is more dominant. The different channel length is also crucial for the device with a shorter channel length shows a relatively higher response than a long channel, as the charges undergo less scattering during transport through a shorter channel. Another report from Kim et al. [243] has investigated the difference in channel materials. Three different metals were used. Al, Ag, and Au were used as conductive material for the electrical channel. The use of different conductive materials can change the Schottky barrier height (SBH) due to the different metals' work functions, as shown in Fig. 12f. This Schottky barrier height also affects the gas sensor response. Figure 12g shows that the NO_2 detection performance improves with the lower work function. The electrode with a low work function increased the responsivity.

Each advanced approach has interesting benefits for sensing enhancement. The precise selection and sensor design greatly produce sensors with expected performance and more effective experimental time. To clarify each strategy's contribution, all reviewed strategies to advance the gas sensing performance of MoS_2 are summarized in Table 2.

4 Other Molybdenum-Based Gas Sensor Materials

Concerning α-MoO_3 and MoS_2, other molybdenum-containing compounds have been recently examined for their functionality as next-generation solid-state chemiresistive gas sensing materials with desired specifications. $MoSe_2$ and $MoTe_2$ are in the same family of TMDs, similar to MoS_2, and having two-dimensional layered structures with a high aspect ratio [246]. The physical and electronic properties of $MoSe_2$, such as very narrow band gap (1.1 eV for bulk and 1.5 eV for monolayer), good full-spectrum absorption at 200–800 nm, low internal resistance, and high carrier mobility (100 cm^2 V^{-1} s^{-1}), support its utilization in optoelectronic and photocatalysis application [247, 248]. Specifically, 2D structures manifested by $MoSe_2$ secures the ultra-large specific surface area and abundant surface adsorption sites that govern

 https://doi.org/10.1007/s40820-021-00724-1

Table 2 Improvement strategies of MoS_2-based gas sensor

Improvement strategies	Sensing materials	Target gas	Conc. (ppm)	T (°C)	Sensitivity	Response/recovery times (s)	Refs.
Morphological design	Hierarchically MoS_2 nanospheres	CO	500	230	92.6(R_a/R_g)	18/15	[188]
	3D hierarchical porous MoS_2 microspheres	H_2	500	120	20.5%	30/60	[185]
	MoS_2 nanoflakes	Ethanol Methanol	10	50	17.6(I_D/I_0) 10.8(I_D/I_0)	53/– 67/–	[244]
	3D MoS_2 Aerogel	NO_2	0.5	200	120%	33/107	[195]
	Edge-oriented MoS_2 flakes	H_2	10,000	RT	1%	14.3/136.8	[189]
	Atomic layered MoS_2	NO_2	0.12	RT	35%	*n.a*	[193]
	Monolayer MoS_2	Triethylamine	10	RT	18%	5/5	[190]
	Single- and Multilayer MoS_2	NO	2	RT	80%	*n.a*	[191]
	Monolayer MoS_2	NO_2 NH_3	0.02 1	RT	20% 40%	n.a	[194]
Phase control Surface functionalization	10%1 T $Mo_{0.87}W_{0.13}S_2$	Acetone	100	RT	1.6%	n.a	[206]
	30%1 T $Mo_{0.87}W_{0.13}S_2$	Acetone	1000	RT	0.4%	n.a	[206]
	1 T/2H MoS_2	NO_2	2	RT	25%	10/700	[207]
	1 T/2H (1.7) MoS_2	Toluene	100	RT	12.50%	52/48	[172]
	1 T/2H (4) MoS_2	Toluene	100	RT	16.29%	52/26	[172]
	Au MoS_2	NH_3	1000	60	9.6 (R_a/R_g)	*n.a*	[209]
	Au MoS_2	Triethylamine	50	280	59 (R_a/R_g)	*n.a*	[208]
	Pd-MoS_2	H_2	10,000	RT	35.3%	786/900	[210]
	Pd-MoS_2	H_2	50,000	RT	10 (R_a/R_g)	83/-	[211]
	Pd-MoS_2	H_2	500	RT	33.7%	16/38	[212]
	Ni-MoS_2	H_2S	2	RT	80%	*n.a*	[215]
	Pt-MoS_2	NH_3	70	RT	36%	*n.a*	[213]
	Pt-MoS_2	H_2	100	150	10 (R_a/R_g)	4/19	[214]
	Ni-MoS_2	H_2S	2	RT	80%	*n.a*	[215]
	Ag-MoS_2	Methanol	100	RT	21.6%	*n.a*	[216]
Elemental doping	O-doped MoS_2	H_2O	RH (95%)	RT	47%	228/184	[222]
	Zn-doped MoS_2	O_3	0.6	RT	8%	5.5/10.1	[221]
	Fe-doped MoS_2	SO_2	500	RT	5%	60/107	[231]
	Ni-doped MoS_2	SO_2	500	RT	14%	54/92	[231]
	Co-doped MoS_2	SO_2	500	RT	4%	58/98	[231]
Heterostructures	MoS_2/rGO	H_2O	RH (85%)	RT	2494.25%	6.3/30.8	[233]
	MoS_2 WS_2	NO_2	50	RT	25%	2/36	[237]
	MoS_2/ZnO	NO_2	5	RT	3050%	*n.a*	[238]
	MoS_2/SnO_2	NH_3	50	RT	90 (R_a/R_g)	2.3/1.6	[239]
	MoS_2/SnO_2	NO_2	5	RT	18.7 (G_g/G_a)	74/–	[245]
	MoS_2/Carbon Dots (CDs)	H_2O	RH (15–80%)	RT	0.5 (I_R/I_0)	22/71	[234]

n.a. = data not available

the gas sensing performances. Because of these properties, $MoSe_2$ exhibited excellent sensing performances to sensitively recognize harmful and toxic gases, such as NH_3, NO_2, CO, and H_2S with LoD at ppb level and fast response/recovery times within few seconds [249–252]. 2D $MoSe_2$ nanosheet can be synthesized via a liquid exfoliation approach in which the process is assisted by anhydrous ethanol as dispersant. With only a few layered structures, the 2D $MoSe_2$ exhibited the improved detection to NO_2 gas greater than bulk $MoSe_2$ [253]. Advanced strategies have also been conducted to improve the gas sensing performance of $MoSe_2$, including noble metals functionalization (Au, Pd), morphology and structural control, and nanocomposites [249, 251, 254, 255]. $MoSe_2$ is expected to have a bright prospect in gas sensing in the future. Although there have been extensive studies on MoS_2 and $MoSe_2$, there is still a lack of relevant research on $MoTe_2$ gas sensing properties despite their equivalent structures. $MoTe_2$ has a possible use for environmental monitoring, as initially suggested by Lin and group [256], followed by a few experimental works. $MoTe_2$ demonstrated gas sensing ability to detect as low as 3 ppb of NH_3 gas upon UV-light illumination. Due to the excellent $MoTe_2$ electronic properties, UV light improved NH_3 detectability [257]. Wu et al. stated that the $MoTe_2$ sensing response behaved like a p-type semiconductor. With a similar approach, UV-light-illuminated $MoTe_2$ gas sensors detected NO_2 and ketones with high selectivity [258, 259]. The light-tunable sensing approach is a facile strategy and key performance applied in sensing platforms based on other 2D materials. Due to many structural similarities, the enhanced gas detection performances of $MoSe_2$ and $MoTe_2$ can be expected using approaches performed to MoS_2. Though less pronounced, molybdenum carbide (α-MoC_{1-x} and β-Mo_2C) nanoparticles showed unprecedentedly high signal-to-noise ratio (SNR) with the ability to detect the ppb levels of NH_3 and NO_2 [260]. Furthermore, its chemical stability and high melting temperature properties are suitable for sensing hazardous gases in a harsh environment, which cannot be achieved by oxides semiconducting gas sensor. Hence, the research utilizing other kinds of molybdenum-based sensors is highly encouraged to extend the future high-performance gas sensing materials.

5 Summary and Future Challenge

Extensive studies on molybdenum oxides and dichalcogenides show a significant technological prospect and tremendous assets for multiple functional applications on the environment, energy, and health. Due to excellent and many interesting properties, including 2D layered structures, studies have examined the ability and feasibility of α-MoO_3 and MoS_2 as gas sensing materials. Various advancement strategies of α-MoO_3 and MoS_2 gas sensors have comprehensively been summarized. Regarding pristine α-MoO_3 and MoS_2, enhancement strategy was performed by morphological design and shape control, including 0D (quantum dots), 1D (monolayer nanosheet or nanoplates), 2D (nanorods, nanotubes, nanofibers, nanobelts), and 3D hierarchical structures (microspheres, microflowers, hollow nanostructures) to enlarge their surface area in order to allow more gas adsorption/desorption process and catalytic reactions. Particularly, intrinsic crystal defects in α-MoO_3, such as oxygen vacancy formed after synthesis, provides a highly active site for molecular oxygen adsorption. Similarly, most of the active surface of MoS_2 is situated at the edges of their layered structures. Therefore, it is essential to have phase control synthesis (1 T, 2H, and 3R) in bare MoS_2 to ensure adsorbed oxygen molecules are exposed to their edges-faceted surface. Further effective strategies involve extrinsic chemicals or compounds, either surface functionalization, elemental dopants, and heterostructure coupler. Surface functionalization lowers the activation energy of oxygen dissociation, leading to more abundant ionized oxygens. However, the decorative surface thickness needs to be controlled to avoid blocking oxygen diffusion into sensing materials. Dopants are used to modify electronic, efficient, and crystal structures, mainly for band gap tuning, charge carrier sensitization, and defect formation. The option to heterostructures coupled-α-MoO_3 and MoS_2 is more pronounced to effectively improve gas sensing properties due to widely available developed compounds (other semiconductor ceramics, metals, or polymer) meant for a particular purpose such as extreme environment resistant and flexible/wearable sensors.

The combination of the above strategies can be developed with special attention to their methodological simplicity and effectiveness. In the case of α-MoO_3, this oxide is very suitable for detecting VOCs, especially VOCs containing amine,

 https://doi.org/10.1007/s40820-021-00724-1

due to its acid properties. However, its strong interaction results in a very long recovery time. Until this moment, the available solution is to apply a heating pulse at a relatively high temperature. This strategy is not suitable for α-MoO_3 which can only be operated at low temperatures. Moreover, it cannot be applied to the oxide that is prepared at low temperature due to its properties that tend to change at high temperature, leading to affect its stability. Therefore, it is important to maintain the long-term performance by lowering the operating temperature. Another worth trying strategy is combining the oxide with basic materials such as ZnO. Furthermore, combined with carbon nanotubes (CNT) is can also be done because its report is still rarely be found. Similarly, the gas sensing properties of pristine $MoSe_2$ and $MoTe_2$ can be dramatically tailored by such approaches. Table 3 shows the advantages and disadvantages of each respective strategy.

Despite enormous strategies for optimizing gas sensing properties of α-MoO_3 and α-MoS_2 developed until today, there is still a need to focus on and address some obstacles and challenges. Gas sensors are technologically important in modern society and help control atmospheric pollutions and their exposure to the environment or monitor human health. With the massive growth of information technology and Internet-of-Thing (IoT), the gas sensing research on 2D layered structured materials, including α-MoO_3 and MoS_2, can be integrated into a flexible and wearable sensor to provide real-time gas detection and point-care. For wide deployment, gas sensor device requires ultralow power utilization, low-cost fabrication, high signal-to-noise ratio, long time span, flexibility, and wearability on integrated electronic circuit and miniaturization. Achieving ultralow power consumption is still a critical task because the semiconducting properties of α-MoO_3 require an external heat source to optimize their gas sensing performance, a similar case in MoS_2. Although some works reported that α-MoO_3 and MoS_2 could work at room temperature, the sensitivity is still too low with terribly slow responses. The surface functionalization by noble metals may significantly reduce working temperature and, at the same time, improves the gas sensitivity and creates high-cost sensing devices due to resource shortage and high price. Because of high abundancy, carbon-based may potentially replace noble metals. Employing graphene oxides to ZnO microwires enabled the sensor device to work at room temperature with ultralow consumption [261]. Fabrication of α-MoO_3- and MoS_2-based sensors with ultrahigh signal-to-noise ratio is highly challenging. The ambient environment's intervention, such as humidity or interference gas, leads to high noise background and cross-sensitivity, reducing a "real" electrical signal generated by the tested gases. Therefore, this issue needs to be tackled to produce a highly selective gas sensor.

To realize the room-temperature sensor device, the humidity factor is very crucial to be considered as the major factor because our air consists of different humidity in different situations. If the sensor is stable under different humidity, the sensor is promising as a room-temperature device; however, if the sensor response is greatly altered during the humidity change, the response value is not reliable. Recently, researchers are still struggling with stabilizing the

Table 3 Advantages and disadvantages of each improvement strategy

Strategy	Advantages	Disadvantages
Morphological design	Versatile to obtain nanostructured materials Inexpensive equipment	Surfactant impurity Gas sensing performance cannot be easily predicted
Noble metal functionalization	High catalytic properties of noble metals to organic and non-organic compounds offers faster redox reaction, lead to rapid and high responsivity Reduce working temperature	Resource scarcity High cost Metal toxicity
Phase control	Effective and efficient to highly adsorb analyte by increasing the edge site	Issue on phase stability at certain temperature
Elemental doping	Improve charge carrier concentration Oxygen deficiency induced by charge compensation can be active sites for gas adsorption	Secondary impurity phases Morphology may be changed after doping due to crystal lattice adjustment
Heterostructures	Enhance electron–hole spatial separation More adsorption sites in heterojunction	Requires multistep synthetic approach which means more time and resource consuming In some cases, optimized working temperature increases

sensor response of MoS_2 in a humid environment. Since the MoS_2 is hydrophobic, it is very sensitive to react with water, altering the sensor response. High humidity decreases sensor response decrease. The decrease in the sensor response during the humid environment is due to the competition between water molecules and targeted gas interact with MoS_2 surfaces. In compensation, MoS_2 can be used as a humidity sensing material in practical application.

There is a huge demand economically and environmentally for sensor devices that can retain their sensing properties over thousands of repeated cycles to avoid added recycling costs and electronic waste (e-waste). The stability of α-MoO_3- and MoS_2-based sensors has been achieved for several days, but the measurement was conducted in a laboratory environment. The real test in the various environmental conditions, such as in winter and summer periods, needs to be performed to observe the environmental effect on gas sensing performance. Integration sensing materials and miniaturization into a flexible electronic circuit are fascinating areas for study, yet still far from development. Given layered structures with excellent mechanical properties, α-MoO_3 and α-MoS_2 need to provide high and homogeneous coverage on the interdigitated electrode of a flexible electronic substrate. The feasibility of various flexible substrates needs to be examined. Furthermore, future investigation on the gas sensing performance of α-MoO_3 and MoS_2 given mechanically bent and stretched conditions is needed in the future investigation. Such advancement may develop suitable state-of-the-art integration methodologies and a general guideline. Finally, there is still insufficient understanding of the sensing mechanism despite the availability of many proposed mechanisms previously reported. Working with computational simulation and modeling could help develop advanced knowledge of how gas molecules behave when exposed to sensing materials. This can help design and optimize the next generation of gas sensing materials. A similar effort is needed in examining $MoSe_2$, $MoTe_2$, Mo_2C, MoC, or any other molybdenum-based materials aiming to provide more sensing material choices for a particular application. For example, molybdenum carbides are relatively more suitable for gas sensors working at higher temperatures and severe environments due to greater stability and higher melting points. Overall, molybdenum-based gas sensors hold multiple promising performances toward gas pollutant detections and have drawn great attention to the technological advancement of sensing devices. This review has provided a complete overview of recent strategies on optimizing gas sensing performance of molybdenum-based gas sensors and insight into the further advancement of these special groups as the next-generation sensing materials with high detection ability.

Acknowledgements This research was partly supported by the JSPS Grant-in-Aid for Scientific Research (No. JP16H06439, No. 20H00297), and by the Dynamic Alliance for Open Innovation Bridging Human, Environment and Materials in Network Joint Research Center for Materials and Devices. S.Y acknowledge financial grants provided by Indonesia Ministry of Education, Culture, Research, and Technology, under the scheme of Basic Research Program No. 2/E1/KP.PTNBH/2021 managed by Institut Teknologi Bandung.

Author's Contribution A.H. contributed to conceptualization and visualization; A.H., N.L.W.S., and A.T. contributed to writing—original draft; B.Y. and S.Y. acquired funding and contributed to supervision; B.Y., S., and S.Y. contributed to writing—review and editing; A.H., N.L.W.S., and A.T. are main contributor and have equally contributed.

References

1. B. Brunekreef, S.T. Holgate, Air pollution and health. Lancet **360**, 1233–1242 (2002). https://doi.org/10.1016/S0140-6736(02)11274-8
2. M. Kampa, E. Castanas, Human health effects of air pollution. Environ. Pollut. **151**, 362–367 (2008). https://doi.org/10.1016/j.envpol.2007.06.012
3. J. Lelieveld, J.S. Evans, M. Fnais, D. Giannadaki, A. Pozzer, The contribution of outdoor air pollution sources to premature mortality on a global scale. Nature **525**, 367–371 (2015). https://doi.org/10.1038/nature15371
4. E.G. Snyder, T.H. Watkins, P.A. Solomon, E.D. Thoma, R.W. Williams et al., The changing paradigm of air pollution monitoring. Environ. Sci. Technol. **47**, 11369–11377 (2013). https://doi.org/10.1021/es4022602
5. H. Mayer, Air pollution in cities. Atmos. Environ. **33**, 4029–4037 (1999). https://doi.org/10.1016/S1352-2310(99)00144-2

6. C.K. Chan, X. Yao, Air pollution in mega cities in China. Atmos. Environ. **42**, 1–42 (2008). https://doi.org/10.1016/j.atmosenv.2007.09.003
7. K.-H. Kim, E. Kabir, S. Kabir, A review on the human health impact of airborne particulate matter. Environ. Int. **74**, 136–143 (2015). https://doi.org/10.1016/j.envint.2014.10.005
8. A. Seaton, D. Godden, W. MacNee, K. Donaldson, Particulate air pollution and acute health effects. Lancet **345**, 176–178 (1995). https://doi.org/10.1016/S0140-6736(95)90173-6
9. J.O. Anderson, J.G. Thundiyil, A. Stolbach, Clearing the Air: A review of the effects of particulate matter air pollution on human health. J. Med. Toxicol. **8**, 166–175 (2012). https://doi.org/10.1007/s13181-011-0203-1
10. E. Sanidas, D.P. Papadopoulos, H. Grassos, M. Velliou, K. Tsioufis et al., Air pollution and arterial hypertension. A new risk factor is in the air. J. Am. Soc. Hypertens. **11**, 709–715 (2017). https://doi.org/10.1016/j.jash.2017.09.008
11. P. Kumar, L. Morawska, C. Martani, G. Biskos, M. Neophytou et al., The rise of low-cost sensing for managing air pollution in cities. Environ. Int. **75**, 199–205 (2015). https://doi.org/10.1016/j.envint.2014.11.019
12. S. Das, M. Pal, Review—non-invasive monitoring of human health by exhaled breath analysis: a comprehensive review. J. Electrochem. Soc. **167**, 037562 (2020). https://doi.org/10.1149/1945-7111/ab67a6
13. W. Shin, Medical applications of breath hydrogen measurements chemosensors and chemoreception. Anal. Bioanal. Chem. **406**, 3931–3939 (2014). https://doi.org/10.1007/s00216-013-7606-6
14. Z. Jia, A. Patra, V. Kutty, T. Venkatesan, Critical review of volatile organic compound analysis in breath and in vitro cell culture for detection of lung cancer. Metabolites **9**, 52 (2019). https://doi.org/10.3390/metabo9030052
15. G.F. Fine, L.M. Cavanagh, A. Afonja, R. Binions, Metal oxide semi-conductor gas sensors in environmental monitoring. Sensors **10**, 5469–5502 (2010). https://doi.org/10.3390/s100605469
16. J.H. Lee, Gas sensors using hierarchical and hollow oxide nanostructures: overview. Sens. Actuat. B Chem. **140**, 319–336 (2009). https://doi.org/10.1016/j.snb.2009.04.026
17. M.J. Tierney, H.O.L. Kim, Electrochemical gas sensor with extremely fast response times. Anal. Chem. **65**, 3435–3440 (1993). https://doi.org/10.1021/ac00071a017
18. M.J. Jory, P.S. Vukusic, J.R. Sambles, Development of a prototype gas sensor using surface plasmon resonance on gratings. Sens. Actuat. B Chem. **17**, 203–209 (1994). https://doi.org/10.1016/0925-4005(93)00871-U
19. Z. Jin, Y. Su, Y. Duan, Development of a polyaniline-based optical ammonia sensor. Sens. Actuat. B Chem. **72**, 75–79 (2001). https://doi.org/10.1016/S0925-4005(00)00636-5
20. D.R. Baselt, B. Fruhberger, E. Klaassen, S. Cemalovic, C.L. Britton et al., Design and performance of a microcantilever-based hydrogen sensor. Sens. Actuat. B Chem. **88**, 120–131 (2003). https://doi.org/10.1016/S0925-4005(02)00315-5
21. A.J. Ricco, S.J. Martin, T.E. Zipperian, Surface acoustic wave gas sensor based on film conductivity changes. Sens. Actuat. **8**, 319–333 (1985). https://doi.org/10.1016/0250-6874(85)80031-7
22. N. Barsan, D. Koziej, U. Weimar, Metal oxide-based gas sensor research: How to? Sens. Actuat. B Chem. **121**, 18–35 (2007). https://doi.org/10.1016/j.snb.2006.09.047
23. N. Yamazoe, G. Sakai, K. Shimanoe, Oxide semiconductor gas sensors. Catal. Surv. from Asia **7**, 63–75 (2003). https://doi.org/10.1023/A:1023436725457
24. A. Hermawan, Y. Asakura, M. Inada, S. Yin, One-step synthesis of micro-/mesoporous SnO_2 spheres by solvothermal method for toluene gas sensor. Ceram. Int. **45**, 15435–15444 (2019). https://doi.org/10.1016/j.ceramint.2019.05.043
25. A. Hermawan, Y. Asakura, M. Inada, S. Yin, A facile method for preparation of uniformly decorated-spherical SnO_2 by CuO nanoparticles for highly responsive toluene detection at high temperature. J. Mater. Sci. Technol. **51**, 119–129 (2020). https://doi.org/10.1016/j.jmst.2020.02.041
26. H.M.M. Munasinghe Arachchige, D. Zappa, N. Poli, N. Gunawardhana, E. Comini, Gold functionalized MoO_3 nano flakes for gas sensing applications. Sens. ActuaT. B Chem. **269**, 331–339 (2018). https://doi.org/10.1016/j.snb.2018.04.124
27. G. Eranna, B.C. Joshi, D.P. Runthala, R.P. Gupta, Oxide materials for development of integrated gas sensors - a comprehensive review. Crit. Rev. Solid State Mater. Sci. **29**, 111–188 (2004). https://doi.org/10.1080/10408430490888977
28. D.R. Miller, S.A. Akbar, P.A. Morris, Nanoscale metal oxide-based heterojunctions for gas sensing: a review. Sens. Actuat. B Chem. **204**, 250–272 (2014). https://doi.org/10.1016/j.snb.2014.07.074
29. H.J. Kim, J.H. Lee, Highly sensitive and selective gas sensors using p-type oxide semiconductors: overview. Sens. Actuat. B Chem. **192**, 607–627 (2014). https://doi.org/10.1016/j.snb.2013.11.005
30. G. Korotcenkov, Metal oxides for solid-state gas sensors: What determines our choice? Mater. Sci. Eng. B Solid-State Mater. Adv. Technol. **139**, 1–23 (2007). https://doi.org/10.1016/j.mseb.2007.01.044
31. A. Hermawan, Y. Asakura, M. Kobayashi, M. Kakihana, S. Yin, High temperature hydrogen gas sensing property of GaN prepared from α-GaOOH. Sens. Actuat. B Chem. **276**, 388–396 (2018). https://doi.org/10.1016/j.snb.2018.08.021
32. A. Shokri, N. Salami, Gas sensor based on MoS_2 monolayer. Sens. Actuat. B Chem. **236**, 378–385 (2016). https://doi.org/10.1016/j.snb.2016.06.033
33. N. Yamazoe, J. Hisamoto, N. Miura, S. Kuwata, Potentiometric solid-state oxygen sensor using lanthanum fluoride operative at room temperature. Sens. Actuat. **12**, 415–423 (1987). https://doi.org/10.1016/0250-6874(87)80060-4
34. M. Sajjad, P. Feng, Study the gas sensing properties of boron nitride nanosheets. Mater. Res. Bull. **49**, 35–38 (2014). https://doi.org/10.1016/j.materresbull.2013.08.019

35. C.M. Hung, V.A. Vuong, N. Van Duy, D. Van An, N. Van Hieu et al., Controlled growth of vertically oriented trilayer MoS_2 nanoflakes for room-temperature NO_2 gas sensor applications. Phys. Status Solidi (2020). https://doi.org/10.1002/pssa.202000004
36. M. Yu, H. Shao, G. Wang, F. Yang, C. Liang et al., Interlayer gap widened α-phase molybdenum trioxide as high-rate anodes for dual-ion-intercalation energy storage devices. Nat. Commun. **11**, 1–9 (2020). https://doi.org/10.1038/s41467-020-15216-w
37. T. Liu, Z. Liu, 2D MoS_2 nanostructures for biomedical applications. Adv. Healthc. Mater. **7**, 1–18 (2018). https://doi.org/10.1002/adhm.201701158
38. K. Krishnamoorthy, M. Veerapandian, K. Yun, S.J. Kim, New function of molybdenum trioxide nanoplates: toxicity towards pathogenic bacteria through membrane stress. Coll. Surf. B Biointerf. **112**, 521–524 (2013). https://doi.org/10.1016/j.colsurfb.2013.08.026
39. Y. Jiao, A.M. Hafez, D. Cao, A. Mukhopadhyay, Y. Ma et al., Metallic MoS_2 for high performance energy storage and energy conversion. Small **14**, 1–20 (2018). https://doi.org/10.1002/smll.201800640
40. J. Cheng, C. Wang, X. Zou, L. Liao, Recent advances in optoelectronic devices based on 2D materials and their heterostructures. Adv. Opt. Mater. **7**, 1–15 (2019). https://doi.org/10.1002/adom.201800441
41. E. Singh, P. Singh, K.S. Kim, G.Y. Yeom, H.S. Nalwa, Flexible molybdenum disulfide (MoS_2) atomic layers for wearable electronics and optoelectronics. ACS Appl. Mater. Interf. **11**, 11061–11105 (2019). https://doi.org/10.1021/acsami.8b19859
42. S.S. Sunu, E. Prabhu, V. Jayaraman, K.I. Gnanasekar, T.K. Seshagiri et al., Electrical conductivity and gas sensing properties of MoO_3. Sens. Actuat. B Chem. **101**, 161–174 (2004). https://doi.org/10.1016/j.snb.2004.02.048
43. I.A. de Castro, R.S. Datta, J.Z. Ou, A. Castellanos-Gomez, S. Sriram et al., Molybdenum oxides – from fundamentals to functionality. Adv. Mater. **29**, 1701619 (2017). https://doi.org/10.1002/adma.201701619
44. R. Kumar, W. Zheng, X. Liu, J. Zhang, M. Kumar, MoS_2-based nanomaterials for room-temperature gas sensors. Adv. Mater. Technol. **5**, 1–28 (2020). https://doi.org/10.1002/admt.201901062
45. H. Yan, P. Song, S. Zhang, J. Zhang, Z. Yang et al., Au nanoparticles modified MoO_3 nanosheets with their enhanced properties for gas sensing. Sens. Actuat. B Chem. **236**, 201–207 (2016). https://doi.org/10.1016/j.snb.2016.05.139
46. S. Zhang, P. Song, J. Zhang, Z. Li, Z. Yang et al., In_2O_3-functionalized MoO_3 heterostructure nanobelts with improved gas-sensing performance. RSC Adv. **6**, 50423–50430 (2016). https://doi.org/10.1039/c6ra07292e
47. H. Yan, P. Song, S. Zhang, Z. Yang, Q. Wang, Facile fabrication and enhanced gas sensing properties of hierarchical MoO_3 nanostructures. RSC Adv. **5**, 72728–72735 (2015). https://doi.org/10.1039/c5ra13036k
48. X. Luo, K. You, Y. Hu, S. Yang, X. Pan et al., Rapid hydrogen sensing response and aging of α-MoO_3 nanowires paper sensor. Int. J. Hydrogen Energy **42**, 8399–8405 (2017). https://doi.org/10.1016/j.ijhydene.2017.01.116
49. T. Nagyné-Kovács, L. Studnicka, I.E. Lukács, K. László, P. Pasierb et al., Hydrothermal synthesis and gas sensing of monoclinic MoO_3 nanosheets. Nanomaterials **10**, 891 (2020). https://doi.org/10.3390/nano10050891
50. C.V. Ramana, S. Utsunomiya, R.C. Ewing, C.M. Julien, U. Becker, Structural stability and phase transitions in WO_3 thin films. J. Phys. Chem. B **110**, 10430–10435 (2006). https://doi.org/10.1021/jp056664i
51. T.T.P. Pham, P.H.D. Nguyen, T.T. Vo, H.H.P. Nguyen, C.L. Luu, Facile method for synthesis of nanosized β –MoO_3 and their catalytic behavior for selective oxidation of methanol to formaldehyde. Adv. Nat. Sci. Nanosci. Nanotechnol. **6**, 45010 (2015). https://doi.org/10.1088/2043-6262/6/4/045010
52. L. Zheng, Y. Xu, D. Jin, Y. Xie, Novel metastable hexagonal MoO_3 nanobelts: synthesis, photochromic, and electrochromic properties. Chem. Mater. **21**, 5681–5690 (2009). https://doi.org/10.1021/cm9023887
53. K. Inzani, M. Nematollahi, F. Vullum-Bruer, T. Grande, T.W. Reenaas et al., Electronic properties of reduced molybdenum oxides. Phys. Chem. Chem. Phys. **19**, 9232–9245 (2017). https://doi.org/10.1039/C7CP00644F
54. Q. Zhang, X. Li, Q. Ma, Q. Zhang, H. Bai et al., A metallic molybdenum dioxide with high stability for surface enhanced Raman spectroscopy. Nat. Commun. **8**, 14903 (2017). https://doi.org/10.1038/ncomms14903
55. V. Galstyan, Quantum dots: perspectives in next-generation chemical gas sensors - A review. Anal. Chim. Acta **1152**, 238192 (2021). https://doi.org/10.1016/j.aca.2020.12.067
56. S. Mosadegh Sedghi, Y. Mortazavi, A. Khodadadi, Low temperature CO and CH_4 dual selective gas sensor using SnO_2 quantum dots prepared by sonochemical method. Sens. Actuat. B Chem. **145**, 7–12 (2010). https://doi.org/10.1016/j.snb.2009.11.002
57. H. Singh, A. Kumar, B.S. Bansod, T. Singh, A. Thakur et al., Enhanced moisture sensing properties of a nanostructured ZnO coated capacitive sensor. RSC Adv. **8**, 3839–3845 (2018). https://doi.org/10.1039/c7ra10917b
58. S.J. Xiao, X.J. Zhao, P.P. Hu, Z.J. Chu, C.Z. Huang et al., Highly photoluminescent molybdenum oxide quantum dots: one-pot synthesis and application in 2,4,6-trinitrotoluene determination. ACS Appl. Mater. Interfaces **8**, 8184–8191 (2016). https://doi.org/10.1021/acsami.5b11316
59. N. Wang, D. Tang, H. Zou, S. Jia, Z. Sun et al., Synthesis of molybdenum oxide quantum dots with better dispersity and bio-imaging ability by reduction method. Opt. Mater. **83**, 19–27 (2018). https://doi.org/10.1016/j.optmat.2018.05.065
60. L. Yuan, Y. Niu, R. Li, L. Zheng, Y. Wang et al., Molybdenum oxide quantum dots prepared via a one-step stirring strategy and their application as fluorescent probes for pyrophosphate sensing and efficient antibacterial materials.

 https://doi.org/10.1007/s40820-021-00724-1

J. Mater. Chem. B **6**, 3240–3245 (2018). https://doi.org/10.1039/C8TB00475G

61. Z. Zhang, Z. Yang, X. Chen, D. Hu, Y. Hong, Facile gradient oxidation synthesizing of highly-fluorescent MoO_3 quantum dots for Cr_2O_{72}− trace sensing. Inorg. Chem. Commun. **118**, 108001 (2020). https://doi.org/10.1016/j.inoche.2020.108001
62. X. Lu, R. Wang, L. Hao, F. Yang, W. Jiao et al., Preparation of quantum dots from MoO_3 nanosheets by UV irradiation and insight into morphology changes. J. Mater. Chem. C **4**, 11449–11456 (2016). https://doi.org/10.1039/C6TC04006C
63. T. Li, W. Zeng, Z. Wang, Quasi-one-dimensional metal-oxide-based heterostructural gas-sensing materials: a review. Sens. Actuat. B Chem. **221**, 1570–1585 (2015). https://doi.org/10.1016/j.snb.2015.08.003
64. J. Huang, Q. Wan, Gas sensors based on semiconducting metal oxide one-dimensional nanostructures. Sensors **9**, 9903–9924 (2009). https://doi.org/10.3390/s91209903
65. S. Zhao, Y. Shen, X. Yan, P. Zhou, Y. Yin et al., Complex-surfactant-assisted hydrothermal synthesis of one-dimensional ZnO nanorods for high-performance ethanol gas sensor. Sens. Actuat. B Chem. **286**, 501–511 (2019). https://doi.org/10.1016/j.snb.2019.01.127
66. P. Karnati, S. Akbar, P.A. Morris, Conduction mechanisms in one dimensional core-shell nanostructures for gas sensing: a review. Sens. Actuat. B Chem. **295**, 127–143 (2019). https://doi.org/10.1016/j.snb.2019.05.049
67. M.M. Arafat, B. Dinan, S.A. Akbar, A.S.M.A. Haseeb, Gas sensors based on one dimensional nanostructured metal-oxides: a review. Sensors **12**, 7207–7258 (2012). https://doi.org/10.3390/s120607207
68. S. Cao, C. Zhao, J. Xu, A facile synthesis and controlled growth of various MoO_3 nanostructures and their gas-sensing properties. SN Appl. Sci. **1**, 1–6 (2019). https://doi.org/10.1007/s42452-019-0944-z
69. D. Jiang, Y. Wang, W. Wei, F. Li, Y. Li et al., Xylene sensor based on α-MoO_3 nanobelts with fast response and low operating temperature. RSC Adv. **5**, 18655–18659 (2015). https://doi.org/10.1039/c4ra16976j
70. Y. Mo, Z. Tan, L. Sun, Y. Lu, X. Liu, Ethanol-sensing properties of α-MoO_3 nanobelts synthesized by hydrothermal method. J. Alloys Compd. **812**, 152166 (2020). https://doi.org/10.1016/j.jallcom.2019.152166
71. N.L.W. Septiani, Y.V. Kaneti, Y. Guo, B. Yuliarto, X. Jiang et al., Holey assembly of two-dimensional iron-doped nickel-cobalt layered double hydroxide nanosheets for energy conversion application. Chemsuschem **13**, 1645–1655 (2020). https://doi.org/10.1002/cssc.201901364
72. M.M.Y.A. Alsaif, S. Balendhran, M.R. Field, K. Latham, W. Wlodarski et al., Two dimensional α-MoO_3 nanoflakes obtained using solvent-assisted grinding and sonication method: application for H_2 gas sensing. Sens. Actuat. B Chem. **192**, 196–204 (2014). https://doi.org/10.1016/j.snb.2013.10.107
73. M.M.Y.A. Alsaif, M.R. Field, B.J. Murdoch, T. Daeneke, K. Latham et al., Substoichiometric two-dimensional molybdenum oxide flakes: a plasmonic gas sensing platform. Nanoscale **6**, 12780–12791 (2014). https://doi.org/10.1039/c4nr03073g
74. F. Ji, X. Ren, X. Zheng, Y. Liu, L. Pang et al., 2D-MoO_3 nanosheets for superior gas sensors. Nanoscale **8**, 8696–8703 (2016). https://doi.org/10.1039/c6nr00880a
75. F. Rahman, A. Zavabeti, M.A. Rahman, A. Arash, A. Mazumder et al., Dual selective gas sensing characteristics of 2D α-MoO_{3-x} via a facile transfer process. ACS Appl. Mater. Interf. **11**, 40189–40195 (2019). https://doi.org/10.1021/acsami.9b11311
76. S. Shen, X. Zhang, X. Cheng, Y. Xu, S. Gao et al., Oxygen-vacancy-enriched porous α-MoO_3 nanosheets for trimethylamine sensing. ACS Appl. Nano Mater. **2**, 8016–8026 (2019). https://doi.org/10.1021/acsanm.9b02072
77. P. Bisht, A. Kumar, I.T. Jensen, M. Ahmad, B.D. Belle et al., Enhanced gas sensing response for 2D α-MoO_3 layers: thickness-dependent changes in defect concentration, surface oxygen adsorption, and metal-metal oxide contact. Sens. Actuat. B Chem. **341**, 129953 (2021). https://doi.org/10.1016/j.snb.2021.129953
78. S. He, W. Li, L. Feng, W. Yang, Rational interaction between the aimed gas and oxide surfaces enabling high-performance sensor: the case of acidic α-MoO_3 nanorods for selective detection of triethylamine. J. Alloys Compd. **783**, 574–582 (2019). https://doi.org/10.1016/j.jallcom.2018.12.349
79. Q. Zhou, Q. Zhang, H. Liu, C. Hong, G. Wu et al., Research on gas sensing properties of orthorhombic molybdenum oxide based sensor to hydrogen sulfide. J. Nanoelectron. Optoelectron. **12**, 1072–1076 (2017). https://doi.org/10.1166/jno.2017.2119
80. K. Xu, W. Wei, Y. Sun, W. Lu, T. Yu et al., Design of $NiCo_2O_4$ porous nanosheets/α-MoO_3 nanorods heterostructures for ppb-level ethanol detection. Powder Technol. **345**, 633–642 (2019). https://doi.org/10.1016/j.powtec.2019.01.051
81. Y. Xia, R. Feng, C. Wu, S. Wei, A novel net-like α-MoO_3 nanowires based sensor for the detection of hydrogen sulphide in asphalt. J. Nanoelectron. Optoelectron. **13**, 1235–1238 (2018). https://doi.org/10.1166/jno.2018.2411
82. L. Zhang, Z. Liu, L. Jin, B. Zhang, H. Zhang et al., Self-assembly gridding α-MoO_3 nanobelts for highly toxic H_2 S gas sensors. Sens. Actuat. B Chem. **237**, 350–357 (2016). https://doi.org/10.1016/j.snb.2016.06.104
83. S. Yang, Y. Liu, W. Chen, W. Jin, J. Zhou et al., High sensitivity and good selectivity of ultralong MoO_3 nanobelts for trimethylamine gas. Sens. Actuat. B Chem. **226**, 478–485 (2016). https://doi.org/10.1016/j.snb.2015.12.005
84. Z. Tang, X. Deng, Y. Zhang, X. Guo, J. Yang et al., MoO_3 nanoflakes coupled reduced graphene oxide with enhanced ethanol sensing performance and mechanism. Sens. Actuat. B Chem. **297**, 126730 (2019). https://doi.org/10.1016/j.snb.2019.126730
85. H. Ji, W. Zeng, Y. Li, Assembly of 2D nanosheets into flower-like MoO_3: new insight into the petal thickness affect on gas-sensing properties. Mater. Res. Bull. **118**, 110476 (2019). https://doi.org/10.1016/j.materresbull.2019.05.001

86. N.L.W. Septiani, Y.V. Kaneti, B. Yuliarto, H.K.D. Nugraha et al., Hybrid nanoarchitecturing of hierarchical zinc oxide wool-ball-like nanostructures with multi-walled carbon nanotubes for achieving sensitive and selective detection of sulfur dioxide. Sens. Actuat. B Chem. **261**, 241–251 (2018). https://doi.org/10.1016/j.snb.2018.01.088
87. L. Sui, X. Song, X. Cheng, X. Zhang, Y. Xu et al., An ultraselective and ultrasensitive TEA sensor based on α-MoO_3 hierarchical nanostructures and the sensing mechanism. CrystEngComm **17**, 6493–6503 (2015). https://doi.org/10.1039/c5ce00693g
88. Q. Chen, J. Zheng, X. Liu, X. Zhang, W. Kang et al., First-principles investigations on the mechanism of highly sensitive and selective trimethylamine sensing in MoO_3. Appl. Surf. Sci. **524**, 146520 (2020). https://doi.org/10.1016/j.apsusc.2020.146520
89. B. Mandal, M. Aaryashree, M.T. Das, S.M. Htay, Architecture tailoring of MoO_3 nanostructures for superior ethanol sensing performance. Mater. Res. Bull. **109**, 281–290 (2019)
90. J. Zhang, P. Song, J. Li, Z. Yang, Q. Wang, Template-assisted synthesis of hierarchical MoO_3 microboxes and their high gas-sensing performance. Sens. Actuat. B Chem. **249**, 458–466 (2017). https://doi.org/10.1016/j.snb.2017.04.137
91. Y. Xia, C. Wu, N. Zhao, H. Zhang, Spongy MoO_3 hierarchical nanostructures for excellent performance ethanol sensor. Mater. Lett. **171**, 117–120 (2016). https://doi.org/10.1016/j.matlet.2015.12.159
92. H. Ji, W. Zeng, Y. Li, New insight into the gas-sensing properties of nanofiber-assembled and nanosheet-assembled hierarchical MoO_3 structures. Phys. E Low-Dimen. Syst. Nanostruct. **114**, 113646 (2019). https://doi.org/10.1016/j.physe.2019.113646
93. A. Dey, Semiconductor metal oxide gas sensors: a review. Mater. Sci. Eng. B Solid-State Mater. Adv. Technol. **229**, 206–217 (2018). https://doi.org/10.1016/j.mseb.2017.12.036
94. S. Basu, P.K. Basu, Nanocrystalline metal oxides for methane sensors: role of noble metals. J. Sensors **2009**, 861968 (2009). https://doi.org/10.1155/2009/861968
95. Y. Luo, C. Zhang, B. Zheng, X. Geng, M. Debliquy, Hydrogen sensors based on noble metal doped metal-oxide semiconductor: a review. Int. J. Hydrogen Energy **42**, 20386–20397 (2017). https://doi.org/10.1016/j.ijhydene.2017.06.066
96. L. Sui, X. Zhang, X. Cheng, P. Wang, Y. Xu et al., Au-loaded hierarchical MoO_3 hollow spheres with enhanced gas-sensing performance for the detection of BTX (Benzene, Toluene, And Xylene) and the sensing mechanism. ACS Appl. Mater. Interf. **9**, 1661–1670 (2017). https://doi.org/10.1021/acsami.6b11754
97. J. Zhang, P. Song, Z. Li, S. Zhang, Z. Yang et al., Enhanced trimethylamine sensing performance of single-crystal MoO_3 nanobelts decorated with Au nanoparticles. J. Alloys Compd. **685**, 1024–1033 (2016). https://doi.org/10.1016/j.jallcom.2016.06.257
98. P.C. Nagajyothi, H. Lim, J. Shim, S.B. Rawal, Au nanoparticles supported nanoporous ZnO sphere for enhanced photocatalytic activity under UV-light irradiation. J. Clust. Sci. **27**, 1159–1170 (2016). https://doi.org/10.1007/s10876-016-0980-4
99. K. He, S. He, W. Yang, Q. Tian, Ag nanoparticles-decorated α-MoO_3 nanorods for remarkable and rapid triethylamine-sensing response boosted by pulse-heating technique. J. Alloys Compd. **808**, 151704 (2019). https://doi.org/10.1016/j.jallcom.2019.151704
100. X. Fu, P. Yang, X. Xiao, D. Zhou, R. Huang et al., Ultra-fast and highly selective room-temperature formaldehyde gas sensing of Pt-decorated MoO_3 nanobelts. J. Alloys Compd. **797**, 666–675 (2019). https://doi.org/10.1016/j.jallcom.2019.05.145
101. A.A. Mane, A.V. Moholkar, Palladium (Pd) sensitized molybdenum trioxide (MoO_3) nanobelts for nitrogen dioxide (NO_2) gas detection. Solid. State. Electron. **139**, 21–30 (2018). https://doi.org/10.1016/j.sse.2017.09.011
102. Y. Zhang, O. Pluchery, L. Caillard, A.-F. Lamic-Humblot, S. Casale et al., Sensing the charge state of single gold nanoparticles via work function measurements. Nano Lett. **15**, 51–55 (2015). https://doi.org/10.1021/nl503782s
103. R.S. Ganesh, M. Navaneethan, V.L. Patil, S. Ponnusamy, C. Muthamizhchelvan et al., Sensitivity enhancement of ammonia gas sensor based on Ag/ZnO flower and nanoellipsoids at low temperature. Sens. Actuat. B Chem. **255**, 672–683 (2018). https://doi.org/10.1016/j.snb.2017.08.015
104. J. Wang, S. Rathi, B. Singh, I. Lee, S. Maeng et al., Dielectrophoretic assembly of Pt nanoparticle-reduced graphene oxide nanohybrid for highly-sensitive multiple gas sensor. Sens. Actuat. B Chem. **220**, 755–761 (2015). https://doi.org/10.1016/j.snb.2015.05.133
105. N. Van Toan, N. Viet Chien, N. Van Duy, H. Si Hong, H. Nguyen et al., Fabrication of highly sensitive and selective H_2 gas sensor based on SnO_2 thin film sensitized with microsized Pd islands. J. Hazard. Mater. **301**, 433–442 (2016). https://doi.org/10.1016/j.jhazmat.2015.09.013
106. H. Fu, Z. Wu, X. Yang, P. He, X. An et al., Ultra-high sensitivity and selectivity of Au nanoparticles modified MoO_3 nanobelts towards 1-butylamine. Appl. Surf. Sci. **542**, 148721 (2021). https://doi.org/10.1016/j.apsusc.2020.148721
107. F. Li, S. Guo, J. Shen, L. Shen, D. Sun et al., Xylene gas sensor based on Au-loaded $WO_3{\cdot}H_2O$ nanocubes with enhanced sensing performance. Sens. Actuat. B Chem. **238**, 364–373 (2017). https://doi.org/10.1016/j.snb.2016.07.021
108. Q. Rong, Y. Zhang, T. Lv, K. Shen, B. Zi et al., Highly selective and sensitive methanol gas sensor based on molecular imprinted silver-doped $LaFeO_3$ core–shell and cage structures. Nanotechnology **29**, 145503 (2018). https://doi.org/10.1088/1361-6528/aaabd0
109. W. Quan, X. Hu, X. Min, J. Qiu, R. Tian et al., A highly sensitive and selective ppb-level acetone sensor based on a Pt-doped 3D porous SnO_2 hierarchical structure. Sensors **20**, 1150 (2020). https://doi.org/10.3390/s20041150
110. Y.J. Kwon, H.G. Na, S.Y. Kang, S. Choi, S.S. Kim et al., Selective detection of low concentration toluene gas using Pt-decorated carbon nanotubes sensors. Sens. Actuat. B

 https://doi.org/10.1007/s40820-021-00724-1

Chem. **227**, 157–168 (2016). https://doi.org/10.1016/j.snb.2015.12.024

111. U. Inpan, P. Leangtanom, D. Phokharatkul, A. Wisitsoraat, S. Phanichphant et al., H_2S gas sensor based on Ru-MoO_3 nanoflake thick film. J. Nanosci. Nanotechnol. **19**, 1780–1785 (2019). https://doi.org/10.1166/jnn.2019.16197
112. D. Degler, U. Weimar, N. Barsan, Current understanding of the fundamental mechanisms of doped and loaded semiconducting metal-oxide-based gas sensing materials. ACS Sensors **4**, 2228–2249 (2019). https://doi.org/10.1021/acssensors.9b00975
113. L. Sui, Y.-M. Xu, X.-F. Zhang, X.-L. Cheng, S. Gao et al., Construction of three-dimensional flower-like α-MoO_3 with hierarchical structure for highly selective triethylamine sensor. Sens. Actuat. B Chem. **208**, 406–414 (2015). https://doi.org/10.1016/j.snb.2014.10.138
114. Y.H. Cho, Y.N. Ko, Y.C. Kang, I.-D. Kim, J.-H. Lee, Ultraselective and ultrasensitive detection of trimethylamine using MoO_3 nanoplates prepared by ultrasonic spray pyrolysis. Sens. Actuat. B Chem. **195**, 189–196 (2014). https://doi.org/10.1016/j.snb.2014.01.021
115. A.A. Mane, A.V. Moholkar, Palladium (Pd) sensitized molybdenum trioxide (MoO_3) nanobelts for nitrogen dioxide (NO_2) gas detection. Solid-State Electron. **139**, 21–30 (2018). https://doi.org/10.1016/j.sse.2017.09.011
116. W. Jiang, L. Meng, S. Zhang, X. Chuai, Z. Zhou et al., Design of highly sensitive and selective xylene gas sensor based on Ni-doped MoO3 nano-pompon. Sens. Actuat. B Chem. **299**, 126888 (2019). https://doi.org/10.1016/j.snb.2019.126888
117. Q.-Y. Ouyang, L. Li, Q.-S. Wang, Y. Zhang, T.-S. Wang et al., Facile synthesis and enhanced H_2S sensing performances of Fe-doped α-MoO_3 micro-structures. Sens. Actuat. B Chem. **169**, 17–25 (2012). https://doi.org/10.1016/j.snb.2012.01.042
118. Z. Li, W. Wang, Z. Zhao, X. Liu, P. Song, Facile synthesis and enhanced trimethylamine sensing performances of W-doped MoO_3 nanobelts. Mater. Sci. Semicond. Process. **66**, 33–38 (2017). https://doi.org/10.1016/j.mssp.2017.04.002
119. R. Xu, N. Zhang, L. Sun, C. Chen, Y. Chen et al., One-step synthesis and the enhanced xylene-sensing properties of Fe-doped MoO_3 nanobelts. RSC Adv. **6**, 106364–106369 (2016). https://doi.org/10.1039/c6ra22268d
120. S. Wang, J. Xie, J. Hu, H. Qin, Y. Cao, Fe-doped α-MoO_3 nanoarrays: Facile solid-state synthesis and excellent xylene-sensing performance. Appl. Surf. Sci. **512**, 145722 (2020). https://doi.org/10.1016/j.apsusc.2020.145722
121. G. Lei, Z. Wang, J. Xiong, S. Yang, H. Xu et al., The enhanced hydrogen-sensing performance of the Fe-doped MoO_3 monolayer: A DFT study. Int. J. Hydrogen Energy **45**, 10257–10267 (2020). https://doi.org/10.1016/j.ijhydene.2020.01.238
122. J. Wang, Q. Zhou, Z. Wei, L. Xu, W. Zeng, Experimental and theoretical studies of Zn-doped MoO_3 hierarchical microflower with excellent sensing performances to carbon monoxide. Ceram. Int. **46**, 29222–29232 (2020). https://doi.org/10.1016/j.ceramint.2020.08.096
123. X. Li, D. Jiang, Y. Fan, N. Zhang, C. Liu et al., The effects of Zr-doping on improving the sensitivity and selectivity of a one-dimensional α-MoO_3-based xylene gas sensor. Inorg. Chem. Front. **7**, 1704–1712 (2020). https://doi.org/10.1039/d0qi00019a
124. W. Li, S. He, L. Feng, W. Yang, Cr-doped α-MoO_3 nanorods for the fast detection of triethylamine using a pulse-heating strategy. Mater. Lett. **250**, 143–146 (2019). https://doi.org/10.1016/j.matlet.2019.05.006
125. Z. Li, W. Wang, Z. Zhao, X. Liu, P. Song, One-step hydrothermal preparation of Ce-doped MoO_3 nanobelts with enhanced gas sensing properties. RSC Adv. **7**, 28366–28372 (2017). https://doi.org/10.1039/c7ra02893h
126. S. Bai, C. Chen, D. Zhang, R. Luo, D. Li et al., Intrinsic characteristic and mechanism in enhancing H_2S sensing of Cd-doped α-MoO_3 nanobelts. Sens. Actuat. B Chem. **204**, 754–762 (2014). https://doi.org/10.1016/j.snb.2014.08.017
127. S. Yang, Y. Liu, T. Chen, W. Jin, T. Yang et al., Zn doped MoO_3 nanobelts and the enhanced gas sensing properties to ethanol. Appl. Surf. Sci. **393**, 377–384 (2017). https://doi.org/10.1016/j.apsusc.2016.10.021
128. K. Liu, W. Zhang, F. Lei, L. Liang, B. Gu et al., Nitrogen-doping induced oxygen divacancies in freestanding molybdenum trioxide single-layers boosting electrocatalytic hydrogen evolution. Nano Energy **30**, 810–817 (2016). https://doi.org/10.1016/j.nanoen.2016.09.015
129. P. Qin, G. Fang, F. Cheng, W. Ke, H. Lei et al., Sulfur-doped molybdenum oxide anode interface layer for organic solar cell application. ACS Appl. Mater. Interf. **6**, 2963–2973 (2014). https://doi.org/10.1021/am405571a
130. Y. Zhao, Z. Jin, Z. Liu, Y. Xu, L. Lu et al., Sulfur doped molybdenum oxide quantum dots as efficient fluorescent labels and bacteriostatic. Inorg. Chem. Commun. **122**, 108275 (2020). https://doi.org/10.1016/j.inoche.2020.108275
131. S. Bandaru, G. Saranya, N.J. English, C. Yam, M. Chen, Tweaking the electronic and optical properties of α-MoO_3 by sulphur and selenium doping- a density functional theory study. Sci. Rep. **8**, 10144 (2018). https://doi.org/10.1038/s41598-018-28522-7
132. B.A. Davis, B. Chakraborty, N. Kalarikkal, L.M. Ramaniah, Room temperature ferromagnetism in carbon doped MoO_3 for spintronic applications: a DFT study. J. Magn. Magn. Mater. **502**, 166503 (2020). https://doi.org/10.1016/j.jmmm.2020.166503
133. Y. Linghu, C. Wu, Gas molecules on defective and nonmetal-doped MoS_2 monolayers. J. Phys. Chem. C **124**, 1511–1522 (2020). https://doi.org/10.1021/acs.jpcc.9b10450
134. J. Li, H. Liu, H. Fu, L. Xu, H. Jin et al., Synthesis of 1D α-MoO_3/0D ZnO heterostructure nanobelts with enhanced gas sensing properties. J. Alloys Compd. **788**, 248–256 (2019). https://doi.org/10.1016/j.jallcom.2019.02.086
135. J. Yang, J. Liu, B. Li, L. Han, Y. Xu, A microcube-like hierarchical heterostructure of α-Fe_2O_3@α-MoO_3 for trimethylamine sensing. Dalt. Trans. **49**, 8114–8121 (2020). https://doi.org/10.1039/D0DT01521K

136. D. Zappa, V. Galstyan, N. Kaur, H.M.M. Munasinghe Arachchige, O. Sisman et al., Metal oxide -based heterostructures for gas sensors- a review. Anal. Chim. Acta **1039**, 1–23 (2018)
137. D. Jiang, W. Wei, F. Li, Y. Li, C. Liu et al., Xylene gas sensor based on α-MoO_3/α-Fe_2O_3 heterostructure with high response and low operating temperature. RSC Adv. **5**, 39442–39448 (2015). https://doi.org/10.1039/c5ra05661f
138. Z. Li, P. Song, Z. Yang, Q. Wang, In situ formation of one-dimensional $CoMoO_4$/MoO_3 heterojunction as an effective trimethylamine gas sensor. Ceram. Int. **44**, 3364–3370 (2018). https://doi.org/10.1016/j.ceramint.2017.11.126
139. F. Qu, X. Zhou, B. Zhang, S. Zhang, C. Jiang et al., Fe_2O_3 nanoparticles-decorated MoO_3 nanobelts for enhanced chemiresistive gas sensing. J. Alloys Compd. **782**, 672–678 (2019). https://doi.org/10.1016/j.jallcom.2018.12.258
140. F. Zhang, X. Dong, X. Cheng, Y. Xu, X. Zhang et al., Enhanced gas-sensing properties for trimethylamine at low temperature based on MoO_3/$Bi_2Mo_3O_{12}$ hollow microspheres. ACS Appl. Mater. Interf. **11**, 11755–11762 (2019). https://doi.org/10.1021/acsami.8b22132
141. S. Bai, C. Chen, R. Luo, A. Chen, D. Li, Synthesis of MoO_3/reduced graphene oxide hybrids and mechanism of enhancing H2S sensing performances. Sens. Actuat. B Chem. **216**, 113–120 (2015). https://doi.org/10.1016/j.snb.2015.04.036
142. S. Bai, C. Chen, M. Cui, R. Luo, A. Chen et al., Rapid synthesis of rGO-MoO_3 hybrids and mechanism of enhancing sensing performance to H_2S. RSC Adv. **5**, 50783–50789 (2015). https://doi.org/10.1039/c5ra06716b
143. M. MalekAlaie, M. Jahangiri, A.M. Rashidi, A. HaghighiAsl, N. Izadi, Selective hydrogen sulfide (H_2S) sensors based on molybdenum trioxide (MoO_3) nanoparticle decorated reduced graphene oxide. Mater. Sci. Semicond. Process. **38**, 93–100 (2015). https://doi.org/10.1016/j.mssp.2015.03.034
144. S. Some, Y. Xu, Y. Kim, Y. Yoon, H. Qin et al., Highly sensitive and selective gas sensor using hydrophilic and hydrophobic graphenes. Sci. Rep. **3**, 1868 (2013). https://doi.org/10.1038/srep01868
145. Y.P. Venkata Subbaiah, K.J. Saji, A. Tiwari, Atomically thin MoS2: a versatile nongraphene 2D material. Adv. Funct. Mater. **26**, 2046–2069 (2016). https://doi.org/10.1002/adfm.201504202
146. K.F. Mak, C. Lee, J. Hone, J. Shan, T.F. Heinz, Atomically thin MoS_2: a new direct-gap semiconductor. Phys. Rev. Lett. **105**, 2–5 (2010). https://doi.org/10.1103/PhysRevLett.105.136805
147. W. Zhao, J. Pan, Y. Fang, X. Che, D. Wang et al., Metastable MoS2: crystal structure, electronic band structure, synthetic approach and intriguing physical properties. Chem. A Eur. J. **24**, 15942–15954 (2018). https://doi.org/10.1002/chem.201801018
148. R.J. Toh, Z. Sofer, J. Luxa, D. Sedmidubský, M. Pumera, 3R phase of MoS_2 and WS_2 outperforms the corresponding 2H phase for hydrogen evolution. Chem. Commun. **53**, 3054–3057 (2017). https://doi.org/10.1039/c6cc09952a
149. F. Schwierz, Graphene transistors. Nat. Nanotechnol. **5**, 487–496 (2010). https://doi.org/10.1038/nnano.2010.89
150. G. Eda, T. Fujita, H. Yamaguchi, D. Voiry, M. Chen et al., Coherent atomic and electronic heterostructures of single-layer MoS_2. ACS Nano **6**, 7311–7317 (2012). https://doi.org/10.1021/nn302422x
151. B. Pal, A. Singh, S.G., P. Mahale, A. Kumar, et al., Chemically exfoliated MoS_2 layers: spectroscopic evidence for the semiconducting nature of the dominant trigonal metastable phase. Phys. Rev. B **96**, 195426 (2017). https://doi.org/10.1103/PhysRevB.96.195426
152. J. Heising, M.G. Kanatzidis, Structure of restacked MoS_2 and WS_2 elucidated by electron crystallography. J. Am. Chem. Soc. **121**, 638–643 (1999). https://doi.org/10.1021/ja983043c
153. J. Heising, M.G. Kanatzidis, Exfoliated and restacked MoS_2 and WS_2: Ionic or neutral species? Encapsulation and ordering of hard electropositive cations. J. Am. Chem. Soc. **121**, 11720–11732 (1999). https://doi.org/10.1021/ja991644d
154. B. Radisavljevic, A. Radenovic, J. Brivio, V. Giacometti, A. Kis, Single-layer MoS_2 transistors. Nat. Nanotechnol. **6**, 147–150 (2011). https://doi.org/10.1038/nnano.2010.279
155. A. Molina-Sánchez, K. Hummer, L. Wirtz, Vibrational and optical properties of MoS2: from monolayer to bulk. Surf. Sci. Rep. **70**, 554–586 (2015). https://doi.org/10.1016/j.surfrep.2015.10.001
156. S. Bertolazzi, J. Brivio, A. Kis, Stretching and breaking of ultrathin MoS_2. ACS Nano **5**, 9703–9709 (2011). https://doi.org/10.1021/nn203879f
157. J. Pu, Y. Yomogida, K.-K. Liu, L.-J. Li, Y. Iwasa et al., Highly flexible MoS_2 thin-film transistors with ion gel dielectrics. Nano Lett. **12**, 4013–4017 (2012). https://doi.org/10.1021/nl301335q
158. K.S. Novoselov, D. Jiang, F. Schedin, T.J. Booth, V.V. Khotkevich et al., Two-dimensional atomic crystals. Proc. Natl. Acad. Sci. **102**, 10451–10453 (2005). https://doi.org/10.1073/pnas.0502848102
159. S. Najmaei, M. Amani, M.L. Chin, Z. Liu, A.G. Birdwell et al., Electrical transport properties of polycrystalline monolayer molybdenum disulfide. ACS Nano **8**, 7930–7937 (2014). https://doi.org/10.1021/nn501701a
160. K.M. Garadkar, A.A. Patil, P.P. Hankare, P.A. Chate, D.J. Sathe et al., MoS_2: preparation and their characterization. J. Alloys Compd. **487**, 786–789 (2009). https://doi.org/10.1016/j.jallcom.2009.08.069
161. H. Gao, H. Gao, J. Suh, J. Suh, M.C. Cao et al., Tuning electrical conductance of MoS_2 monolayers through substitutional doping. Nano Lett. **20**, 4095–4101 (2020). https://doi.org/10.1021/acs.nanolett.9b05247
162. R. Kappera, D. Voiry, S.E. Yalcin, B. Branch, G. Gupta et al., Phase-engineered low-resistance contacts for ultrathin MoS_2 transistors. Nat. Mater. **13**, 1128–1134 (2014). https://doi.org/10.1038/nmat4080
163. Y. Li, L. Wang, S. Zhang, X. Dong, Y. Song et al., Cracked monolayer 1T MoS_2 with abundant active sites for enhanced electrocatalytic hydrogen evolution. Catal. Sci. Technol. **7**, 718–724 (2017). https://doi.org/10.1039/C6CY02649D

 https://doi.org/10.1007/s40820-021-00724-1

164. J.Y. Kim, S.M. Choi, W.S. Seo, W.S. Cho, Thermal and electronic properties of exfoliated metal chalcogenides. Bull. Korean Chem. Soc. **31**, 3225–3227 (2010). https://doi.org/10.5012/bkcs.2010.31.11.3225
165. R. Yan, J.R. Simpson, S. Bertolazzi, J. Brivio, M. Watson et al., Thermal conductivity of monolayer molybdenum disulfide obtained from temperature-dependent Raman spectroscopy. ACS Nano **8**, 986–993 (2014). https://doi.org/10.1021/nn405826k
166. I. Jo, M.T. Pettes, E. Ou, W. Wu, L. Shi, Basal-plane thermal conductivity of few-layer molybdenum disulfide. Appl. Phys. Lett. **104**, 201902 (2014). https://doi.org/10.1063/1.4876965
167. S. Sahoo, A.P.S. Gaur, M. Ahmadi, M.J.F. Guinel, R.S. Katiyar, Temperature-dependent Raman studies and thermal conductivity of few-layer MoS_2. J. Phys. Chem. C **117**, 9042–9047 (2013). https://doi.org/10.1021/jp402509w
168. J.V. Lauritsen, M.V. Bollinger, E. Lægsgaard, K.W. Jacobsen, J.K. Nørskov et al., Atomic-scale insight into structure and morphology changes of MoS_2 nanoclusters in hydrotreating catalysts. J. Catal. **221**, 510–522 (2004). https://doi.org/10.1016/j.jcat.2003.09.015
169. M.V. Bollinger, J.V. Lauritsen, K.W. Jacobsen, J.K. Nørskov, S. Helveg et al., One-dimensional metallic edge states in MoS_2. Phys. Rev. Lett. **87**, 196803 (2001). https://doi.org/10.1103/PhysRevLett.87.196803
170. H. Wang, C. Li, P. Fang, Z. Zhang, J.Z. Zhang, Synthesis, properties, and optoelectronic applications of two-dimensional MoS_2 and MoS_2 -based heterostructures. Chem. Soc. Rev. **47**, 6101–6127 (2018). https://doi.org/10.1039/C8CS00314A
171. T.H.M. Lau, S. Wu, R. Kato, T.S. Wu, J. Kulhavý et al., Engineering monolayer 1T-MoS_2 into a bifunctional electrocatalyst via sonochemical doping of isolated transition metal atoms. ACS Catal. **9**, 7527–7534 (2019). https://doi.org/10.1021/acscatal.9b01503
172. A. Taufik, Y. Asakura, H. Kato, M. Kakihana, R. Saleh et al., 1T/2H-MoS_2 engineered by in-situ ethylene glycol intercalation for improved toluene sensing response at room temperature. Adv. Powder Technol. **31**, 1868–1878 (2020). https://doi.org/10.1016/j.apt.2020.02.022
173. E. Lee, Y.S. Yoon, D.J. Kim, Two-dimensional transition metal dichalcogenides and metal oxide hybrids for gas sensing. ACS Sens. **3**, 2045–2060 (2018). https://doi.org/10.1021/acssensors.8b01077
174. B. Cho, M.G. Hahm, M. Choi, J. Yoon, A.R. Kim et al., Charge-transfer-based gas sensing using atomic-layer MoS_2. Sci. Rep. **5**, 8052 (2015). https://doi.org/10.1038/srep08052
175. Q. Yue, Z. Shao, S. Chang, J. Li, Adsorption of gas molecules on monolayer MoS_2 and effect of applied electric field. Nanoscale Res. Lett. **8**, 425 (2013). https://doi.org/10.1186/1556-276X-8-425
176. D.J. Late, Y.K. Huang, B. Liu, J. Acharya, S.N. Shirodkar et al., Sensing behavior of atomically thin-layered MoS_2 transistors. ACS Nano **7**, 4879–4891 (2013). https://doi.org/10.1021/nn400026u
177. Y. Feng, K. Zhang, H. Li, F. Wang, B. Zhou et al., In situ visualization and detection of surface potential variation of mono and multilayer MoS_2 under different humidities using Kelvin probe force microscopy. Nanotechnology (2017). https://doi.org/10.1088/1361-6528/aa7183
178. M. Li, D. Wang, J. Li, Z. Pan, H. Ma et al., Surfactant-assisted hydrothermally synthesized MoS_2 samples with controllable morphologies and structures for anthracene hydrogenation. Chin. J. Catal. **38**, 597–606 (2017). https://doi.org/10.1016/S1872-2067(17)62779-7
179. G. Tang, J. Zhang, C. Liu, D. Zhang, Y. Wang et al., Synthesis and tribological properties of flower-like MoS_2 microspheres. Ceram. Int. **40**, 11575–11580 (2014). https://doi.org/10.1016/j.ceramint.2014.03.115
180. Y. Zhang, W. Zeng, Y. Li, Hydrothermal synthesis and controlled growth of hierarchical 3D flower-like MoS_2 nanospheres assisted with CTAB and their NO_2 gas sensing properties. Appl. Surf. Sci. **455**, 276–282 (2018). https://doi.org/10.1016/j.apsusc.2018.05.224
181. X. Wang, Z. Zhang, Y. Chen, Y. Qu, Y. Lai et al., Morphology-controlled synthesis of MoS_2 nanostructures with different lithium storage properties. J. Alloys Compd. **600**, 84–90 (2014). https://doi.org/10.1016/j.jallcom.2014.02.127
182. H. Hwang, H. Kim, J. Cho, MoS_2 nanoplates consisting of disordered graphene-like layers for high rate lithium battery anode materials. Nano Lett. **11**, 4826–4830 (2011). https://doi.org/10.1021/nl202675f
183. M. Wang, G. Li, H. Xu, Y. Qian, J. Yang, Enhanced lithium storage performances of hierarchical hollow MoS_2 nanoparticles assembled from nanosheets. ACS Appl. Mater. Interf. **5**, 1003–1008 (2013). https://doi.org/10.1021/am3026954
184. S. Kumari, R. Gusain, N. Kumar, O.P. Khatri, PEG-mediated hydrothermal synthesis of hierarchical microspheres of MoS_2 nanosheets and their potential for lubrication application. J. Ind. Eng. Chem. **42**, 87–94 (2016). https://doi.org/10.1016/j.jiec.2016.07.038
185. Y. Zhang, W. Zeng, Y. Li, The hydrothermal synthesis of 3D hierarchical porous MoS_2 microspheres assembled by nanosheets with excellent gas sensing properties. J. Alloys Compd. **749**, 355–362 (2018). https://doi.org/10.1016/j.jallcom.2018.03.307
186. U.K. Sen, S. Mitra, High-rate and high-energy-density lithium-ion battery anode containing 2D MoS_2 nanowall and cellulose binder. ACS Appl. Mater. Interf. **5**, 1240–1247 (2013). https://doi.org/10.1021/am3022015
187. L. Ye, H. Xu, D. Zhang, S. Chen, Synthesis of bilayer MoS_2 nanosheets by a facile hydrothermal method and their methyl orange adsorption capacity. Mater. Res. Bull. **55**, 221–228 (2014). https://doi.org/10.1016/j.materresbull.2014.04.025
188. Q. Zhou, C. Hong, Y. Yao, S. Hussain, L. Xu et al., Hierarchically MoS_2 nanospheres assembled from nanosheets for superior CO gas-sensing properties. Mater. Res. Bull. **101**, 132–139 (2018). https://doi.org/10.1016/j.materresbull.2018.01.030

189. A.V. Agrawal, R. Kumar, S. Venkatesan, A. Zakhidov, Z. Zhu et al., Fast detection and low power hydrogen sensor using edge-oriented vertically aligned 3-D network of MoS_2 flakes at room temperature. Appl. Phys. Lett. **111**, 093102 (2017). https://doi.org/10.1063/1.5000825
190. F.K. Perkins, A.L. Friedman, E. Cobas, P.M. Campbell, G.G. Jernigan et al., Chemical vapor sensing with monolayer MoS_2. Nano Lett. **13**, 668–673 (2013). https://doi.org/10.1021/nl3043079
191. H. Li, Z. Yin, Q. He, H. Li, X. Huang et al., Fabrication of single- and multilayer MoS_2 film-based field-effect transistors for sensing NO at room temperature. Small **8**, 63–67 (2012). https://doi.org/10.1002/smll.201101016
192. M. Donarelli, S. Prezioso, F. Perrozzi, F. Bisti, M. Nardone et al., Response to NO_2 and other gases of resistive chemically exfoliated MoS_2-based gas sensors. Sens. Actuat. B Chem. **207**, 602–613 (2015). https://doi.org/10.1016/j.snb.2014.10.099
193. B. Cho, A.R. Kim, Y. Park, J. Yoon, Y.J. Lee et al., Bifunctional sensing characteristics of chemical vapor deposition synthesized atomic-layered MoS_2. ACS Appl. Mater. Interf. **7**, 2952–2959 (2015). https://doi.org/10.1021/am508535x
194. B. Liu, L. Chen, G. Liu, A.N. Abbas, M. Fathi et al., High-performance chemical sensing using Schottky-contacted chemical vapor deposition grown monolayer MoS_2 transistors. ACS Nano **8**, 5304–5314 (2014). https://doi.org/10.1021/nn5015215
195. H. Long, L. Chan, A. Harley-Trochimczyk, L.E. Luna, Z. Tang et al., 3D MoS_2 aerogel for ultrasensitive NO_2 detection and its tunable sensing behavior. Adv. Mater. Interf. **4**, 2–9 (2017). https://doi.org/10.1002/admi.201700217
196. S. Fathipour, M. Remskar, A. Varlec, A. Ajoy, R. Yan et al., Synthesized multiwall MoS_2 nanotube and nanoribbon field-effect transistors. Appl. Phys. Lett. **106**, 022114 (2015). https://doi.org/10.1063/1.4906066
197. K. Qi, S. Yu, Q. Wang, W. Zhang, J. Fan et al., Decoration of the inert basal plane of defect-rich MoS_2 with Pd atoms for achieving Pt-similar HER activity. J. Mater. Chem. A **4**, 4025–4031 (2016). https://doi.org/10.1039/c5ta10337a
198. L. Dong, S. Guo, Y. Wang, Q. Zhang, L. Gu et al., Activating MoS_2 basal planes for hydrogen evolution through direct CVD morphology control. J. Mater. Chem. A **7**, 27603–27611 (2019). https://doi.org/10.1039/c9ta08738a
199. Y. Ouyang, C. Ling, Q. Chen, Z. Wang, L. Shi et al., Activating inert basal planes of MoS_2 for hydrogen evolution reaction through the formation of different intrinsic defects. Chem. Mater. **28**, 4390–4396 (2016). https://doi.org/10.1021/acs.chemmater.6b01395
200. Q. Tang, D.E. Jiang, Stabilization and band-gap tuning of the 1T-MoS_2 monolayer by covalent functionalization. Chem. Mater. **27**, 3743–3748 (2015). https://doi.org/10.1021/acs.chemmater.5b00986
201. S. Wang, D. Zhang, B. Li, C. Zhang, Z. Du et al., Ultrastable in-plane 1T–2H MoS_2 heterostructures for enhanced hydrogen evolution reaction. Adv. Energy Mater. **8**, 1801345 (2018). https://doi.org/10.1002/aenm.201801345
202. C. Guo, J. Pan, H. Li, T. Lin, P. Liu et al., Observation of superconductivity in 1T′-MoS_2 nanosheets. J. Mater. Chem. C **5**, 10855–10860 (2017). https://doi.org/10.1039/c7tc03749j
203. D. Wang, X. Zhang, S. Bao, Z. Zhang, H. Fei et al., Phase engineering of a multiphasic 1T/2H MoS_2 catalyst for highly efficient hydrogen evolution. J. Mater. Chem. A **5**, 2681–2688 (2017). https://doi.org/10.1039/c6ta09409k
204. Y. Zhang, Y. Kuwahara, K. Mori, C. Louis, H. Yamashita, Hybrid phase 1T/2H-MoS_2 with controllable 1T concentration and its promoted hydrogen evolution reaction. Nanoscale **12**, 11908–11915 (2020). https://doi.org/10.1039/d0nr02525a
205. H. Cao, Z. Bai, Y. Li, Z. Xiao, X. Zhang et al., Solvothermal synthesis of defect-rich mixed 1T–2H MoS_2 nanoflowers for enhanced hydrodesulfurization. ACS Sustain. Chem. Eng. **8**, 7343–7352 (2020). https://doi.org/10.1021/acssuschemeng.0c00736
206. K. Yang, X. Wang, H. Li, B. Chen, X. Zhang et al., Composition- and phase-controlled synthesis and applications of alloyed phase heterostructures of transition metal disulphides. Nanoscale **9**, 5102–5109 (2017). https://doi.org/10.1039/c7nr01015j
207. B. Zong, Q. Li, X. Chen, C. Liu, L. Li et al., Highly enhanced gas sensing performance using a 1T/2H Heterophase MoS_2 field-effect transistor at room temperature. ACS Appl. Mater. Interf. **12**, 50610–50618 (2020). https://doi.org/10.1021/acsami.0c15162
208. Z. Chen, H. Xu, C. Liu, D. Cao, Q. Ye et al., Good triethylamine sensing properties of Au@MoS_2 nanostructures directly grown on ceramic tubes. Mater. Chem. Phys. **245**, 122683 (2020). https://doi.org/10.1016/j.matchemphys.2020.122683
209. H. Yan, P. Song, S. Zhang, J. Zhang, Z. Yang et al., A low temperature gas sensor based on Au-loaded MoS_2 hierarchical nanostructures for detecting ammonia. Ceram. Int. **42**, 9327–9331 (2016). https://doi.org/10.1016/j.ceramint.2016.02.160
210. D.H. Baek, J. Kim, MoS_2 gas sensor functionalized by Pd for the detection of hydrogen. Sens. Actuat. B Chem. **250**, 686–691 (2017). https://doi.org/10.1016/j.snb.2017.05.028
211. C. Kuru, C. Choi, A. Kargar, D. Choi, Y.J. Kim et al., MoS_2 nanosheet-Pd nanoparticle composite for highly sensitive room temperature detection of hydrogen. Adv. Sci. **2**, 1500004 (2015). https://doi.org/10.1002/advs.201500004
212. J. Jaiswal, P. Tiwari, P. Singh, R. Chandra, Fabrication of highly responsive room temperature H_2 sensor based on vertically aligned edge-oriented MoS_2 nanostructured thin film functionalized by Pd nanoparticles. Sens. Actuat. B Chem. **325**, 128800 (2020). https://doi.org/10.1016/j.snb.2020.128800
213. J. Park, J. Mun, J.-S. Shin, S.-W. Kang, Highly sensitive two-dimensional MoS_2 gas sensor decorated with Pt nanoparticles. R. Soc. Open Sci. **5**, 181462 (2018). https://doi.org/10.1098/rsos.181462
214. S.R. Gottam, C.T. Tsai, L.W. Wang, C.T. Wang, C.C. Lin et al., Highly sensitive hydrogen gas sensor based on a

 https://doi.org/10.1007/s40820-021-00724-1

MoS_2-Pt nanoparticle composite. Appl. Surf. Sci. **506**, 144981 (2020). https://doi.org/10.1016/j.apsusc.2019.144981

215. L. Chacko, E. Massera, P.M. Aneesh, Enhancement in the selectivity and sensitivity of Ni and Pd functionalized MoS_2 toxic gas sensors. J. Electrochem. Soc. **167**, 106506 (2020). https://doi.org/10.1149/1945-7111/ab992c
216. P. Halvaee, S. Dehghani, M. Mohammadzadeh, Room temperature methanol sensors based on rod-shaped nanostructures of MoS_2 functionalized with Ag nanoparticles. IEEE Sens. J. **21**, 4233–4240 (2021). https://doi.org/10.1109/JSEN.2020.3035753
217. Z. Hu, Z. Wu, C. Han, J. He, Z. Ni et al., Two-dimensional transition metal dichalcogenides: Interface and defect engineering. Chem. Soc. Rev. **47**, 3100–3128 (2018). https://doi.org/10.1039/c8cs00024g
218. J. Suh, T.E. Park, D.Y. Lin, D. Fu, J. Park et al., Doping against the native propensity of MoS_2: degenerate hole doping by cation substitution. Nano Lett. **14**, 6976–6982 (2014). https://doi.org/10.1021/nl503251h
219. A. Nipane, D. Karmakar, N. Kaushik, S. Karande, S. Lodha, Few-layer MoS_2 p-type devices enabled by selective doping using low energy phosphorus implantation. ACS Nano **10**, 2128–2137 (2016). https://doi.org/10.1021/acsnano.5b06529
220. M. Li, J. Yao, X. Wu, S. Zhang, B. Xing et al., P-type doping in large-area monolayer MoS_2 by chemical vapor deposition. ACS Appl. Mater. Interf. **12**, 6276–6282 (2020). https://doi.org/10.1021/acsami.9b19864
221. L. Shao, Z. Wu, H. Duan, T. Shaymurat, Discriminative and rapid detection of ozone realized by sensor array of Zn^{2+} doping tailored MoS2 ultrathin nanosheets. Sens. Actuat. B Chem. **258**, 937–946 (2018). https://doi.org/10.1016/j.snb.2017.11.166
222. A. Taufik, Y. Asakura, T. Hasegawa, H. Kato, M. Kakihana et al., Surface engineering of 1T/2H-MoS_2 nanoparticles by O_2 plasma irradiation as a potential humidity sensor for breathing and skin monitoring applications. ACS Appl. Nano Mater. **3**, 7835–7846 (2020). https://doi.org/10.1021/acsanm.0c01352
223. Y. Chen, F. Su, H. Xie, R. Wang, C. Ding et al., One-step construction of S-scheme heterojunctions of N-doped MoS_2 and S-doped g-C_3N_4 for enhanced photocatalytic hydrogen evolution. Chem. Eng. J. **404**, 126498 (2021). https://doi.org/10.1016/j.cej.2020.126498
224. D.N. Sangeetha, M.S. Santosh, M. Selvakumar, Flower-like carbon doped MoS_2/Activated carbon composite electrode for superior performance of supercapacitors and hydrogen evolution reactions. J. Alloys Compd. **831**, 154745 (2020). https://doi.org/10.1016/j.jallcom.2020.154745
225. R. Li, L. Yang, T. Xiong, Y. Wu, L. Cao et al., Nitrogen doped MoS_2 nanosheets synthesized via a low-temperature process as electrocatalysts with enhanced activity for hydrogen evolution reaction. J. Power Sour. **356**, 133–139 (2017). https://doi.org/10.1016/j.jpowsour.2017.04.060
226. P. Liu, Y. Liu, W. Ye, J. Ma, D. Gao, Flower-like N-doped MoS_2 for photocatalytic degradation of RhB by visible light irradiation. Nanotechnology **27**, 225403 (2016). https://doi.org/10.1088/0957-4484/27/22/225403
227. J. Guo, C. Liu, Y. Sun, J. Sun, W. Zhang et al., N-doped MoS_2 nanosheets with exposed edges realizing robust electrochemical hydrogen evolution. J. Solid State Chem. **263**, 84–87 (2018). https://doi.org/10.1016/j.jssc.2018.04.023
228. A. Taufik, Y. Asakura, T. Hasegawa, S. Yin, MoS_{2-x} Se_x nanoparticles for NO detection at room temperature. ACS Appl. Nano Mater. **4**, 6861–6871 (2021). https://doi.org/10.1021/acsanm.1c00926
229. C. Jin, X. Tang, X. Tan, S.C. Smith, Y. Dai et al., A Janus MoSSe monolayer: a superior and strain-sensitive gas sensing material. J. Mater. Chem. A **7**, 1099–1106 (2019). https://doi.org/10.1039/c8ta08407f
230. J. Zhu, H. Zhang, Y. Tong, L. Zhao, Y. Zhang et al., First-principles investigations of metal (V, Nb, Ta)-doped monolayer MoS2: Structural stability, electronic properties and adsorption of gas molecules. Appl. Surf. Sci. **419**, 522–530 (2017). https://doi.org/10.1016/j.apsusc.2017.04.157
231. D. Zhang, J. Wu, P. Li, Y. Cao, Room-temperature SO_2 gas-sensing properties based on a metal-doped MoS_2 nanoflower: an experimental and density functional theory investigation. J. Mater. Chem. A **5**, 20666–20677 (2017). https://doi.org/10.1039/c7ta07001b
232. S. Singh, S. Sharma, R.C. Singh, S. Sharma, Hydrothermally synthesized MoS_2-multi-walled carbon nanotube composite as a novel room-temperature ammonia sensing platform. Appl. Surf. Sci. **532**, 147373 (2020). https://doi.org/10.1016/j.apsusc.2020.147373
233. S.Y. Park, Y.H. Kim, S.Y. Lee, W. Sohn, J.E. Lee et al., Highly selective and sensitive chemoresistive humidity sensors based on rGO/MoS_2 van der Waals composites. J. Mater. Chem. A **6**, 5016–5024 (2018). https://doi.org/10.1039/c7ta11375g
234. G. He, D. Huang, Z. Yang, Y. Han, J. Hu et al., Linear humidity response of carbon dot-modified molybdenum disulfide. Phys. Chem. Chem. Phys. **20**, 4083–4091 (2018). https://doi.org/10.1039/C7CP07125F
235. N. Yue, J. Weicheng, W. Rongguo, D. Guomin, H. Yifan, Hybrid nanostructures combining graphene-MoS_2 quantum dots for gas sensing. J. Mater. Chem. A **4**, 8198–8203 (2016). https://doi.org/10.1039/c6ta03267b
236. L. Liu, M. Ikram, L. Ma, X. Zhang, H. Lv et al., Edge-exposed MoS2 nanospheres assembled with SnS_2 nanosheet to boost NO_2 gas sensing at room temperature. J. Hazard. Mater. **393**, 122325 (2020). https://doi.org/10.1016/j.jhazmat.2020.122325
237. M. Ikram, L. Liu, Y. Liu, L. Ma, H. Lv et al., Fabrication and characterization of a high-surface area MoS_2@WS_2 heterojunction for the ultra-sensitive NO_2 detection at room temperature. J. Mater. Chem. A **7**, 14602–14612 (2019). https://doi.org/10.1039/c9ta03452h
238. Y. Han, D. Huang, Y. Ma, G. He, J. Hu et al., Design of hetero-nanostructures on MoS_2 nanosheets to boost NO_2 room-temperature sensing. ACS Appl. Mater. Interf. **10**,

22640–22649 (2018). https://doi.org/10.1021/acsami.8b05811

239. W. Wang, Y. Zhen, J. Zhang, Y. Li, H. Zhong et al., SnO_2 nanoparticles-modified 3D-multilayer MoS_2 nanosheets for ammonia gas sensing at room temperature. Sens. Actuat. B Chem. **321**, 128471 (2020). https://doi.org/10.1016/j.snb.2020.128471
240. T. Pham, G. Li, E. Bekyarova, M.E. Itkis, A. Mulchandani, MoS_2 -based optoelectronic gas sensor with sub-parts-per-billion limit of NO_2 gas detection. ACS Nano **13**, 3196–3205 (2019). https://doi.org/10.1021/acsnano.8b08778
241. R. Kumar, N. Goel, M. Kumar, UV-activated MoS_2 based fast and reversible NO_2 sensor at room temperature. ACS Sens. **2**, 1744–1752 (2017). https://doi.org/10.1021/acssensors.7b00731
242. A. Ali, O. Koybasi, W. Xing, D.N. Wright, D. Varandani et al., Single digit parts-per-billion NO_x detection using MoS_2/hBN transistors. Sens. Actuat. A Phys. **315**, 112247 (2020). https://doi.org/10.1016/j.sna.2020.112247
243. Y. Kim, S.K. Kang, N.C. Oh, H.D. Lee, S.M. Lee et al., Improved sensitivity in Schottky contacted two-dimensional MoS_2 gas sensor. ACS Appl. Mater. Interf. **11**, 38902–38909 (2019). https://doi.org/10.1021/acsami.9b10861
244. M. Barzegar, A. Iraji zad, A. Tiwari, On the performance of vertical MoS_2 nanoflakes as a gas sensor. Vacuum **167**, 90–97 (2019). https://doi.org/10.1016/j.vacuum.2019.05.033
245. Y. Han, Y. Ma, Y. Liu, S. Xu, X. Chen et al., Construction of MoS_2/SnO_2 heterostructures for sensitive NO_2 detection at room temperature. Appl. Surf. Sci. **493**, 613–619 (2019). https://doi.org/10.1016/j.apsusc.2019.07.052
246. K.D. Bronsema, J.L. De Boer, F. Jellinek, On the structure of molybdenum diselenide and disulfide. ZAAC - J. Inorg. Gen. Chem. **540**, 15–17 (1986). https://doi.org/10.1002/zaac.19865400904
247. A. Eftekhari, Molybdenum diselenide ($MoSe_2$) for energy storage, catalysis, and optoelectronics. Appl. Mater. Today **8**, 1–17 (2017). https://doi.org/10.1016/j.apmt.2017.01.006
248. F. Jiang, W.-S. Zhao, J. Zhang, Mini-review: Recent progress in the development of $MoSe_2$ based chemical sensors and biosensors. Microelectron. Eng. **225**, 111279 (2020). https://doi.org/10.1016/j.mee.2020.111279
249. D.J. Late, T. Doneux, M. Bougouma, Single-layer $MoSe_2$ based NH_3 gas sensor. Appl. Phys. Lett. **105**, 3–7 (2014). https://doi.org/10.1063/1.4903358
250. S. Guo, D. Yang, S. Zhang, Q. Dong, B. Li et al., Development of a cloud-based epidermal $MoSe_2$ device for hazardous gas sensing. Adv. Funct. Mater. **29**, 1–10 (2019). https://doi.org/10.1002/adfm.201900138
251. Z. Yang, D. Zhang, D. Wang, Carbon monoxide gas sensing properties of metal-organic frameworks-derived tin dioxide nanoparticles/molybdenum diselenide nanoflowers. Sens. Actuat. B Chem. **304**, 127369 (2020). https://doi.org/10.1016/j.snb.2019.127369
252. R.K. Jha, J.V. D'Costa, N. Sakhuja, N. Bhat, $MoSe_2$ nanoflakes based chemiresistive sensors for ppb-level hydrogen sulfide gas detection. Sens. Actuat. B Chem. **297**, 126687 (2019). https://doi.org/10.1016/j.snb.2019.126687
253. X. Chen, X. Chen, Y. Han, C. Su, M. Zeng et al., Two-dimensional $MoSe_2$ nanosheets via liquid-phase exfoliation for high-performance room temperature NO_2 gas sensors. Nanotechnology (2019). https://doi.org/10.1088/1361-6528/ab35ec
254. D. Zhang, Q. Li, P. Li, M. Pang, Y. Luo, Fabrication of Pd-decorated $MoSe_2$ nanoflowers and density functional theory simulation toward ammonia sensing. IEEE Electron Device Lett. **40**, 616–619 (2019). https://doi.org/10.1109/LED.2019.2901296
255. D. Zhang, Z. Yang, P. Li, M. Pang, Q. Xue, Flexible self-powered high-performance ammonia sensor based on Au-decorated $MoSe_2$ nanoflowers driven by single layer MoS_2-flake piezoelectric nanogenerator. Nano Energy **65**, 103974 (2019). https://doi.org/10.1016/j.nanoen.2019.103974
256. Y.F. Lin, Y. Xu, C.Y. Lin, Y.W. Suen, M. Yamamoto et al., Origin of noise in layered $MoTe_2$ transistors and its possible use for environmental sensors. Adv. Mater. **27**, 6612–6619 (2015). https://doi.org/10.1002/adma.201502677
257. Z. Feng, Y. Xie, E. Wu, Y. Yu, S. Zheng et al., Enhanced sensitivity of $MoTe_2$ chemical sensor through light illumination. Micromachines **8**, 155 (2017). https://doi.org/10.3390/mi8050155
258. E. Wu, Y. Xie, B. Yuan, H. Zhang, X. Hu et al., Ultrasensitive and fully reversible NO_2 gas sensing based on p-type $MoTe_2$ under ultraviolet illumination. ACS Sens. **3**, 1719–1726 (2018). https://doi.org/10.1021/acssensors.8b00461
259. E. Wu, Y. Xie, B. Yuan, D. Hao, C. An et al., Specific and highly sensitive detection of ketone compounds based on p-type $MoTe_2$ under ultraviolet illumination. ACS Appl. Mater. Interf. **10**, 35664–35669 (2018). https://doi.org/10.1021/acsami.8b14142
260. S.Y. Cho, J.Y. Kim, O. Kwon, J. Kim, H.T. Jung, Molybdenum carbide chemical sensors with ultrahigh signal-to-noise ratios and ambient stability. J. Mater. Chem. A **6**, 23408–23416 (2018). https://doi.org/10.1039/C8TA07168C
261. F. Rasch, V. Postica, F. Schütt, Y.K. Mishra, A.S. Nia et al., Highly selective and ultra-low power consumption metal oxide based hydrogen gas sensor employing graphene oxide as molecular sieve. Sens. Actuat. B Chem. **320**, 128363 (2020). https://doi.org/10.1016/j.snb.2020.128363

 https://doi.org/10.1007/s40820-021-00724-1